

Non-contrast Estimation of Respiration and Heartbeat Rate using Ultra-Wideband Signals

Chang Li

Thesis submitted to the Faculty of the
Virginia Polytechnic Institute and State University
in partial fulfillment of the requirements for the degree of

Master of Science
in
Electrical Engineering

Dr. R. M. Buehrer, co-chair
Dr. C. R. C. M. da Silva, co-chair
Dr. J. H. Reed

August 29, 2008
Blacksburg, Virginia

Keywords: Wireless, Ultra-wideband, vital-signs estimation, continuous wavelet transform, elliptical fitting, Welch periodogram, MUSIC, array processing

Non-contrast Estimation of Respiration and Heartbeat Rate using Ultra-Wideband Signals

Chang Li

ABSTRACT

The use of ultra-wideband (UWB) signals holds great promise for remote monitoring of vital-signs which has applications in the medical, for first responder and in security. Previous research has shown the feasibility of a UWB-based radar system for respiratory and heartbeat rate estimation. Some simulation and real experimental results are presented to demonstrate the capability of the respiration rate detection. However, past analysis are mostly based upon the assumption of an ideal experiment environment. The accuracy of the estimation and interference factors of this technology has not been investigated.

This thesis establishes an analytical framework for the FFT-based signal processing algorithms to detect periodic bio-signals from a single target. Based on both simulation and experimental data, three basic challenges are identified: (1) Small body movement during the measurement interval results in slow variations in the consecutive received waveforms which mask the signals of interest. (2) The relatively strong respiratory signal with its harmonics greatly impact the detection of heartbeat rate. (3) The non-stationary nature of bio-signals creates challenges for spectral analysis. Having identified these problems, adaptive signal processing techniques have been developed which effectively mitigate these problems. Specifically, an ellipse-fitting algorithm is adopted to track and compensate the aperiodic large-scale body motion, and a wavelet-based filter is applied for attenuating the interference caused by respiratory harmonics to accurately estimate the heartbeat frequency. Additionally, the spectrum estimation of non-stationary signals is examined using a different transform method. Results from simulation and experiments show that substantial improvement is obtained by the use of these techniques.

Further, this thesis examines the possibility of multi-target detection based on the same measurement setup. Array processing techniques with subspace-based algorithms are applied to estimate multiple respiration rates from different targets. The combination of array processing and single-target detection techniques are developed to extract the heartbeat rates. The performance is examined via simulation and experimental results and the limitation of the current measurement setup is discussed.

This work received support from the Wireless@Virginia Tech.

Acknowledgments

I owe much, in particular to the development and completion of this work, to my advisor, Dr. R. Michael Buehrer. I have learned a tremendous amount from him not only in the academic area but also the great attitude towards work and life, and I believe his guidance has well prepared me for the future. I would also like to thank Dr. Claudio da Silva for advising me and Dr. Jeffrey Reed for serving on my committee and reviewing my work. Many thanks go to everyone at MPRG, especially Haris Volos, Jeong-heon Lee, Xuetao Chen, An He and Chris Anderson for their help to conducting measurements. Thanks to all the staff for always keeping everything running smoothly and for willingly helping me whenever I needed it. Many thanks also go to the faculty and students of the Virginia Tech Antenna Group (VTAG) for providing the measurement equipment that much of this work is built upon.

I would also like to thank my family, and Lijing Zhang for their constant love and support.

Thanks also to other students. I appreciate having had the chance to get to know many of them and learn more about the world and other cultures from them. I would further like to thank my friends Yue Hou, Ying Wang, Yun Wang, Xiang Cai, Yisi sun, and Tina Wang for their support and helping me keep perspective and optimistic during the occasionally stressful times.

I would finally like to thank all of the people whose endless support made this work possible!

List of Abbreviations

CTFT	Continuous Time Fourier Transform
CWT	Continuous Wavelet Transform
DFT	Discrete Fourier Transform
FFT	Fast Fourier Transform
ICWT	Inverse Continuous Wavelet Transform
MTI	Moving-Target Indication
MUSIC	Multiple Signal Classification
SNR	Signal to noise ratio
UWB	Ultra-Wideband

Contents

1	Introduction	1
1.1	Motivation	1
1.2	System Concept	3
1.3	Previous Work	5
1.4	Ultra-Wideband Technology	6
1.5	Thesis Organization	12
2	FFT-based Signal Processing Techniques for Vital-signs Estimation	14
2.1	Introduction	14
2.2	Measurement Setup	16
2.3	Mathematical Formulation	17
2.3.1	Continuous-Time Signal Processing	24
2.3.2	Finite Record Length	27
2.3.3	Effect of Fast-time Index, Modulation Index and Pulse Width	28
2.4	Simulation Results	29
2.5	Experimental Results	36
2.6	Conclusions	39
3	Improved Single-Target Respiration Rate Estimation	40
3.1	Introduction	40
3.2	Mean Position Tracking Algorithms	42
3.2.1	Moving Average Filter	42

3.2.2	Ellipse Fitting Algorithm	45
3.3	Experimental Results	55
3.4	Conclusions	57
4	Improved Single-Target Heartbeat Rate Estimation	58
4.1	Introduction	58
4.2	Respiratory Interference Cancellation	59
4.2.1	Wavelet Transform	59
4.2.2	Shape Factor β for Morlet Wavelet	65
4.2.3	Wavelet-based Filter	67
4.3	Simulation Results	73
4.4	Frequency Estimation for Non stationary Signals	76
4.5	Experimental Results	81
4.6	Conclusions	81
5	Multi-Target Vital-Signs Estimation	85
5.1	Introduction	85
5.2	Multi-Target Respiration Rate Estimation	86
5.2.1	Array processing for respiration estimation	86
5.2.2	Simulation Results	91
5.2.3	Experimental Results	93
5.3	Multi-target Heartbeat Rate Estimation	95
5.3.1	Combination of single-target and multi-target techniques	95
5.3.2	Simulation Results	96
5.3.3	Limitations of the measurement setup	97
5.4	Conclusions	98
6	Concluding Remarks	104
	Bibliography	106

List of Figures

1.1	UWB emission limits for indoor communication devices	8
1.2	UWB emission limits for outdoor hand-held communication devices	9
1.3	UWB emission limits for imaging systems	9
1.4	Second derivative Gaussian (a) Time domain and (b) Frequency domain . . .	10
1.5	Ultra-wideband versus Narrowband signals	11
2.1	Basic Pulse Radar System	15
2.2	Measurement Setup	17
2.3	A sample received signal waveform in fast-time	20
2.4	Computation of Background Clutter by averaging (From [1])	21
2.5	Output after Motion-Filter processing (From [1])	22
2.6	Large modulation index results in several peaks at the harmonics of f_b (From [1])	30
2.7	Small modulation index results in a single strong peak at f_b (From [1]) . . .	31
2.8	Flow chart of FFT-based algorithm	33
2.9	Slow-time range bin which contains the maximum energy, assuming the breathing rate is 0.2Hz and Heartbeat rate is 1.5Hz	33
2.10	Frequency content of the slow-time range bin which contains the maximum energy, assuming the breathing rate is 0.2Hz and Heartbeat rate is 1.5Hz . .	34
2.11	Frequency content of the slow-time range bin which contains the maximum energy, assuming the breathing rate is 0.4Hz and Heartbeat rate is 1.5Hz . .	34
2.12	Average error of FFT-based breathing and heartbeat rate estimation from simulation	36
2.13	Distribution of estimation error of the heartbeat rate at SNR=20dB	37

3.1	Slow-time variation along the range bin containing the maximum energy from experiment data	41
3.2	FFT of the Slow-time variation along the the range bin containing the maximum energy from experiment data	42
3.3	Moving average filter performance on the observed trajectory from real experiments (target's breathing period is 5.45seconds, L = 5seconds)	44
3.4	Moving average filter performance on the observed trajectory from real experiments (target's breathing period is 5.45second, L = 3seconds)	44
3.5	Simulation results for the moving average filter for mean position tracking	46
3.6	Performance of mean position estimation by ellipse fitting algorithm with different window sizes on the simulated sinusoidal trajectory	52
3.7	Comparison of simulation result of the moving average filter and ellipse fitting algorithm for mean position tracking	53
3.8	Comparison of moving average and ellipse fitting estimator for mean position tracking: window length equals to 15 breaths/min, target respiration rate is 16 breaths/min	54
3.9	Comparison of moving average and ellipse fitting estimator for mean position tracking: window length equals to 15 breaths/min, target respiration rate is 21 breaths/min	54
3.10	Slow-time variation along the range bin containing maximum energy from experiment data with estimated drifting mean value	55
3.11	FFT of the Slow-time variation along the range bin containing maximum energy from experiment data after compensating drifting mean value	57
4.1	Four different wavelet bases (a)Morlet (b) Paul(m=4) (c)Mexican hat(DOG m=2), and (d) DOG (m=6), based on [2]	64
4.2	Shape of standard Morlet wavelet function in frequency at scale s corresponding to the fundamental respiration frequency, $\beta = 1$	67
4.3	Shape of standard Morlet wavelet function in frequency at scale s corresponding to the 2nd harmonic of respiration frequency, $\beta = 1$	68
4.4	Shape of standard Morlet wavelet function in frequency at scale s corresponding to the 3rd harmonic of respiration frequency, $\beta = 1$	68
4.5	Shape of modified Morlet wavelet function in frequency at scale s corresponding to the fundamental respiration frequency, $\beta = 5$	69

4.6	Shape of modified Morlet wavelet function in frequency at scale s corresponding to the 2nd harmonic of respiration frequency, $\beta = 5$	69
4.7	Shape of modified Morlet wavelet function in frequency at scale s corresponding to the 3rd harmonic of respiration frequency, $\beta = 5$	70
4.8	Comparison of magnitude of $\Psi(s\omega_0)$ along scale-axis s at the frequency ω_0 corresponding to fundamental respiration rate	70
4.9	Comparison of magnitude of $\Psi(s\omega_0)$ along scale-axis s at the frequency ω_0 corresponding to 2nd harmonic respiration rate	71
4.10	Comparison of magnitude of $\Psi(s\omega_0)$ along scale-axis s at the frequency ω_0 corresponding to 3rd harmonic respiration rate	71
4.11	Original spectrum of the observed trajectory at $f_r = 0.33Hz$ and $f_h = 1.16Hz$	74
4.12	Spectrum of the observed trajectory after apply a bandpass filter with pass-band of $[0.7\ 4]Hz$ at $f_r = 0.33Hz$ and $f_h = 1.16Hz$	75
4.13	Spectrum of the observed trajectory after proposed filtering at $f_r = 0.33Hz$ and $f_h = 1.16Hz$	75
4.14	Average error of heartbeat rate estimation from simulation	76
4.15	Original spectrum of the observed trajectory at $f_r = 0.33Hz$ and $f_h = 1.08Hz$	77
4.16	Spectrum of the observed trajectory after proposed filtering at $f_r = 0.33Hz$ and $f_h = 1.08Hz$	77
4.17	Illustration of the data segments of input sequence	79
4.18	Performance of FFT spectrum and Welch periodogram of the observed trajectory	82
4.19	Spectrum of the observed trajectory for respiration rate detection	83
4.20	Spectrum of the observed trajectory for heartbeat rate detection	83
5.1	Scenario setup for two person monitoring	87
5.2	Spectrum of the array of the observed trajectory by using MUSIC algorithm, assuming Target1's respiration rate is 20 breaths/min (0.33Hz), Target2's respiration rate is 15 breaths/min (0.25Hz)	92
5.3	Spectrum of the array of the observed trajectory by using MUSIC algorithm, assuming Target1's respiration rate is 20 breaths/min (0.33Hz), Target2's respiration rate is 15 breaths/min (0.25Hz); Target1's receiving pulse amplitude is twice as the Target2's	92

5.4	Average error of two-target respiration rate estimation from simulation using MUSIC algorithm	94
5.5	Distribution of estimation error of the multi-target respiration rate at SNR=20dB	94
5.6	Scenario setup for multi-target monitoring	100
5.7	Respiration rate detection in three-target scenario	101
5.8	Performance of multiple targets heartbeat estimation with overlapped echo pulses	102
5.9	Performance of multiple targets heartbeat estimation with non-overlapped echo pulses	103

List of Tables

1.1	Previous research on the use of UWB radar system for vital-signs detection .	7
2.1	Performance of the FFT-based Respiration and Heart Rate Estimation Approach	38
3.1	Performance of the New Respiration Estimation Approach	56
4.1	Wavelet basis functions	63
4.2	Performance of the New Heartbeat Estimation Approach	84
5.1	Reference and Estimated Respiration Rate	95

Chapter 1

Introduction

1.1 Motivation

The motivation behind this thesis comes from the interest in using Ultra-wideband (UWB) technology to monitor cardiac and respiratory activities of human beings, without direct skin contact.

In the medical field, for many situations, it is essential that a subject's respiration and heart-beat be monitored. The primary tool used for monitoring heartbeat is the voltage-derived electrocardiogram (ECG). Electrical signals cause the heart muscle to contract. These signals pass through the body and can be measured by electrodes (electrical contacts) attached to the skin. Electrodes on different sides of the heart measure the activity of different parts of the heart muscle. An ECG displays the voltage between pairs of these electrodes, and the muscle activity that they represent, from different directions. This display indicates the overall rhythm of the heart. A measurement typically requires placement of twelve electrodes on the body. Another tool which is frequently used in hospital settings is the pulse oximeter.

As a patient's hemoglobin saturation drops, blood becomes bluer in color. A pulse oximeter measures the amount of oxygen in a patient's blood by observing light reflections. As blood vessels expand and contract with every heart beat, the pulse oximeter signal fluctuates. The pulse oximeter probe also requires direct contact with the finger or ear lobe. Additionally, the stethoscope is an acoustic tool that enables physicians to listen to heart sounds and breathing. In summary, all of these tools require a direct physical connection to the patient. UWB technology could provide a continuous, non-contact technique for cardiac and respiratory assessment that would be beneficial for minimizing patient disruption. The utilization of this technique can be applied to three application areas: health care, emergency rescue operations and security. As a non-contact wireless monitoring technique, it has the following advantages over traditional health care monitoring devices:

- Devices requiring physical contact are difficult to use on infants or burn patients who can not tolerate the touch of electrodes. However, wireless sensors reduce such complexity and the difficulty of acquiring vital signs when the patients's health condition is critical. This non-invasive technique may improve patient care without causing discomfort to patients.
- Contact-free sensors can be used for long-term monitoring of activities during daily living for the sake of disease prevention or early diagnosis. Other similar proposed applications include monitoring for sudden infant death syndrome (SIDS) and sleep apnea syndrome.
- When multiple patients are located within a few meters of each other, their vital signs can be monitored independently at the same time by a single device. This potentially reduces the cost of health care by reducing the number of medical devices being used per patient.

- Wireless systems may be useful to share the monitored data with other systems and/or central repositories.
- Finally, several networked sensors could be used together to increase the accuracy of a patients' measurement.

In addition to the potential use of UWB monitoring in health care, this technique can be applied to emergency rescue situations, particularly to the problem of triage when victims are trapped under debris. Existing methods for locating and rescuing human victims buried include the utilization of dogs, seismic or optical devices. These existing devices are not effective if the rubble or debris covering the human victims is thicker than a few feet, especially in the case when the victims are completely trapped or too weak to respond to the signals sent by the rescuers. Thus, a sensitive UWB life-detector that can penetrate common building materials to detect respiration and body movement, would be useful in search and rescue operations to identify live victims under collapsed structures [3].

For security applications, UWB monitoring can be applied to aid in the physiological detection of deception (PDD) [4]. Also, this can be applied in other applications such as airport security, customs/immigration, and military checkpoints.

1.2 System Concept

Cardiac and respiratory monitoring can be achieved through detecting the small body motion of the target produced by the related organs. The basic components of a UWB sensing system include a transmitter, a reflective target, a receiver, and a signal processor. The transmitter generates a series of short duration pulses. The shape of the the transmitted pulses is largely determined by the characteristics of the antenna. At dielectric interfaces of

the target, portions of the transmitted pulse are reflected back toward the antenna. When the target surface is moving, as does the surface of the chest in conjunction with respiratory and cardiac activities, the corresponding variation will be observed through the measured time-delays from the echo waveforms. Post signal processing algorithms can be used to target specific respiratory and cardiac frequencies.

Specifically, we define the model for the target properties and the expected target movement [5]. The human lung is located behind the chest and has a volume of about 4-6 liters. The tidal volume is normally between 500ml and 800ml. This breathing activity will cause a chest movement of about 10mm to 20mm. The radiated antenna of the UWB radar will be reflected partially at every dielectric boundary. The main reflection will occur at the air/chest interface. The propagation impedance in free space η_0 is defined as [5]

$$\begin{aligned}\eta_0 &= \sqrt{\frac{\mu_0}{\epsilon_0}} = 376.73\Omega & (1.1) \\ \mu_0 &= 4\pi \times 10^{-7} \frac{H}{m} \\ \epsilon_0 &\approx 8.8542 \times 10^{-12} \frac{F}{m}\end{aligned}$$

where μ_0 is the permeability of a vacuum and ϵ_0 is the permittivity of a vacuum. By taking the relative permittivity ϵ_r into account, the propagation impedance η of a material can be determined by

$$\eta = \sqrt{\frac{\mu_0}{\epsilon_0 \epsilon_r}} \quad (1.2)$$

For example, dry skin has as relative permittivity $\epsilon_r = 40$ at a frequency of $f = 1.4GHz$.

This yields a propagation impedance of

$$\eta_{skin} = \sqrt{\frac{\mu_0}{\epsilon_0 \epsilon_r}} \approx 59.57 \Omega \quad (1.3)$$

The reflection coefficient Γ is defined as

$$\Gamma = \frac{\eta_{skin} - \eta_0}{\eta_{skin} + \eta_0} \quad (1.4)$$

which results in a reflection coefficient of 72.7%, which means that about 72.7% of the energy of the electromagnetic waves at the air-dry-skin interface is reflected. Therefore, the expansion of the chest cavity creates an observable change in the multipath profile, which is exploited to determine the respiration rate.

1.3 Previous Work

Radar monitoring of human physiologic functions was considered as early as the 1970s [6]. Non-invasive sensing with microwave radars were first demonstrated by Lin in [7], [8], [9], where respiration [7], [8] and heartbeat [9] are measured separately, with a cessation in breathing required for the heart rate measurement. In [7], a non-anesthetized rabbit's respiration is measurement from 30cm. In [8], the same system was tested on a rabbit and two cats, all of which were anesthetized and intubated.

From the mid-1980's through late 1990's, microwave doppler radar transceivers were developed that incorporated analog and digital signal processing to separate the small heart signal from the much larger respiration signal, so that the subject did not need to hold his/her breath for the heart rate to be measured, and heart and respiration could be measured simultaneously [10], [11], [12], [13]. A Radar Vital Signs Monitor (RVSM) developed

by Greneker at [14] was used to detect the heart and respiration rate of athletes at the 1996 Olympics in Atlanta.

More recently, with the development of Ultra-wideband technology, UWB radar has been used for detecting of heartbeat and respiration rates. Previous research in this area is summarized in the Table 1.1. We can conclude that most of the published work focused on demonstrating the capability and feasibility of respiration and heartbeat rate estimation with the use of UWB radar system. Although a simple FFT-based signal processing framework was presented with simulation and experimental results, no detailed analysis on the performance of such techniques was investigated. The accuracy and reliability of these proposed approaches have not been seriously discussed, and we have no information on the interference analysis or the quality of the detection. So it is our goal to evaluate these techniques through a large number of experiments, and identify the major impediments for accurate estimation of respiration and heartbeat rate. Based on the analysis of the experimental results, we expect to develop more robust signal processing algorithms to improve the performance of UWB radar monitoring.

1.4 Ultra-Wideband Technology

The U.S. Federal Communications Commission (FCC) defined UWB signals as those which have a fractional bandwidth greater than 0.20 or a bandwidth greater than 500MHz measured at the -10dB points. Fractional bandwidth is defined as the ratio of the bandwidth occupied by the signal to the center frequency of the signal: $\frac{f_h - f_l}{f_c}$, where f_h and f_l are denoted as the upper and lower limits of the 10dB bandwidth of the signal respectively, and f_c is defined as

Table 1.1: Previous research on the use of UWB radar system for vital-signs detection

Year	Reference	Description and Results
2002	Staderini [6]	Suggestion of the use of UWB radars for non-invasive biomedical applications is described, including cardiac and respiratory monitoring. A physical model for pulse-echo behavior is found by the UWB pulse while traveling through the human thorax from the skin to the heart.
2004	Ossberger et al. [5]	Experimental results are shown on the use of UWB signals to detect the respiration rate of individuals with different distances and behind walls. No detailed analysis was presented regarding signal processing algorithms.
2005	Paksuniemi et al. [15]	Needs and demands concerning patient monitoring utilizing wireless technology, such as UWB radars, are investigated. The necessity and benefit for the UWB-based monitoring are discussed.
2005	Venkatesh et al. [16]	A FFT-based framework for signal processing algorithms to estimate respiration and heartbeat rate of single target using UWB radars is presented. Experimental results demonstrate the capability of the proposed approach for reliable respiration rate estimation. But heartbeat rate estimation shows much larger error compared with respiration rate estimation.
2006	Kang et al. [17]	A subspace-based algorithm for estimation of the time delay of a reflected signal from single target is presented. The simulations on UWB propagation through the tissue model demonstrate the capability of respiration rate detection.
2006	Rivera et al. [18]	The techniques of multi-target vital-signs estimation based on [16] are developed. Clustering and MUSIC algorithms are introduced to detect multiple respiration rates. Experimental examples of two and three targets scenario demonstrates the capability of multiple respiration and heartbeat rates estimation.
2007	Gezici et al. [19]	The analysis of theoretical limits for estimation of periodic movements in pulse-based UWB systems is given.
2007	Bilich et al. [20]	The feasibility of UWB heartbeat rate sensing under the FCC power restriction is investigated.

the center frequency. Therefore, the definition of a UWB signal can be expressed as:

$$\begin{aligned} (f_h - f_l) &\geq 500MHz \\ \frac{f_h - f_l}{f_c} &= 2\left(\frac{f_h - f_l}{f_h + f_l}\right) \geq 0.2 \end{aligned} \quad (1.5)$$

UWB signals have been used in the military for radar applications since the 70's. In February 2002, the FCC legalized the use of UWB by releasing a set of spectral "masks" [21], in the portion of the spectrum from several hundred MHz to approximately 10 GHz, which stipulated the emission level and frequency of operation for imaging, radar, and communication purposes. Figures 1.1-1.3 show the FCC spectral masks for UWB systems. A large bandwidth of 7.5GHz is available between 3.1GHz and 10.6GHz at a maximum power output of -41.3dBm/MHz . This sparked a huge amount of interest in UWB technology.

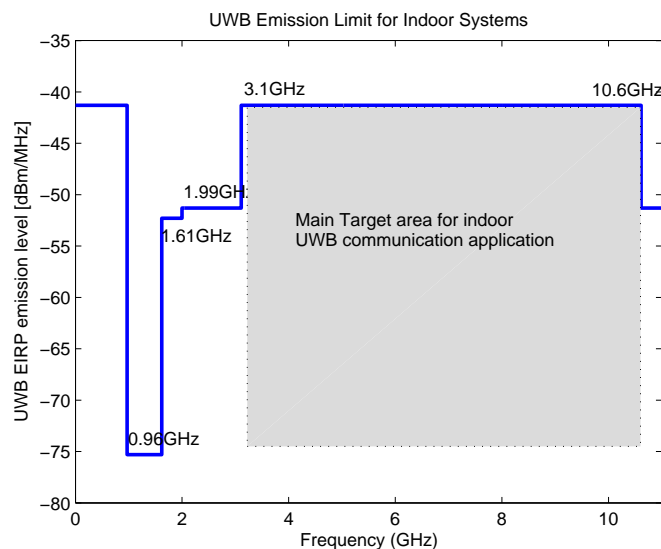


Figure 1.1: UWB emission limits for indoor communication devices

While different methods could be employed to achieve these large bandwidths, typically the term UWB refers to systems that use impulse radio. Impulse radio is a form of UWB signaling

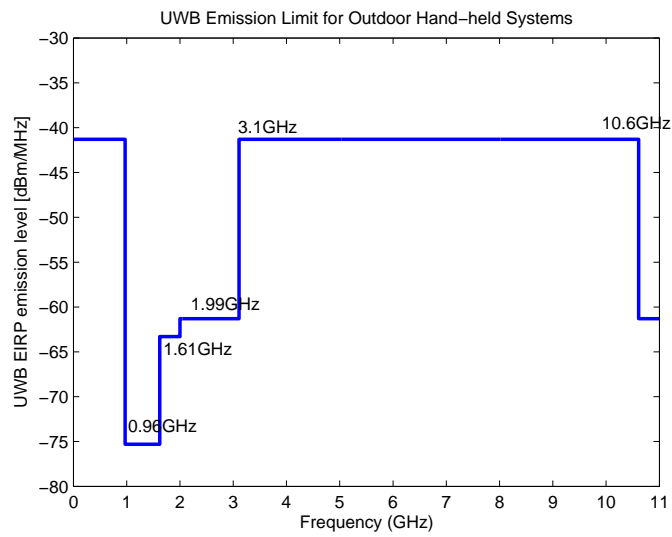


Figure 1.2: UWB emission limits for outdoor hand-held communication devices

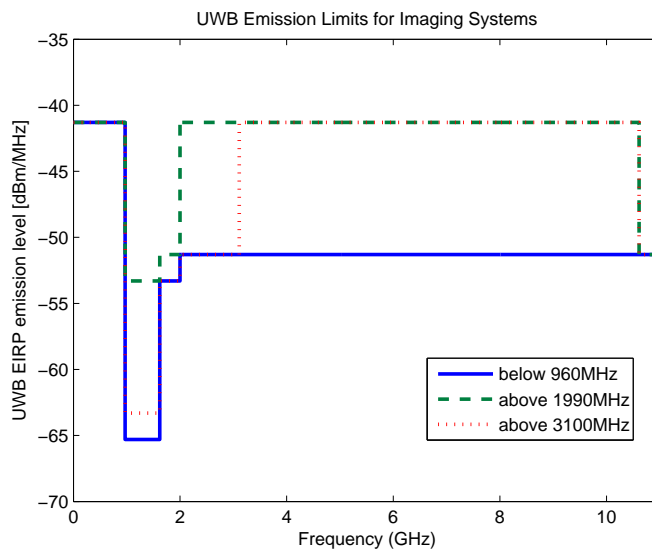


Figure 1.3: UWB emission limits for imaging systems

which uses streams of pulses of very short duration [22]. The pulse width of a UWB signal is usually on the order of nanoseconds, with rise times as fast as 50 picoseconds, corresponding to a frequency range that spans several gigahertz. Sample UWB signals in time and frequency domain are shown in Figure 1.4. Since the energy of the pulse is distributed across many frequencies, the power spectral density is much lower in magnitude than a narrowband system as illustrated in Figure 1.5. To a narrowband system, ultra-wideband signals appear below the noise floor, and are therefore very difficult to detect. UWB communication systems are useful for high data rate transmission in harsh propagation environment. However, widespread commercial use of UWB signals has been limited, largely as a result of FCC restrictions. Due to the concerns of interference with existing communication and navigation systems, the FCC limits the UWB frequency bands and output power. Particularly, medical applications are limited to the 3.1 to 10.6GHz range [21] as shown in Figure 1.1.

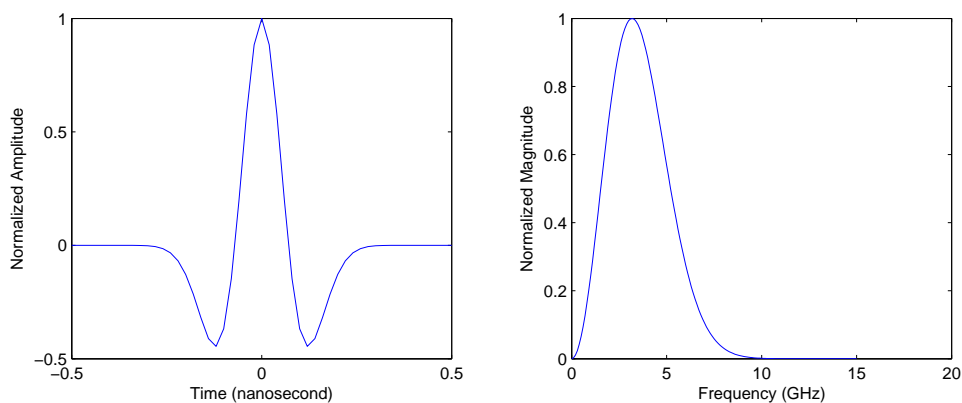


Figure 1.4: Second derivative Gaussian (a) Time domain and (b) Frequency domain

The key benefits of UWB signals versus traditional narrowband signals can be summarized as:

- High data rate: While current chipsets are continually being improved, most UWB communication applications are targeting the range of 100-500 Mbps, which is roughly

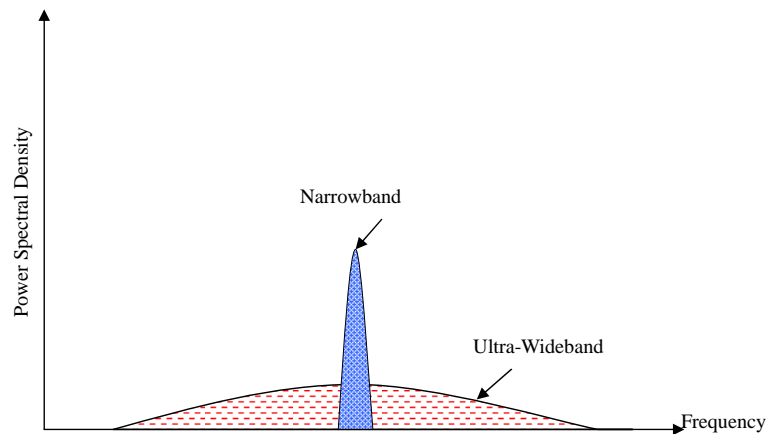


Figure 1.5: Ultra-wideband versus Narrowband signals

the equivalent of wired Ethernet to USB 2.0. It is significant that this data rate is 100-500 times the speed of Bluetooth, and around 50 times the speed of the 802.11b, or 10 times the 802.11a WLAN standards.

- Low system complexity and low cost: UWB systems can be made nearly “all-digital”, with minimal radiofrequency (RF) or microwave electronics. The low component count leads to reduced-cost systems.
- Multipath immunity: The received pulses are relatively immune to the multipath fading that affects narrowband signals. The robustness to multipath fading is due to the fine temporal resolution provided by UWB signals, which allows individual multipath components to be resolved.

Additionally, the impulse-based UWB has some unique advantages over other wireless radars applied in medicine-related fields [23], [24] that include:

- Compared to microwave Doppler radars, UWB signals are capable of penetrating a great variety of materials (esp. in the lower UWB band), including plastic, wood, rubber, sheetrock, dry soil, glass, and concrete [25], [26]. In general, systems with lower

center frequencies achieve better material penetration. Biological materials including skin, muscle, fat, and bone can also be penetrated, although not as easily as most low conductivity building materials. This good material penetration property can provide better coverage for indoor applications and the ability to perform through-wall measurement or monitoring.

- Since UWB signals are non-ionizing, they do not cause the adverse effects associated with X-ray systems such as CT scanners. UWB sensing systems may enable physicians to make a preliminary diagnosis without subjecting the patient to risk or discomfort. In addition, these sensors are well-suited for continuous patient monitoring to identify baseline changes.
- Impulse radio may potentially be manufactured inexpensively with small user terminals/antennas requiring low power. Unlike traditional ultrasound systems which require direct skin contact, UWB sensors can operate at a standoff distance. Due to both their portability and low cost, UWB sensors are ideal candidates for use in rural or remote settings and for in-field use by first responders.
- A UWB system has the potential to support high data rates while appearing noise-like to other RF technologies, and offers inherent data security due to covertness with applications in battlefield communications.

1.5 Thesis Organization

This thesis covers several topics related to non-contact monitoring of vital-signs using UWB radar systems. In this chapter, a background material concerning the benefits of a UWB-based wireless monitoring system are described. The basic UWB technology is also briefly

introduced. In Chapter 2, a measurement setup for respiration and heartbeat rate estimation is presented. A FFT-based signal processing algorithm based on this setup is presented along with simulation and experimental results. Chapter 3 identifies the major impediment to accurate respiration frequency estimation. This impediment is interference due to large-scale body motion. An improved algorithm is proposed to avoid false detection due to this interference. The simulation and experimental results demonstrate the robustness of the proposed method. In Chapter 4, challenges that impact heartbeat signal detection are identified and various techniques are developed to tackle these challenges. The efficacy of these approaches is verified by simulation and experimental results. In Chapter 5, a multi-target monitoring system is developed. Based on the single target detection framework, different algorithms for the estimation of multiple respiration and heartbeat rates estimation are investigated. Finally, Chapter 6 summarizes the contributions of this thesis.

Chapter 2

FFT-based Signal Processing

Techniques for Vital-signs Estimation

2.1 Introduction

UWB has been used in radar applications since the 1970s due to its fine time-resolution characteristics. Pulse-radar systems can provide accurate range estimates of targets. A basic pulse-radar system is shown in Figure 2.1. A transmitter transmits a series of pulses at a regular repetition rate. These pulses reflect off the target and are collected by the receiver. The distance between the transmitter and the target is d_T , and the distance between the receiver and the target is d_R . Assuming that the speed of propagation of electromagnetic waves in the environment is c , the total time taken for the pulse to reach the target from the transmitter is given by

$$\tau_T = \frac{d_T}{c} \tag{2.1}$$

and the time taken by pulse reflected from the target to reach the receiver is given by

$$\tau_R = \frac{d_R}{c} \quad (2.2)$$

Therefore, the pulse reaches the receiver at the time

$$\tau = \tau_0 + \tau_T + \tau_R \quad (2.3)$$

where τ_0 is the time instant the pulse is transmitted. By maintaining time synchronism between the transmitter and the receiver, the round-trip distance to the target $d = d_T + d_R$ can be estimated.

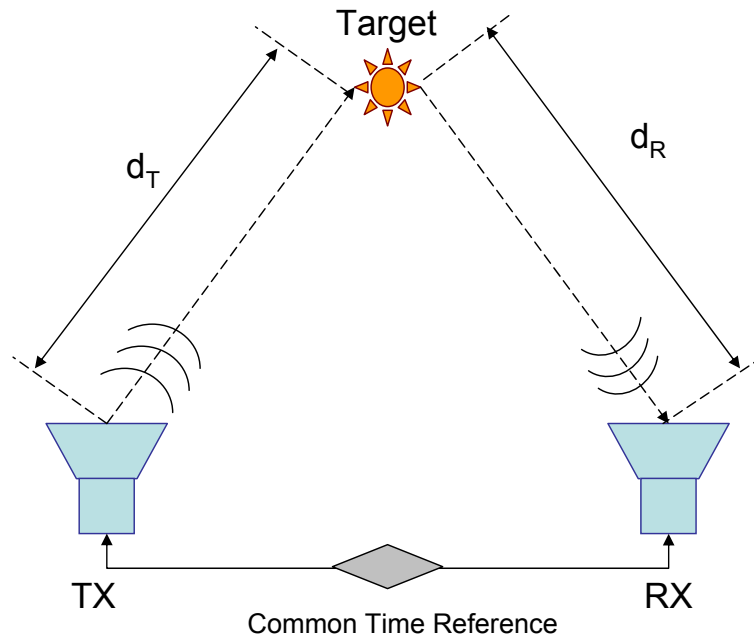


Figure 2.1: Basic Pulse Radar System

In principle, the range of any target can be estimated using the above radar operation. However, in practice, electromagnetic energy is reflected not only by the target, but by other scatters in the propagation environment, such as rocks, water, buildings and trees. Therefore,

at the receiver, the received signal is a superposition of the reflected pulses arriving via a large number of paths from scatterers in the environment. This constitutes multipath, and signal components which are not from the target of interest are termed “background clutter”. Often, we are interested only in detecting moving targets and determining their speed and other parameters in addition to their range. In such a case, signal processing techniques are used to eliminate stationary scatters and extract signal components pertaining to moving targets. Such radars are called Moving-Target Indication (MTI) radars. In the case of UWB radar applied to the medical, since the target of interest is the motion of the respiratory and cardiac organs, it can be regarded as a special kind of MTI radar.

This chapter introduces the measurement setup for the proposed monitoring system and demonstrates the mathematical formula for FFT-based signal processing as a proof of concept for the potential of using UWB signals for detection of respiration and heart rate.

2.2 Measurement Setup

The basic measurement setup is shown in Figure 2.2. The transmit and receive antennas used are TEM horn antennas directed toward the target. Note that the target can be located behind an obstruction such as a wall. The transmit antenna is connected to a pulser with a Pulse-Repetition Frequency (PRF) of 100kHz which generates pulses with a width of 1 nanosecond. The pulser also triggers an oscilloscope (Tektronix CSA8000 Communication Signal Analyzer) which is connected to the receive antenna. The time resolution δ_τ for measuring the received waveforms is 2 picoseconds. The interval between successive recorded waveforms is $T_s = 0.025$ seconds. The total measurement time is typically about 60 seconds. For the sake of clarification, we define the term “*fast-time*” as the time axis along each received waveform, denoted by τ , which is typically on the order of picoseconds. The time-

axis of all recorded waveforms is termed “*slow-time*” and denoted by t which is typically on the order of seconds. For the experimental setting in this paper, the sampling frequency f_s for *fast-time* is 500GHz and the sampling frequency F_s for *slow-time* is 40Hz. The total measuring time T_{mea} is around 60 seconds. Since the maximum heart rate is usually under 220 bpm which is less than $f_{max} = 4\text{Hz}$, the *slow-time* sampling frequency F_s satisfies Nyquist theory.

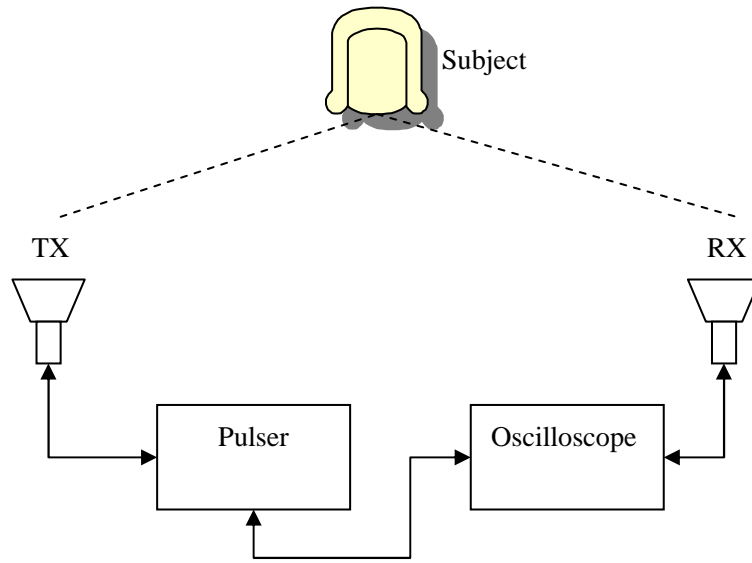


Figure 2.2: Measurement Setup

2.3 Mathematical Formulation

Assuming that the displacement of the chest cavity is a sinusoidal function of time, the location of the skin-air interface relative to the transceiver location can be expressed as [1], [16]

$$d_l(t) = d_0 + \Delta_d \sin(2\pi f_b t) \quad (2.4)$$

where d_0 is the mean distance and f_b is the frequency of the sinusoidal variation caused by chest movement. Δ_d represents the maximum deviation in the distance. Note that due to separate respiratory and heartbeat signals, there may be multiple frequency components existing in the above function. From Fourier Series theory, any time-varying periodic displacement can be viewed as a combination of a series a single-tone signals. Therefore, for the ease of analysis and without loss of generality, we assume a single tone with frequency f_b . If we assume the that the environment is static, this movement is manifested in a time-varying channel impulse response $h(t, \tau)$

$$h(t, \tau) = \underbrace{\sum_i \alpha_i \delta(\tau - \tau_i)}_{\text{static channel}} + \underbrace{\alpha_b \delta[\tau - \tau_b(t)]}_{\text{sinusoidal variations}} \quad (2.5)$$

where $\tau_b(t)$ is given by

$$\tau_b(t) = \frac{d_t(t)}{c} = \frac{d_0 + \Delta_d \sin(2\pi f_b t)}{c} = \frac{d_0}{c} + \frac{\Delta_d \sin(2\pi f_b t)}{c} = \tau_0 + \tau_d \sin(2\pi f_b t) \quad (2.6)$$

where $\tau_d = \frac{\Delta_d}{c}$ is the maximum variation in the time-of-arrival.

Each recorded waveform is a signal measured by the receive antenna and can be written as the convolution of the transmit pulse and the channel (ignoring the pulse distortion). Ignoring noise, the received signal measured at *slow-time* t_0 can be written as

$$\begin{aligned} r(t_0, \tau) &= p(t) * h(t_0, \tau) = p(t) * \left(\left[\sum_i \alpha_i \delta(\tau - \tau_i) \right] + \alpha_b \delta[\tau - \tau_b(t_0)] \right) \\ &= \sum_i \alpha_i p(\tau - \tau_i) + \alpha_b p[\tau - \tau_b(t_0)] \end{aligned} \quad (2.7)$$

A typical recorded waveform is shown in Figure 2.3. In the real application, we measure the

received waveforms at discrete instants in *slow-time* $t = mT_s$,

$$r(mT_s, \tau) = \sum_i \alpha_i p(\tau - \tau_i) + \alpha_b p[\tau - \tau_b(mT_s)] \quad (2.8)$$

$$m = 1, 2, \dots, N_w$$

At the receiver, the signal is sampled at the rate of $f_s = \frac{1}{\delta_\tau}$ in *fast-time* as well and this results in a discrete-time sequence of the received waveform samples. In order to record the chest motion information for individuals within a certain range, we need to set the proper delay time and recording time window τ_{max} along the *fast-time* axis at the receiver to collect the complete variation information. Therefore, each recorded waveform contains $N_s = \frac{\tau_{max}}{\delta_\tau}$ sample points, and can be expressed as

$$r[m, n] = r(mT_s, n\delta_\tau) = \sum_i \alpha_i p(n\delta_\tau - \tau_i) + \alpha_b p[n\delta_\tau - \tau_b(mT_s)] \quad (2.9)$$

$$m = 1, 2, \dots, N_w; \quad n = 1, 2, \dots, N_s;$$

These values are stored in a $(N_w \times N_s)$ matrix $\mathbf{R} = \{r[m, n]\}$, $1 \leq m \leq N_w$, $1 \leq n \leq N_s$. A row of the matrix \mathbf{R} , denoted by \mathbf{r}_i , represented the samples corresponding to the i th sample received waveform.

In order to extract the sinusoidal variation information from the matrix, we first need to eliminate the “background clutter”. We assume that the environment is static, and the only motion present is that of the target’s displacements of the chest cavity and cardiac muscle. Therefore, the background clutter consists of multipath corresponding to stationary scatterers in the multipath environment. Since we would like to separate moving scatters from stationary scatterers, a “motion filter” is applied to the data which removes the stationary components. The easiest way of doing this is to simply average all the rows in the matrix

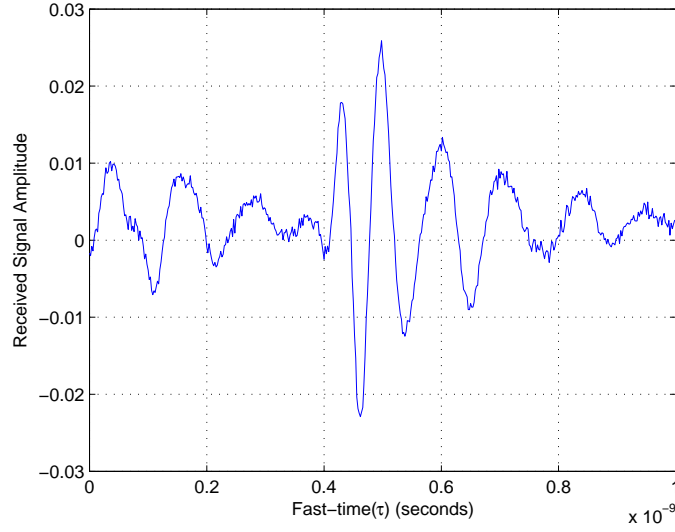


Figure 2.3: A sample received signal waveform in fast-time

\mathbf{R} and then subtract this average from the individual rows of the matrix. The average of all rows, which we denote by r_{av} , captures all the “constant” features of the signal. Subtracting this from each row results in a signal $d_i = r_i - r_{av}$ which contains signal components that vary across the set of signals.

Figures 2.4 and 2.5 show sample output of the measured data after passing the matrix \mathbf{R} through the MT filter. To gain insight into the operation of this MT filter, we characterize the output of the MT filter. From (2.9), the samples $r_{mn} = r[m, n]$ in the m th row \mathbf{r}_m of the matrix \mathbf{R} can be represented by

$$r_{mn} = \sum_i \alpha_i p(n\delta_\tau - \tau_i) + \alpha_b p[n\delta_\tau - \tau_b(mT_s)] \quad (2.10)$$

The “background reference” vector \mathbf{r}_{av} is given by

$$\mathbf{r}_{av} = \frac{1}{N_w} \sum_{m=1}^{N_w} \mathbf{r}_m \quad (2.11)$$

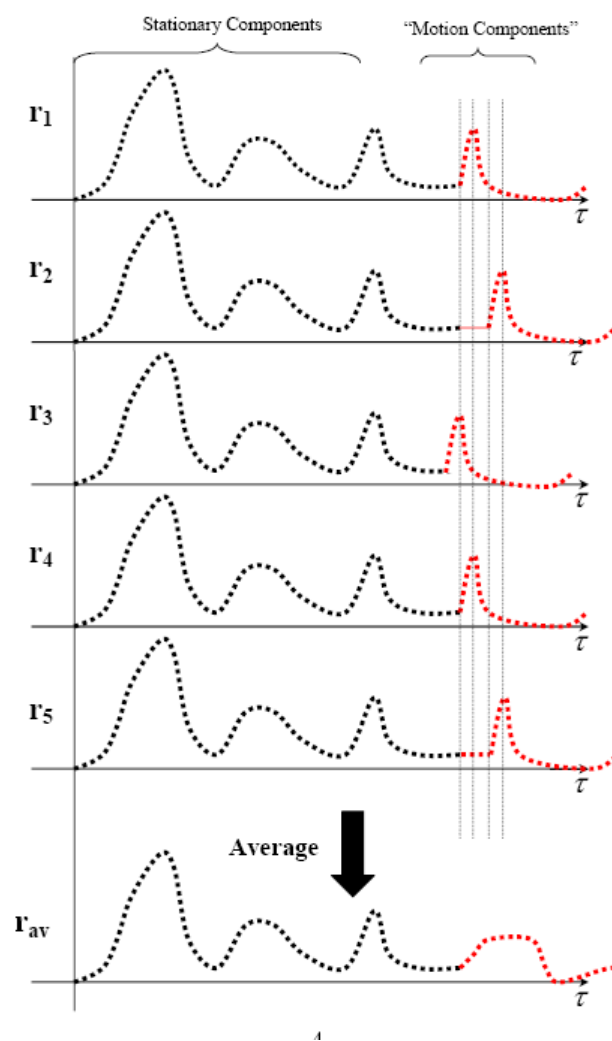


Figure 2.4: Computation of Background Clutter by averaging (From [1])

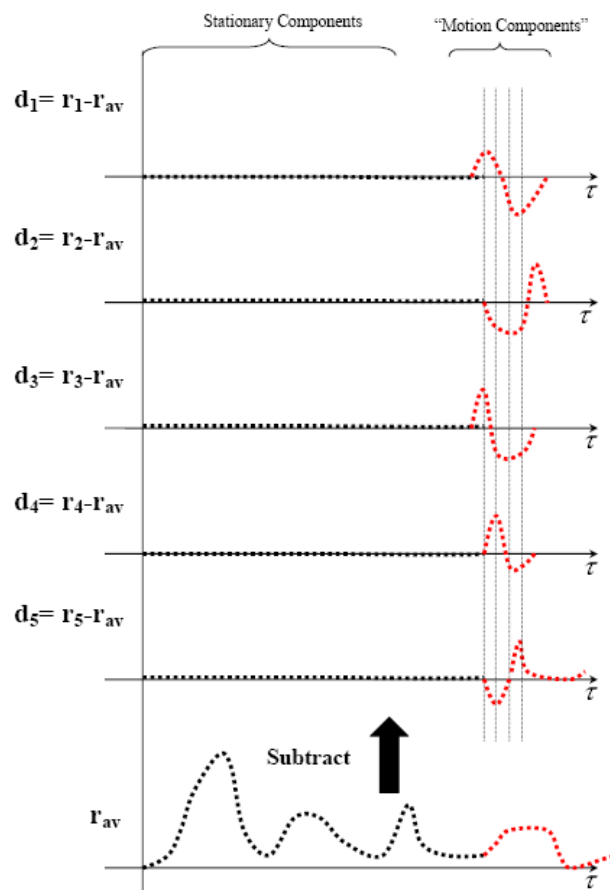


Figure 2.5: Output after Motion-Filter processing (From [1])

Therefore, the elements of \mathbf{r}_{av} are given by

$$\begin{aligned}
 r_{av,n} &= \frac{1}{N_w} \sum_{m=1}^{N_w} r_{mn} \\
 &= \frac{1}{N_w} \sum_{m=1}^{N_w} \left(\sum_i \alpha_i p(n\delta_\tau - \tau_i) + \alpha_b p[n\delta_\tau - \tau_b(mT_s)] \right) \\
 &= \underbrace{\sum_i \alpha_i p(n\delta_\tau - \tau_i)}_{\text{background clutter}} + \underbrace{\frac{\alpha_b}{N_w} \sum_{m=1}^{N_w} p[n\delta_\tau - \tau_b(mT_s)]}_{\text{average of time-varying terms}}
 \end{aligned} \tag{2.12}$$

Then the output of the MT is given by \mathbf{d}_m

$$\mathbf{d}_m = \mathbf{r}_m - \mathbf{r}_{av} \tag{2.13}$$

The elements of the row \mathbf{d}_m are given by

$$\begin{aligned}
 d_{mn} &= r_{mn} - r_{av,n} \\
 &= \left(\sum_i \alpha_i p(n\delta_\tau - \tau_i) + \alpha_b p[n\delta_\tau - \tau_b(mT_s)] \right) \\
 &\quad - \left(\sum_i \alpha_i p(n\delta_\tau - \tau_i) + \frac{\alpha_b}{N_w} \sum_{k=1}^{N_w} p[n\delta_\tau - \tau_b(kT_s)] \right) \\
 &= \alpha_b p(n\delta_\tau - \tau_b(mT_s)) - \underbrace{\frac{\alpha_b}{N_w} \sum_{k=1}^{N_w} p[n\delta_\tau - \tau_b(kT_s)]}_{\text{averaged variation}} \\
 &= \alpha_b p[n\delta_\tau - \tau_b(mT_s)] - d_0(n)
 \end{aligned}$$

Let us denote the N_w -point Fast Fourier transform (FFT) of d_{mn} along *slow-time* by $D(k, n)$.

We have the following FFT relation

$$\begin{aligned}
 D(k, n) &= \sum_{m=1}^{N_w} d_{mn} \exp(-j \frac{2\pi mk}{N_w}) \\
 &= \sum_{m=1}^{N_w} (\alpha_b p [n\delta_\tau - \tau_b(mT_s)] - d_0(n)) \exp(-j \frac{2\pi mk}{N_w}) \\
 &= \alpha_b \sum_{m=1}^{N_w} p [n\delta_\tau - \tau_b(mT_s)] \exp(-j \frac{2\pi mk}{N_w}) - N_w d_0 \delta_\kappa(k)
 \end{aligned}$$

where $\delta_\kappa(\cdot)$ is the Kronecker delta function.

2.3.1 Continuous-Time Signal Processing

For notational ease, more generally, considering continuous-time, the output of motion-filter would be

$$\begin{aligned}
 d(\tau, t) &= r(\tau, t) - \lim_{T \rightarrow \infty} \frac{1}{T} \int_{-T}^T r(\tau, t) dt \\
 &= \alpha_b p [\tau - \tau_b(t)] - \underbrace{\lim_{T \rightarrow \infty} \frac{1}{T} \int_{-T}^T \alpha_b p [\tau - \tau_b(t)] dt}_{d_0(\tau)}
 \end{aligned} \tag{2.14}$$

and we have the relation

$$\begin{aligned}
 D(\tau, f) &= \int_{-\infty}^{\infty} d(\tau, t) e^{-j2\pi ft} dt \\
 &= \int_{-\infty}^{\infty} [\alpha_b p (\tau - \tau_b(t)) - d_0(\tau)] e^{-j2\pi ft} dt \\
 &= \alpha_b \int_{-\infty}^{\infty} \underbrace{p(\tau - \tau_b(t))}_{x(\tau, t)} e^{-j2\pi ft} dt - d_0(\tau) \delta_D(f)
 \end{aligned} \tag{2.15}$$

where $\delta_D(\cdot)$ is the Dirac delta function. The term $x(\tau, t)$ can be written in terms of its

Fourier transform in *fast-time*, i.e., the (ν, t) domain

$$\begin{aligned}
 X(\nu, t) &= \int_{-\infty}^{\infty} p(\tau - \tau_b(t)) e^{-j2\pi\nu\tau} d\tau \\
 &= e^{-j2\pi\nu\tau_b(t)} \int_{-\infty}^{\infty} p(\tau) e^{-j2\pi\nu\tau} d\tau \\
 &= e^{-j2\pi\nu\tau_b(t)} P(\nu)
 \end{aligned} \tag{2.16}$$

where $P(\nu) = \int_{-\infty}^{\infty} p(\tau) e^{-j2\pi\nu\tau} d\tau$ is the Continuous Time Fourier Transform (CTFT) of the pulse-shape $p(\tau)$. Therefore, from (2.16), $x(\tau, t)$ can be written as the inverse Fourier transform of $X(\nu, t)$

$$x(\tau, t) = \int_{-\infty}^{\infty} P(\nu) e^{j2\pi\nu(\tau - \tau_b(t))} d\nu \tag{2.17}$$

Using (2.15) and (2.17), we can write

$$\begin{aligned}
 D(\tau, f) &= \alpha_b \int_{-\infty}^{\infty} p(\tau - \tau_b(t)) e^{-j2\pi ft} dt - d_0(\tau) \delta_D(f) \\
 &= \alpha_b \int_{-\infty}^{\infty} \left[\int_{-\infty}^{\infty} P(\nu) e^{j2\pi\nu(\tau - \tau_b(t))} d\nu \right] e^{-j2\pi ft} dt - d_0(\tau) \delta_D(f) \\
 &= \alpha_b \int_{-\infty}^{\infty} P(\nu) \underbrace{\left[\int_{-\infty}^{\infty} e^{-j2\pi\nu\tau_b(t)} e^{-j2\pi ft} dt \right]}_{Z(\nu, f)} e^{j2\pi\nu\tau} d\nu - d_0(\tau) \delta_D(f)
 \end{aligned} \tag{2.18}$$

Based on the assumption $\tau_b(t) = \tau_0 + \tau_d \sin(2\pi f_b t)$, we have

$$\begin{aligned}
 Z(\nu, f) &= \int_{-\infty}^{\infty} e^{-j2\pi\nu\tau_b(t)} e^{-j2\pi ft} dt \\
 &= \int_{-\infty}^{\infty} e^{-j2\pi\nu(\tau_0 + \tau_d \sin(2\pi f_b t))} e^{-j2\pi ft} dt \\
 &= e^{-j2\pi\nu\tau_0} \int_{-\infty}^{\infty} e^{-j2\pi\nu\tau_d \sin(2\pi f_b t)} e^{-j2\pi ft} dt \\
 &= e^{-j2\pi\nu\tau_0} \int_{-\infty}^{\infty} e^{-j\gamma \sin(2\pi f_b t)} e^{-j2\pi ft} dt
 \end{aligned} \tag{2.19}$$

The function $e^{-j\gamma \sin(2\pi f_b t)}$ can be expanded as a series of the first order Bessel Functions $J_l(\cdot)$

$$e^{-j\gamma \sin(2\pi f_b t)} = \sum_{l=-\infty}^{\infty} J_l(\gamma) e^{-j2\pi l f_b t} \tag{2.20}$$

Therefore,

$$\begin{aligned}
 Z(\nu, f) &= e^{-j2\pi\nu\tau_0} \sum_{l=-\infty}^{\infty} J_l(\gamma) \int_{-\infty}^{\infty} e^{-j2\pi(f+l f_b)t} dt \\
 &= e^{-j2\pi\nu\tau_0} \sum_{l=-\infty}^{\infty} J_l(\gamma) \delta_D(f + l f_b)
 \end{aligned} \tag{2.21}$$

where $\gamma = 2\pi\nu\tau_d = \beta\nu$, where $\beta = 2\pi\tau_d$. We now return to the expression for $D(\tau, f)$:

$$\begin{aligned}
 D(\tau, f) &= \alpha_b \int_{-\infty}^{\infty} P(\nu) Z(\nu, f) e^{j2\pi\nu\tau} d\nu - d_0(\tau) \delta_D(f) \\
 &= \alpha_b \int_{-\infty}^{\infty} P(\nu) \left[\sum_{l=-\infty}^{\infty} J_l(\gamma) \delta_D(f + lf_b) \right] e^{j2\pi\nu(\tau-\tau_0)} d\nu - d_0(\tau) \delta_D(f) \\
 &= \alpha_b \sum_{l=-\infty}^{\infty} \delta_D(f + lf_b) \underbrace{\int_{-\infty}^{\infty} J_l(2\pi\nu\tau_d) P(\nu) e^{j2\pi\nu(\tau-\tau_0)} d\nu}_{\Omega_l(\tau)} - d_0(\tau) \delta_D(f) \\
 &= \alpha_b \sum_{l=-\infty}^{\infty} \delta_D(f + lf_b) \Omega_l(\tau) - d_0(\tau) \delta_D(f) \\
 &= [\alpha_b \Omega_0(\tau) - d_0(\tau)] \delta_D(f) + \alpha_b \left(\sum_{l=-\infty, l \neq 0}^{\infty} \delta_D(f + lf_b) \Omega_l(\tau) \right) \quad (2.22)
 \end{aligned}$$

Therefore, we see that the CTFT of $d(\tau, t)$ consists of a train of impulses at the harmonics of the sinusoidal variation frequency f_b . The magnitude of the harmonics in $|D(\tau, f)|$ are determined by *fast-time* instant τ , β and $P(\nu)$.

2.3.2 Finite Record Length

In our case, we have the data $r(\tau, t)$ between $t = t_{start}$ and $t = t_{end} = t_{start} + T_{meas}$, thus we actually use the Short-term Fourier Transform. The CTFT of output of the motion filter

$D(\tau, f)$ is equivalent to

$$\begin{aligned}
 D_{short}(\tau, f) &= \int_{t_{start}}^{t_{start}+T_{meas}} d(\tau, t) e^{-j2\pi ft} dt \\
 &= \int_{-\infty}^{\infty} \text{rect}\left(\frac{t-t_{start}}{T_{meas}}\right) d(\tau, t) e^{-j2\pi ft} dt \\
 &= D(\tau, f) * \underbrace{(T_{meas} e^{-j2\pi f t_{start}} \text{sinc}(f T_{meas}))}_{\phi(f)} \\
 &= D(\tau, f) * \phi(f)
 \end{aligned} \tag{2.23}$$

where $\text{rect}(\frac{t}{T})$ denotes a rectangular window of width T centered around the origin, and $\text{sinc}(x) = \frac{\sin(\pi x)}{\pi x}$. From (2.23), we have

$$D_{short}(\tau, f) = [\alpha_b \Omega_0(\tau) - d_0(\tau)] \phi(f) + \alpha_b \left(\sum_{l=-\infty, l \neq 0}^{\infty} \phi(f + l f_b) \Omega_l(\tau) \right) \tag{2.24}$$

This means windowing “spreads” the frequency lines at harmonics of f_b . Therefore, by looking at the spectrum of the data along *slow-time*, we can identify the variation rate.

2.3.3 Effect of Fast-time Index, Modulation Index and Pulse Width

Recalling that $\Omega_l(\tau) = \int_{-\infty}^{\infty} J_l(2\pi\nu\tau_d) P(\nu) e^{j2\pi\nu(\tau-\tau_0)} d\nu$, it can be verified that $|\Omega_l(\tau)|$ is maximized at $\tau = \tau_0$:

$$\Omega_l(\tau_0) = \int_{-\infty}^{\infty} J_l(\beta\nu) P(\nu) d\nu. \tag{2.25}$$

If we define the modulation index as

$$\beta = 2\pi\tau_d \tag{2.26}$$

we can draw parallels to frequency modulation (FM) concepts. FM analysis states that the bandwidth of the FM signal depends strongly on the modulation index (which is defined as the maximum change in the carrier's frequency due to the modulating signal). In our case, the modulation index determines the maximum delay of the pulse which depends on the motion of the chest cavity. Carson's rule for FM signals states that the $(\beta + 1)$ th frequency harmonic is negligible compared to frequency components with lower indices. Therefore, if β is small, this means that we have very few strong frequency harmonics. Specifically, in our case, large β means $\tau_d > \tau_p$, where τ_p is the width of the UWB pulse. On the other hand, small β stands for $\tau_d < \tau_p$.

As shown in Figure 2.6, for large β , we will observe a large number of frequency harmonics. In contrast, for small β , we can obtain a single strong peak at the main variation rate f_b illustrated in Figure 2.7. This can be used to determine the pulse width required so that the low but strong respiration rate can be determined directly and its harmonics' influence on the weak heart rate signals is reduced. In our measurement setup, the pulse width of 1 nanosecond is roughly equivalent to 30 centimeters and is much larger than typical expansion of the chest cavity. This is beneficial since it means that the bandwidth of the pulse need not be multiple GHz to achieve good accuracy.

2.4 Simulation Results

The general procedure of this FFT-based algorithm is illustrated in Figure 2.8 and was evaluated via simulation using MATLAB. In Section 2.3.3, we showed that if the received pulse width τ_p is larger than τ_d , we can obtain a single strong peak at the main variation rate f_b . This analysis was based on the assumption of non-distortion of the received pulses which is a Gaussian-like shape. However, in real experiments, the UWB pulses are distorted

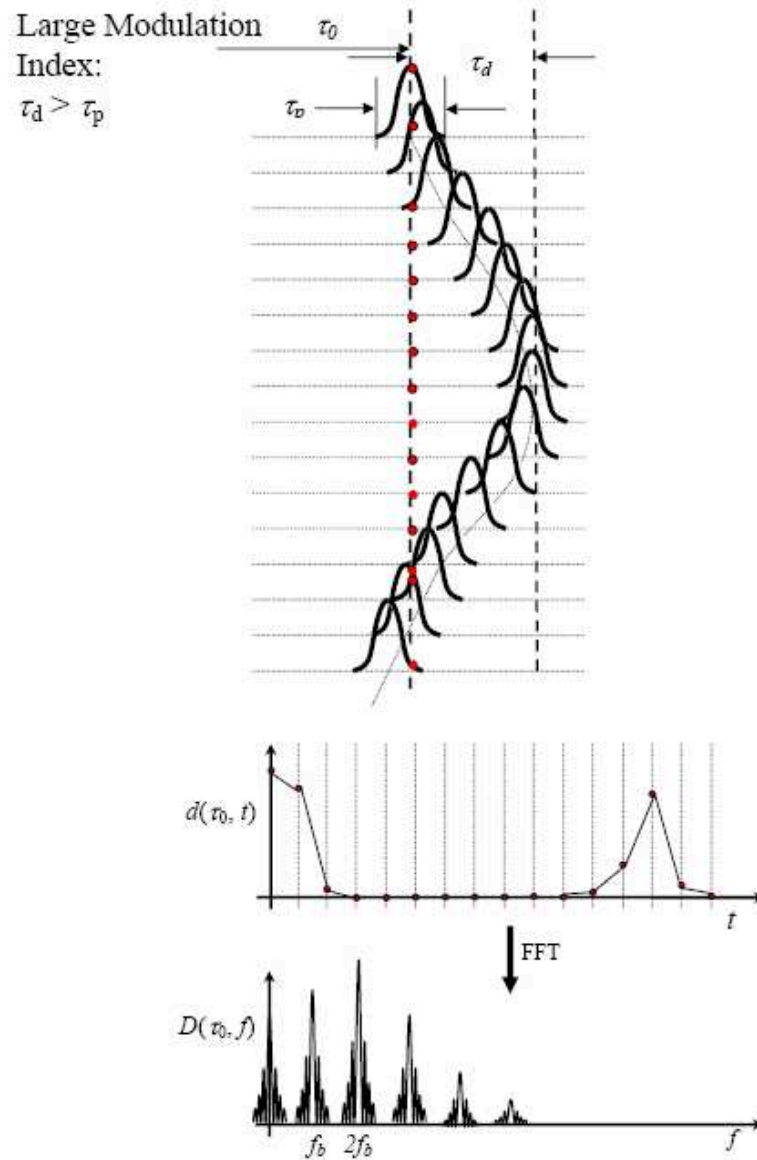


Figure 2.6: Large modulation index results in several peaks at the harmonics of f_b (From [1])

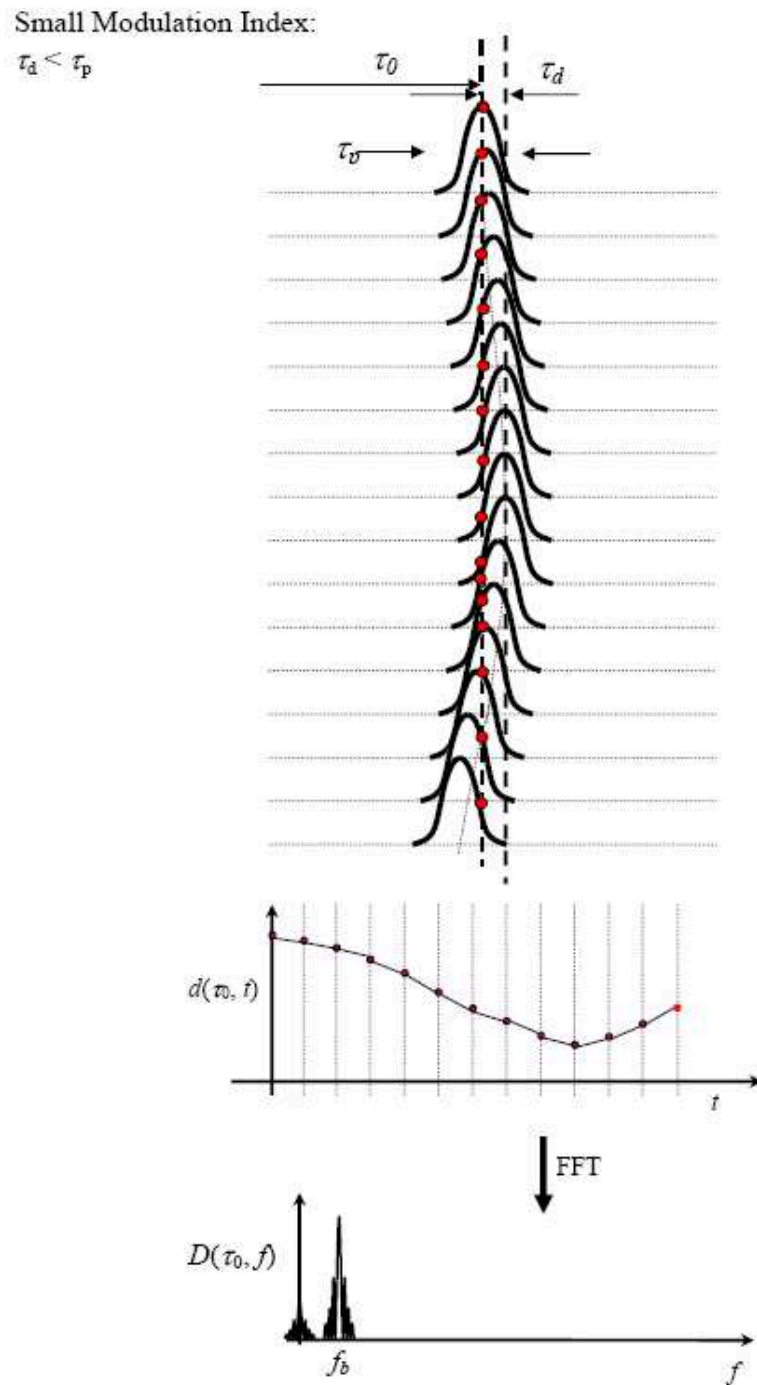


Figure 2.7: Small modulation index results in a single strong peak at f_b (From [1])

by amplifier, antennas and human body. The shape of the received waveform is like a damped sinusoidal function as shown in Figure 2.3. Therefore, in order to reflect the real situation, we use a sample received waveform from the experimental data to be the basic echo pulse for our simulations instead of using the ideal Gaussian-shape pulse. Additionally, we assumed that the data was obtained from a subject seated still on a chair and remained perfectly still. Thus, the only motion component in the data was due to breathing and heartbeat movement. Further, we assumed that the motion induced by breathing and the beating heart were sinusoidal. The maximum deviation Δ_r of the chest wall movement due to respiration was assumed to be 10mm, and Δ_h associated with cardiac muscle expansion-contraction movement was assumed to be 1mm. Other related parameters, such as the *fast-time* and *slow-time* sampling frequencies, are kept identical to the actual measurement setup discussed in Section 2.2. Figures 2.9 and 2.10 illustrate an example of the simulated *slow-time* variation along the range bin containing the maximum energy in both the time domain (termed the *observed trajectory*) and the frequency domain.

From the spectrum of the target trajectory (in Figure 2.10), the second-order (2nd) and the third-order (3rd) harmonics of the respiratory signal are clearly discernible in the spectra. It can be inferred that if the target breaths heavily, the magnitude of the high-order harmonics of respiratory signal will grow stronger. Additionally, if the target's respiration rate increases, the strong-magnitude harmonics may move closer to the location of the heartbeat frequency. Clearly the harmonics of the respiratory signal can be a source of interference for detecting the heartbeat frequency. In a second example spectrum shown in Figure 2.11 where the respiration rate is 0.4Hz (15 breaths/min), the fourth-order harmonic of the respiration signal falls near heartbeat frequency which causes major difficulty in heartbeat rate detection as we shall see.

The average error magnitude of respiration and heartbeat rate (in beats or breaths per

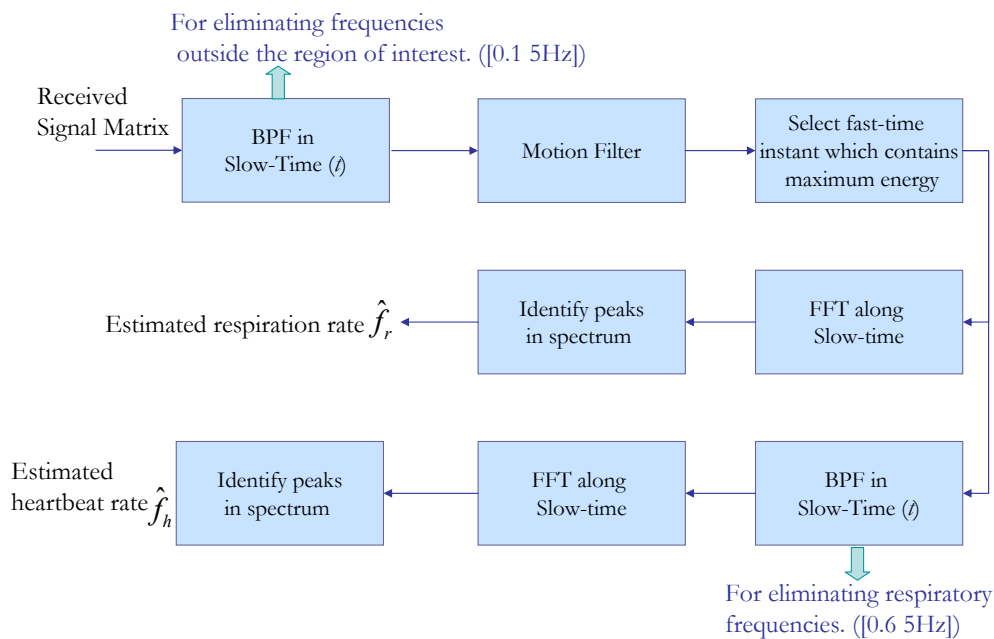


Figure 2.8: Flow chart of FFT-based algorithm

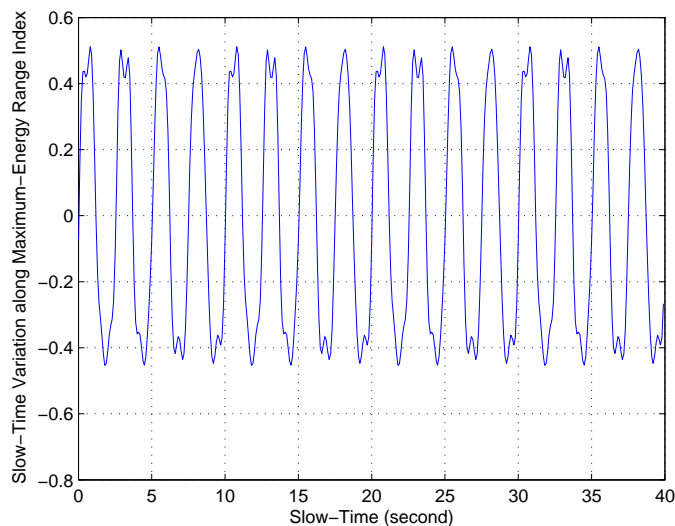


Figure 2.9: Slow-time range bin which contains the maximum energy, assuming the breathing rate is 0.2Hz and Heartbeat rate is 1.5Hz

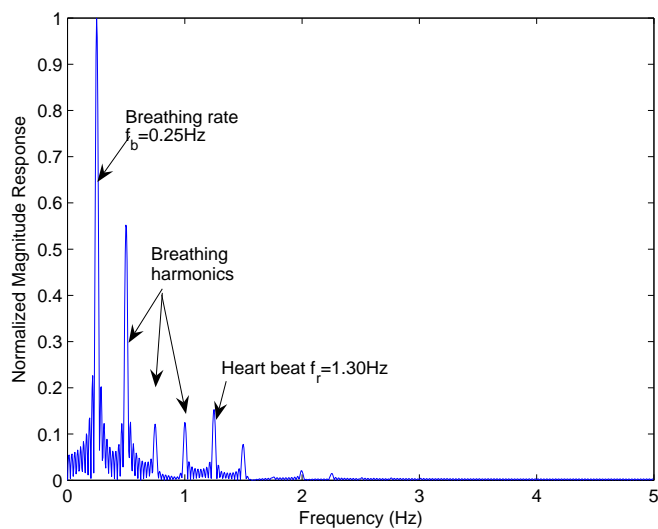


Figure 2.10: Frequency content of the slow-time range bin which contains the maximum energy, assuming the breathing rate is 0.2Hz and Heartbeat rate is 1.5Hz

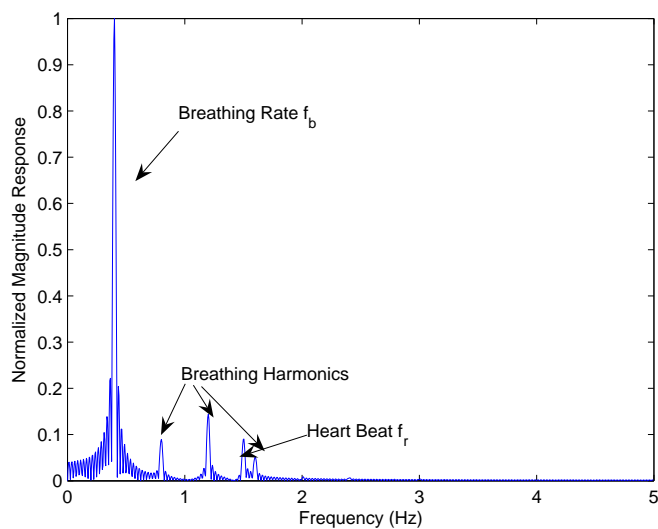


Figure 2.11: Frequency content of the slow-time range bin which contains the maximum energy, assuming the breathing rate is 0.4Hz and Heartbeat rate is 1.5Hz

minute) versus Signal-to-Noise Ratio (SNR) based on simulation is shown in Figure 2.12. In this simulation, the heartbeat movement was assumed to be stationary and 20dB weaker than the respiratory signal. The respiration rate was random over 2000 simulations and uniformly distributed between 12 and 25 breaths per minute (0.2-0.4Hz). The heartbeat rate was uniformly distributed from 60 to 100 beats per minutes (1-2Hz). The average error is plotted versus the average SNR of the received signal. The relationship between this average SNR and the SNR of the target trajectory is somewhat complicated, so that the absolute SNR value is perhaps not as important as the relative performance. From the simulation, we can note several things.

- First, for breathing rate estimation, the estimator works very well even in low SNR.
- The respiration rate estimation experiences an error floor due to the fact that there is a finite resolution in the frequency analysis which can be reduced by increasing the FFT size (at the expense of additional complexity).
- The observed error floor of heartbeat estimation is substantially higher than that associated with breathing rate. This is due to the interference from higher order harmonics of the respiratory signal. Even though we applied a bandpass filter with passband at 0.7 – 4Hz in order to remove respiratory signal, the harmonics may still fall into the passband of the filter as discussed above. The average error of approximately 4bpm is due to a large number of true heartbeat rate estimates with very small error (0.1bpm) due to resolution, and a smaller number of false detection with very high error (20-40bpm) which are the result of interference caused by respiratory signal harmonics. It indicates that the respiratory signal is a major interference which will result in false detection with great error, and is irrelevant with SNR.

Figure 2.13 illustrates the distribution of the error of the estimated heartbeat frequency

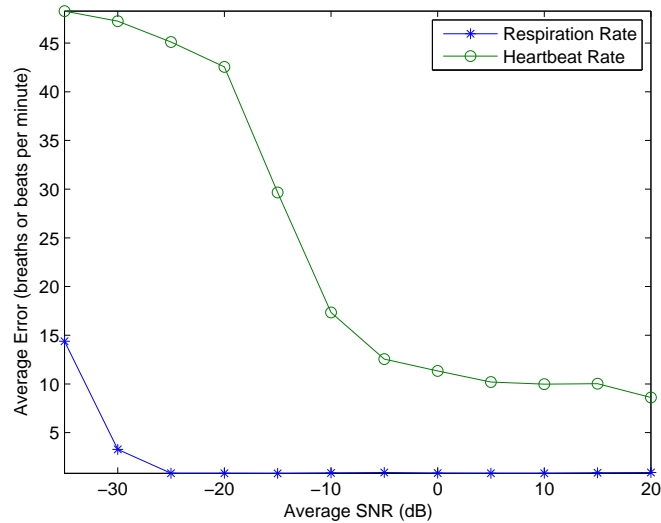


Figure 2.12: Average error of FFT-based breathing and heartbeat rate estimation from simulation

at SNR= 20dB over 200 simulations. We can find that a big cluster is close to zero which indicates the successful detection of true heartbeat frequency. There is also a smaller cluster around the large error values. After examining these estimated frequency, we find out that the estimated heartbeat rates with great error corresponds to the respiratory harmonics frequencies. This shows that even in high SNR environment, the respiratory harmonic is still a interference for accurate heartbeat estimation.

2.5 Experimental Results

In addition to the simulation results, we also processed real measurements taken as described in Section 2.2. The results of ten representative experiments, processed by FFT-based approach described above, are given in Table 2.1.

As can be seen, the technique accurately estimates breathing rate. Over 10 separate exper-

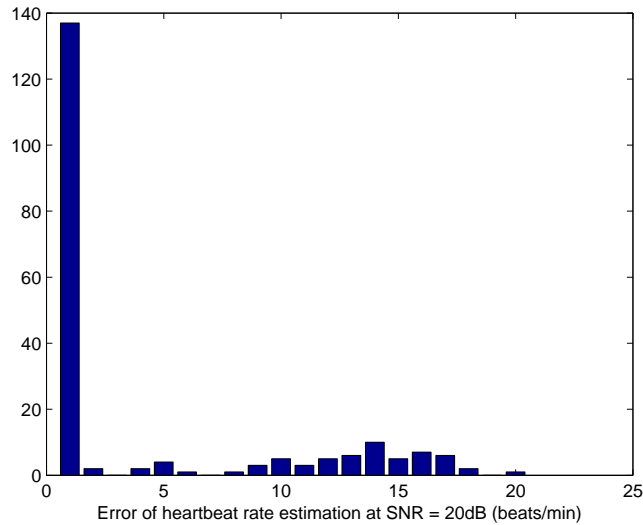


Figure 2.13: Distribution of estimation error of the heartbeat rate at SNR=20dB

iments, the error is approximately 9% on average, with a maximum error of about 57% and a minimum error of approximately 1%. The worst case occurred in Experiment 10 and 13, where the breathing rate estimate was off by approximately 30% and 57%. The error in this case was found to be due to relatively large scale movement of the body that caused frequency components appearing in the breathing rate band (0.1-0.5Hz), which is regarded as a false detection.

The heart rate estimate, however, shows much greater variation, as is expected. Like in the simulation results, this is due to (a) a lower SNR and (b) interference from harmonics of the respiratory signal that fall within the frequency band where the heart rate is expected. For example in Experiments 2,5,7, the estimated heartbeat rate is obviously the high (second or third) order harmonics of the respiration rate, which can be regarded as false detection. The average error of heartbeat detection is roughly 23% with a maximum of 66%, which reflects the fact that while some estimates are relatively good (e.g., Experiment 4), others are very poor (e.g., Experiment 7). These results are analogous to what we saw in the simulations.

Table 2.1: Performance of the FFT-based Respiration and Heart Rate Estimation Approach

EXP	True Respiratory Rate (per min)	True Heart Rate (per min)	Estimated Respiratory Rate(per min)	Estimated Heart Rate(per min)
1	10	63	9.4	62.3
2	19	71	18.8	57.4
3	11	78	10.5	71.5
4	15	71	14.1	69.1
5	24	90	23.4	48.0
6	19	103	18.8	42.2
7	20	115	18.8	39.8
8	15	74	14.1	75.0
9	16	110	15.2	68.0
10	10	68	7.0	75.0
11	25	64	24.5	66.9
12	24	80	24.6	48.1
13	22	60	9.4	62.1
14	23	70	23.4	48.1
15	16	60	17.5	61.0

2.6 Conclusions

In this chapter, a basic measurement setup for respiration and heartbeat rate estimation is presented. A FFT-based signal processing framework for the frequency estimation of multiple periodic signals (viz. respiration and heartbeat rates) is investigated. The mathematical formula of this approach conceptually proves the capabilities of using UWB signals for the detection of respiration and heart rate. However, simulation and experimental results show that this FFT-based approach while intuitive, is not sufficient for accurate respiration and heartbeat rate estimation. Clearly, more advanced techniques are needed for reliable detection and estimation of vital-signs.

Chapter 3

Improved Single-Target Respiration Rate Estimation

3.1 Introduction

Chapter 2 demonstrates the capability of UWB signals to detect the respiration rate of a human target. Theoretically, the FFT-based approach is able to estimate accurate respiration rate even in very low SNR, as the simulation results show in Figure 2.12. However, from the experimental results, large error in respiration rate estimation occasionally occurs, e.g., 30% error in respiration rate in Experiment 10 of Table 2.1. Based on the observation of the *slow-time* variation of the received signals, we found that the large error was not caused by noise, but rather the large-scale body motion of the target during the measurement. We noticed that although the target is required to be still during the measurement, it is quite common in the received data that the motion components not only include the chest-wall displacement, but also contain slower variations which are mainly caused by large-scale body motion of the target. This is reflected in the target trajectory as mean position drifting or an

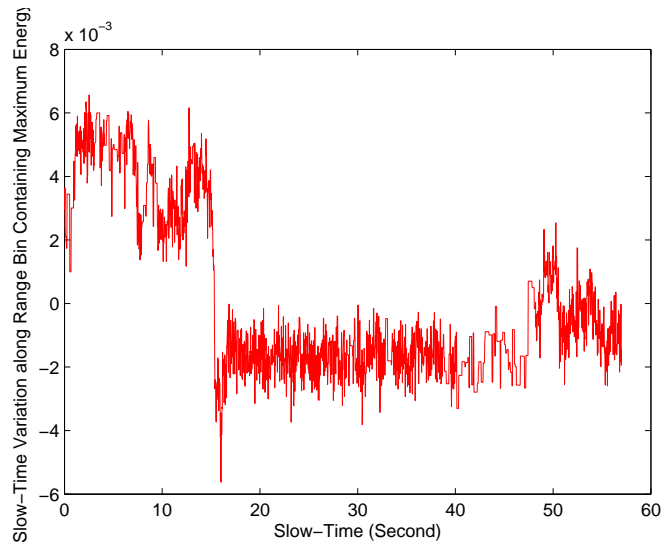


Figure 3.1: Slow-time variation along the range bin containing the maximum energy from experiment data

abrupt shift of the periodic variation along the *slow-time* domain, as shown in Figure 3.1. In the frequency domain, it exhibits as some peaks within the low frequency range. Sometimes, the relatively large-scale motion will cause strong frequency components in the lower frequency spectra and interfere with the detection of the true respiration rate.

It is intuitive to use a high-pass filter to remove the low-frequency components in the signals. However, such an approach is unreliable, mainly because it is difficult to predict the appropriate cut-off frequency to effectively block unwanted frequency components caused by the relative large-scale body motion, yet pass the respiratory signal, especially when the patient is in critical condition with a very low breathing rate. In Figure 3.2, although we have already applied a BPF with a passband frequency of 0.1-5Hz, we still observe a strong low frequency component just below 0.1Hz that was not eliminated by filtering. The signal in Figures 3.1 and 3.2 is the target trajectory from Experiment 10 in Table 2.1. This explains the large error in this experiment. Thus, our goal is to find a robust mean position compensation method which will be adaptive to different measurement environments.

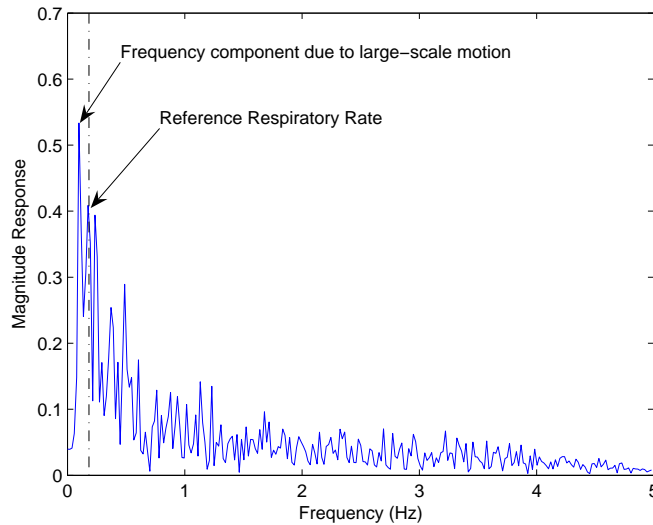


Figure 3.2: FFT of the Slow-time variation along the the range bin containing the maximum energy from experiment data

3.2 Mean Position Tracking Algorithms

For the sake of clarity, since the vector of *slow-time* variation along the range bin containing the maximum energy reflects the characteristic frequency of both the respiration and heartbeat activities, we denote it as the *observed trajectory*.

3.2.1 Moving Average Filter

The simplest way to compute local first order statistics is to use the empirical average of the observation samples in an appropriate window around each time instance. As the time instant of interest proceeds, the window moves at the same speed. Assuming the window size L to be even for simplicity of notation, the typical method of calculating the moving

average over a fixed window is formulated as,

$$x_{mean}(i) = \frac{1}{L} \sum_{j=i-L/2}^{i+L/2-1} x_j \quad (3.1)$$

The benefit of the moving average filter is its computational efficiency. However, this estimator is effective only if the window size closely matches the signal period which is unknown in our case. We applied this filter with different window length to the same observed trajectory. As shown in Figure 3.3 where the window size is close to the respiration period, the estimated mean position is smooth and reflects the true variation caused by body motion. On the other hand, when the window size L is smaller than the respiration period as illustrated in Figure 3.4, the estimated mean value exhibits undesirable oscillations following the original trajectory. In this case, once we subtract the obtained mean trajectory from the original trajectory to compensate the drifting mean position, the desired periodic signal may be attenuated or canceled which would impact the estimation. The reason for the oscillations is straightforward since the moving average filter does not take into consideration the nature of the original signal and it only averages the data within the window. With shrinking of the window size, the mean trajectory will gradually converge to the original trajectory. On the other hand, if the window size increases, the filter will become less sensitive to the mean variation and even loose tracking.

Additionally, the actual respiration motion is semi-sinusoidal and usually modeled as a *modified cosine* function [27], which is defined as,

$$x(t) = x_0 - A \cos^{2n}(\pi f_r t + \psi) \quad (3.2)$$

with $n = 2$ and where f_r is the respiration rate and A is the maximum displacement. We simulated a set of data based on this waveform to verify the performance of the moving

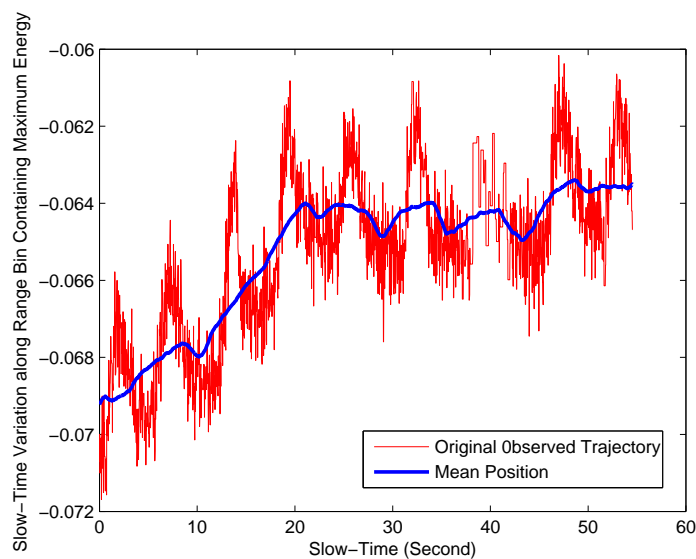


Figure 3.3: Moving average filter performance on the observed trajectory from real experiments (target's breathing period is 5.45seconds, $L = 5$ seconds)

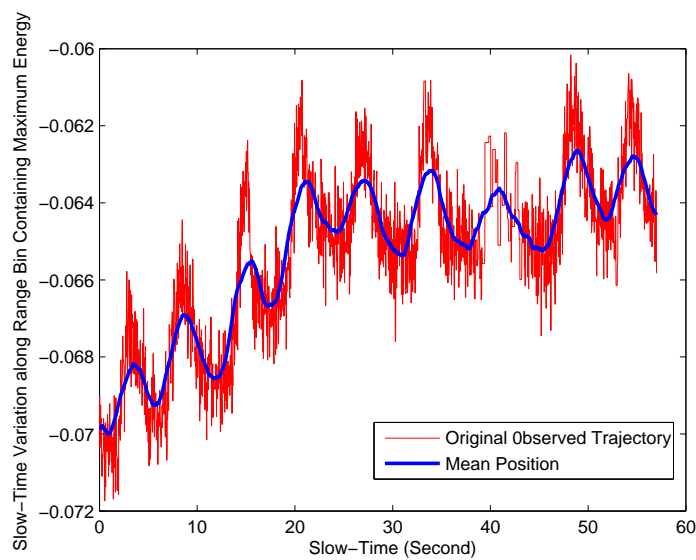


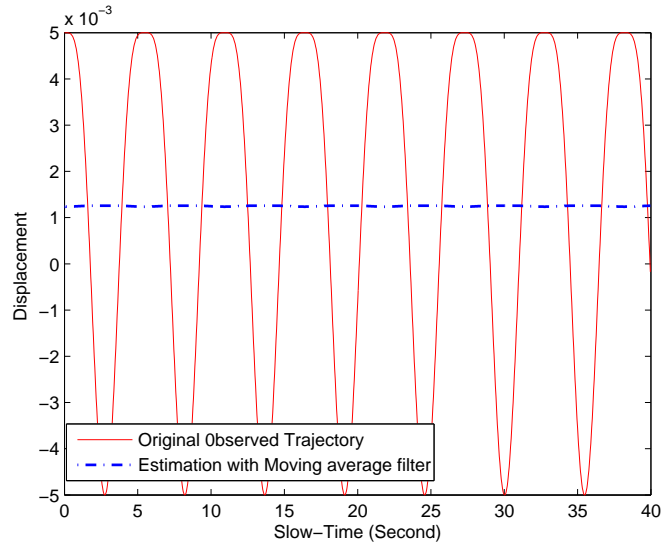
Figure 3.4: Moving average filter performance on the observed trajectory from real experiments (target's breathing period is 5.45second, $L = 3$ seconds)

average filter which is illustrated in Figure 3.5. In Figure 3.5(a), we set the window size equal to the signal period. Although the estimated mean trajectory is a smooth and stable curve, it doesn't reflect the true mean position which is zero. Further in Figure 3.5(b) where the window size is mismatched to the signal period, the estimated mean fluctuates away from the true mean. Therefore, it is obvious that the mean estimation for the ideal respiratory model using a moving average filter is not reliable and very sensitive to the window size.

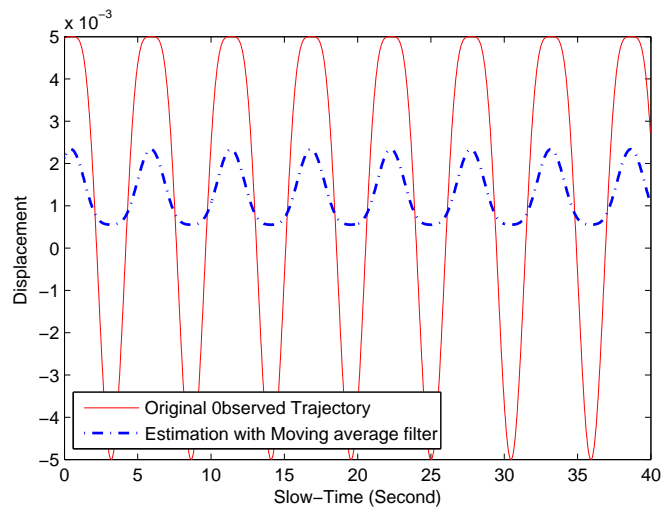
3.2.2 Ellipse Fitting Algorithm

In order to circumvent the direct filtering approach and exploit the semi-sinusoidal feature of the respiratory and heartbeat motion, we adopt another method known as the ellipse fitting algorithm introduced in [28], [29]. This approach uses a relatively low degree-of-freedom ellipse model to fit a cluster of 2-dimensional data obtained from the self-delayed version of the sinusoidal trajectory, to an ellipse. The advantage of this method is its robustness to noise and unreliable observation data.

Given a set of the one-dimensional discrete data $x_i = x(t_i)$ sampled from a sinusoidal waveform $x(t)$, we can obtain a second set of data from a delayed version of the original waveform $y_i = x(t_i - \sigma) = x_j$, where $(i - j)\Delta t = \sigma$. The particular choice of the delay length is not too crucial, and here we use $\tau = 0.5$ seconds. From these two data sets, we have a two-dimensional cluster consisting of (x_i, y_i) with $i = 1, 2, \dots, n$. The $x - y$ plot of the signals results in an elliptical shape. In order to retrieve the parameters (i.e., the instantaneous mean value) of the original sinusoidal model, we need to first compute the ellipse parameters that best fit the signals. Here, we apply the "direct ellipse fitting" algorithm introduced by [29].



(a) Performance of moving average estimation of simulated modified cosine waveform, when the period of the signal is 5.5 seconds and the window length is 5.5 seconds



(b) Performance of moving average estimation of simulated modified cosine waveform, when the period of the signal is 5.5 seconds and the window length is 4.5 seconds

Figure 3.5: Simulation results for the moving average filter for mean position tracking

The model of an ellipse can be represented by a general conic equation

$$F(\boldsymbol{\alpha}, \mathbf{x}) = \boldsymbol{\alpha}^T \mathbf{x} = ax^2 + bxy + cy^2 + dx + ey + f = 0 \quad (3.3)$$

where $\mathbf{x} = [x^2 \ xy \ y^2 \ x \ y \ 1]^T$, and $\boldsymbol{\alpha} = [a \ b \ c \ d \ e \ f]^T$, and superscript T denotes the transpose operation. Note that the discriminant must be negative for an ellipse, i.e., $b^2 - 4ac < 0$. $F(\boldsymbol{\alpha}, \mathbf{x}_i)$ is called the ‘‘algebraic distance’’ of a point (x_i, y_i) to the curve $F(\boldsymbol{\alpha}, \mathbf{x}) = 0$. The fitting of the ellipse conic can be approached by minimizing the sum of squared algebraic distances

$$D_A(\boldsymbol{\alpha}) = \sum_{i=1}^L \{F(\boldsymbol{\alpha}, \mathbf{x}_i)\}^2 \quad (3.4)$$

of the conic to the N data points \mathbf{x}_i .

In order to avoid the trivial solution $\boldsymbol{\alpha} = \mathbf{0}_6$, and recognizing that any multiple of a solution $\boldsymbol{\alpha}$ represents the same conic, the parameter vector $\boldsymbol{\alpha}$ is constrained so that the conic that it represents is forced to be an ellipse. The appropriate constraint is that the discriminant $b^2 - 4ac$ be negative. However, the imposition of the inequality constraint is difficult in general. In this case we have the freedom to arbitrarily scale the parameters, so we may simply incorporate the scaling into the constraint and impose the equality constraint $b^2 - 4ac = -1$. This is a quadratic constraint which may be expressed in the matrix form

$$\boldsymbol{\alpha}^T \mathbf{C} \boldsymbol{\alpha} = 1 \quad (3.5)$$

where $\begin{bmatrix} \tilde{\mathbf{C}} & \mathbf{0}_{3 \times 3} \\ \mathbf{0}_{3 \times 3} & \mathbf{0}_{3 \times 3} \end{bmatrix}$ and $\tilde{\mathbf{C}} = \begin{bmatrix} 0 & 0 & 2 \\ 0 & -1 & 0 \\ 2 & 0 & 0 \end{bmatrix}$, is defined as the constraint matrix. As shown by Bookstein [30], if a quadratic constraint is set on the parameters, the minimization of

(3.4) can be solved by considering a rank deficient generalized eigenvalue system. Therefore, this constrained ellipse fitting problem becomes equivalent to minimizing

$$\begin{aligned} D_A(\boldsymbol{\alpha}) &= \sum_{i=1}^L \{F(\boldsymbol{\alpha}, \mathbf{x}_i)\}^2 \\ &= \|\mathbb{X}\boldsymbol{\alpha}\|^2 = \boldsymbol{\alpha}^T \mathbb{X}^T \mathbb{X} \boldsymbol{\alpha} \end{aligned} \quad (3.6)$$

where $\mathbb{X} = [\mathbf{x}_1, \mathbf{x}_2, \dots, \mathbf{x}_L]^T$, is defined as the design matrix. It is subject to the constraint that $\boldsymbol{\alpha}^T \mathbf{C} \boldsymbol{\alpha} = 1$.

Introducing the Lagrangian multiplier λ and differentiating, we arrive at the system of simultaneous equations which can be written as

$$\begin{aligned} \mathbb{X}^T \mathbb{X} \boldsymbol{\alpha} - \lambda \mathbf{C} \boldsymbol{\alpha} &= 0 \\ \boldsymbol{\alpha}^T \mathbf{C} \boldsymbol{\alpha} &= 1 \end{aligned} \quad (3.7)$$

This may be rewritten as the system

$$\begin{aligned} \mathbf{S} \boldsymbol{\alpha} &= \lambda \mathbf{C} \boldsymbol{\alpha} \\ \boldsymbol{\alpha}^T \mathbf{C} \boldsymbol{\alpha} &= 1 \end{aligned} \quad (3.8)$$

where \mathbf{S} is the scatter matrix equal to $\mathbb{X}^T \mathbb{X}$. This system is readily solved by considering the generalized eigenvectors of (3.8). Based on Theorem 1 in [29], there is exactly one positive generalized eigenvalue which corresponds to the unique local minimum of the Lagrangian. Let us assume that (λ, \mathbf{u}) solves equation (3.7), then $\hat{\boldsymbol{\alpha}} = \mu \mathbf{u}$ is the optimal solution to the

ellipse parameters in equation (3.6), where μ is equal to

$$\mu = \sqrt{\frac{1}{\mathbf{u}^T \mathbf{C} \mathbf{u}}} \quad (3.9)$$

Therefore, as the ellipse equation is obtained with optimal vector $\hat{\mathbf{a}}$, the ellipse parameters can be extracted from the equation in terms of the principal axes, rotation angle, and center of ellipse.

Further, we want to transform the ellipse parameters to the original signal parameters. Assuming the two-dimensional cluster obtained from the the “observed trajectory” is modeled as

$$\begin{aligned} x &= a \cos(\omega t) + m \\ y &= a \cos(\omega t + \phi) + m \end{aligned} \quad (3.10)$$

it can be written in a matrix form as follows

$$\begin{bmatrix} x \\ y \end{bmatrix} = \begin{bmatrix} a \cos(\psi) & -a \sin(\psi) \\ a \cos(\phi + \psi) & -a \sin(\phi + \psi) \end{bmatrix} \begin{bmatrix} \cos(\omega t - \psi) \\ \sin(\omega t - \psi) \end{bmatrix} + \begin{bmatrix} m \\ m \end{bmatrix} \quad (3.11)$$

where ψ is an arbitrary phase (for generality). The corresponding fitted ellipse parameters consists of principle axes, k_1 and k_2 , rotation angle θ and the center of the ellipse (x_0, y_0) . Based on the parametric equation of ellipse, we can write the points (x, y) on the ellipse curve as

$$\begin{bmatrix} x \\ y \end{bmatrix} = \begin{bmatrix} k_1 \cos(\theta) & -k_2 \sin(\theta) \\ k_1 \sin(\theta) & k_2 \cos(\theta) \end{bmatrix} \begin{bmatrix} \cos(\omega t - \psi) \\ \sin(\omega t - \psi) \end{bmatrix} + \begin{bmatrix} x_0 \\ y_0 \end{bmatrix} \quad (3.12)$$

Comparing equations (3.11) and (3.12) yields the DC offset parameters,

$$m = x_0 \text{ or } m = y_0 \quad (3.13)$$

Finally, the center (x_0, y_0) of this ellipse can be parameterized by $\hat{\boldsymbol{\alpha}}$ as

$$\begin{aligned} x_0 &= \frac{2\hat{c}\hat{d} - \hat{b}\hat{e}}{\hat{b}^2 - 4\hat{a}\hat{c}} \\ y_0 &= \frac{2\hat{a}\hat{e} - \hat{b}\hat{d}}{\hat{b}^2 - 4\hat{a}\hat{c}} \end{aligned} \quad (3.14)$$

Therefore, the center of the cluster (x_0, y_0) in equation (3.14) which corresponds to the mean value of the original observed trajectory which can be obtained from the vector $\hat{\boldsymbol{\alpha}}$.

Note that we define $\mathbf{S}(t) = \mathbb{X}(t)^T \mathbb{X}(t) = \sum_{i=t-L/2+1}^{t+L/2} \mathbf{x}_i \mathbf{x}_i^T$ with L indicating the window size. As mentioned in Section 3.2, the window size L also determines the compromise between response speed (tracking efficiency) and robustness (tracking stability) for this ellipse fitting algorithm, which means it is helpful to choose a window size close to its optimal value which should be identical with the signal period. However, since the mean value is gained based on the sinusoidal nature of the trajectory, it is less sensitive to the window size as compared to the moving average filter. A simulation result based on a sinusoidal trajectory with noise illustrates the capability of the ellipse fitting algorithm for accurate mean position estimation even when the window length disagrees with the signal period. In Figure 3.6, we plot the fitted ellipse for the 2-D cluster when the window is identical to the signal period (middle) and much less than the signal period (bottom). It is clear from the fitted ellipse which is overlaid on the observation cluster, the technique outputs an accurate mean position estimate in bose cases. The bottom plot in Figure 3.6 illustrates the situation where the window size is less than the signal period, which can be regarded as the case where the observation data is only available for part of the period (the arc shape of the cluster). We noticed that

although only partial arc data is available for fitting, the fitted ellipse still provides good a approximation for the cluster and an accurate mean position estimate. This empirical study justifies our confidence in ellipse fitting method as a smooth mean estimator.

To further verify this method for our experiment, we first apply this method to the simulated *modified cosine* function which is regarded as the ideal respiratory trajectory and compare it with the moving average filter discussed in Section 3.2.1. Figure 3.7(a) shows that the ellipse fitting algorithm are not only smooth but also able to provide the true mean position (zero). In Figure 3.7(b), it is obvious that the mean position estimated from the this approach is pleasantly stable when the window size mismatches the signal period.

Next, we test this approach using data from real experiments. Since the normal breathing rate of human-beings is in the range of [4-30] breaths/min, we choose the window size to be consistent with the average of 15 breaths/min for both moving average filter and the ellipse fitting algorithm. Figures 3.8 and 3.9 demonstrate the mean tracking ability of two methods applied to experimental data. They present similar performance when the period of the signal is close to the window size as shown in Figure 3.8, but the ellipse fitting method is more stable and closer to the true mean position when the breathing period has a relatively large difference compared to the window size, as shown in Figure 3.9. (Note that for more complicated respiration-motion-related monitoring using UWB in the future, the mean position may have a more significant influence [28],[31])

Finally, after subtracting the estimated drifting mean value from the original observed trajectory, the slow variation caused by large-scale body motion has been removed and the respiratory signal becomes much easier to detect. We used the same set of experimental data shown in Figure 3.1, and applied the ellipse fitting algorithm to track the mean position. The result is shown in Figure 3.10. The FFT spectrum after the mean tracking is removed is shown in Figure 3.11. Compared with the spectrum of the original trajectory

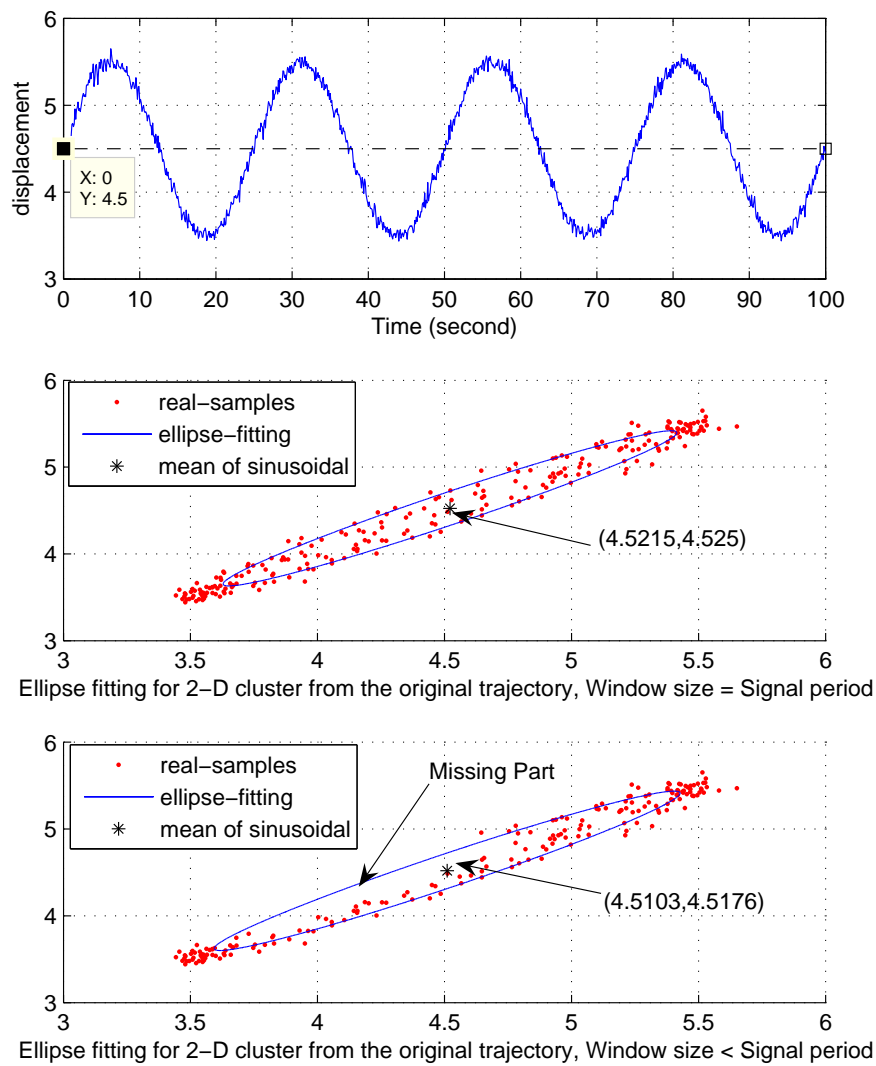
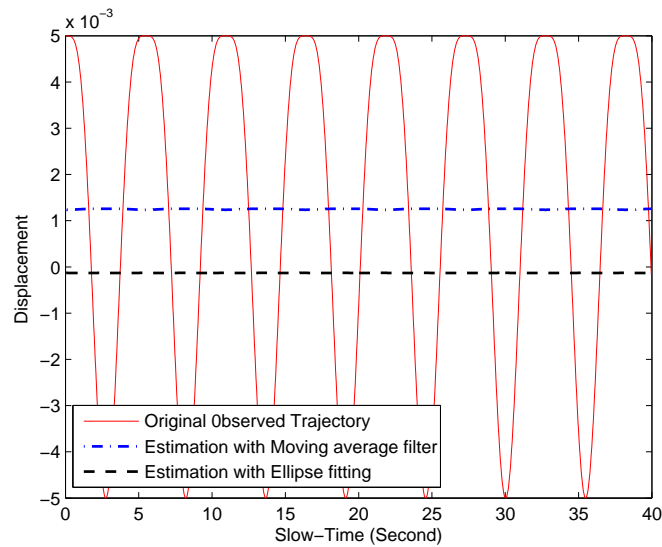
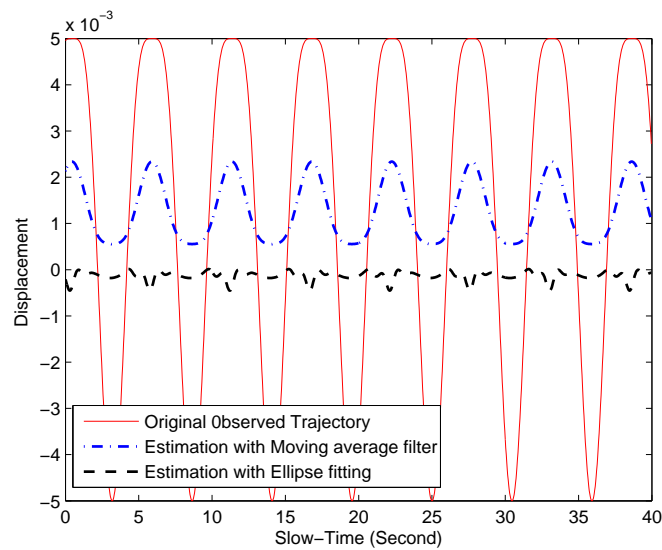


Figure 3.6: Performance of mean position estimation by ellipse fitting algorithm with different window sizes on the simulated sinusoidal trajectory



(a) Comparison of moving average and ellipse fitting estimation of simulated modified cosine waveform, when the period of the signal is 5.5 seconds and the window length is 5.5 seconds



(b) Comparison of moving average and ellipse fitting estimation of simulated modified cosine waveform, when the period of the signal is 5.5 seconds and the window length is 4.5 seconds

Figure 3.7: Comparison of simulation result of the moving average filter and ellipse fitting algorithm for mean position tracking

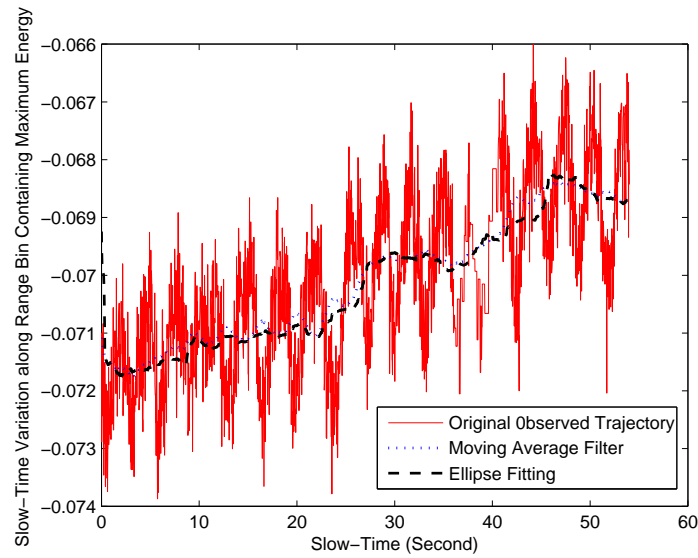


Figure 3.8: Comparison of moving average and ellipse fitting estimator for mean position tracking: window length equals to 15 breaths/min, target respiration rate is 16 breaths/min

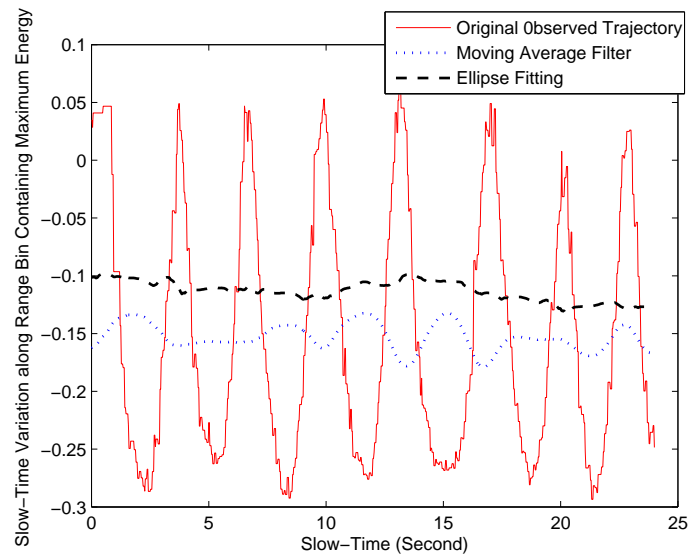


Figure 3.9: Comparison of moving average and ellipse fitting estimator for mean position tracking: window length equals to 15 breaths/min, target respiration rate is 21 breaths/min

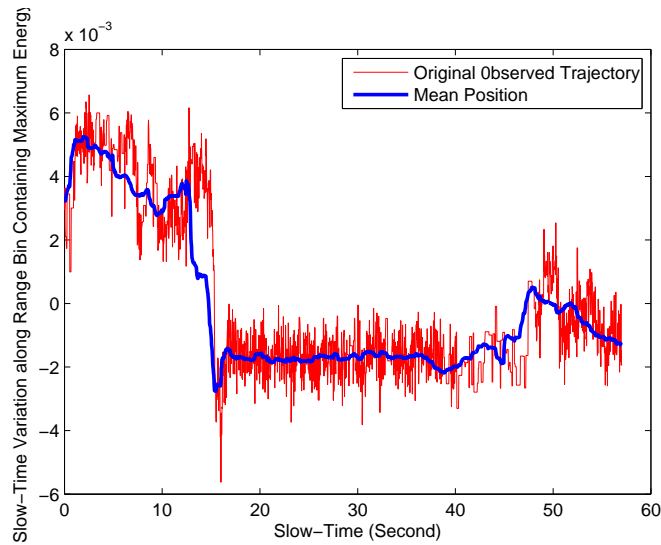


Figure 3.10: Slow-time variation along the range bin containing maximum energy from experiment data with estimated drifting mean value

in Figure 3.2, the respiratory frequency is now the largest magnitude response. Therefore, compensation of the drifting mean value provides some resistance to false detection due to body motion.

3.3 Experimental Results

The same experimental data given in Table 2.1 was processed using the ellipse fitting algorithm. The experimental results are summarized in Table 3.1. As we can see, in most cases the accuracy of the respiration rate estimation is nearly identical to the simple FFT-based approach. One exception to that trend is Experiment 10. In this particular experiment, the subject was moving in a more pronounced manner, and thus the mean tracking filter provided substantial improvement. The advanced average error was reduced from approximately 9% to roughly 3%, and the error in Experiment 10 was reduced from 24% to 3%.

Table 3.1: Performance of the New Respiration Estimation Approach

EXP	True Respiratory Rate (per min)	Estimated Respiratory Rate
1	10	10.5
2	19	18.8
3	11	10.5
4	15	14.1
5	24	23.4
6	19	18.8
7	20	18.8
8	15	14.1
9	16	15.2
10	10	10.5
11	25	24.8
12	24	24.6
13	22	21.9
14	23	22.8
15	16	16.9

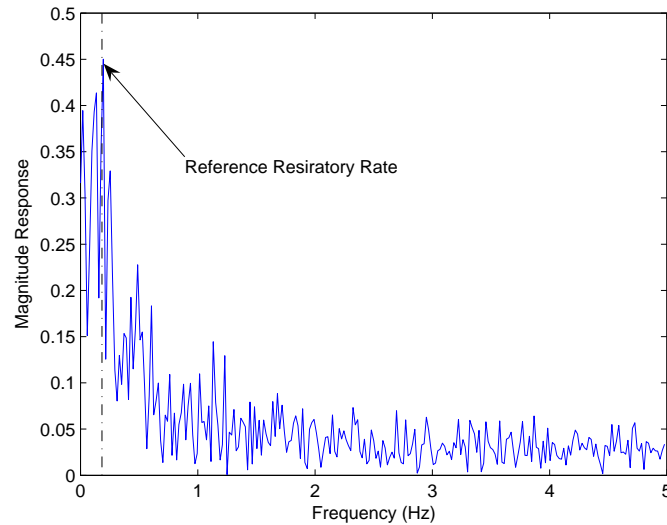


Figure 3.11: FFT of the Slow-time variation along the range bin containing maximum energy from experiment data after compensating drifting mean value

3.4 Conclusions

In this chapter, we identified that large-scale body motion is a major interference for accurate respiration frequency estimation. The motion is manifested as mean position drifting of the observed trajectory in the time domain and exhibits some peaks in the low frequency range. A mean position tracking filter was proposed to estimate the drifting mean position and remove it from the observed trajectory. Instead of the common moving average filter, we apply the ellipse fitting algorithm for the mean estimation due to its robustness and accuracy for the sinusoidal-like trajectory. Experimental results demonstrate that the proposed method effectively avoids false detection due to body motion.

Chapter 4

Improved Single-Target Heartbeat Rate Estimation

4.1 Introduction

As compared to respiration rate estimation, due to the subtle cardiac displacement and the strong interference caused by respiratory harmonics, it is difficult to detect the heart rate accurately from the FFT-based approach directly. This has been demonstrated in our simulation and experimental results discussed in chapter 2. Based on our observations, we identified two major problems which result in high estimation error for heartbeat rate: (1) strong harmonics interference from the respiratory signal. (2) Non-stationarity of signals induced by breathing and heartbeat.

An intuitive way of reducing the respiratory interference and rejecting noise is to use a bandpass filter to eliminate the low frequency respiratory components as done in the FFT-based approach described in Chapter 2. However, this approach is very limited. First,

due to the large variation in human vital signs, it is hard to determine a reliable cut-off frequency to effectively extract the heartbeat spectrum while maximizing noise rejection. Secondly, this approach has little effect on the higher order respiratory harmonics if they happen to lie within the range of the bandpass filter. In this chapter, we will investigate more advanced signal processing algorithms to tackle these problems in order to extract an accurate heartbeat frequency.

4.2 Respiratory Interference Cancellation

FFT-based filter theory has been applied to a wide range of problems and it was our first approach to reject the interference and noise. However, the traditional FFT-based filtering methods in most cases rely on the frequencies obtained in the power spectrum being stationary. The theory of wavelets promises several improvements to the traditional filtering methods. The major difference is the fact that wavelet methods can much better resolve frequencies which vary in time (such as the heartbeat signal and other biomedical signals) [32]. Due to the efficiency of the wavelet transform in extracting both time-like and frequency-like information from a time-varying signal, we adopted a continuous wavelet-based filter to attenuate the harmonics interference from the heartbeat signal.

4.2.1 Wavelet Transform

While a detailed mathematical background of the Continuous Wavelet Transform (CWT) can be found in [2, 33], a brief summary is given as follows. The CWT of a signal $f(t)$ is

defined as

$$Wf(s, b) = \int_{-\infty}^{+\infty} f(t)\psi_{s,b}^*(t)dt \quad (4.1)$$

where

$$\psi_{s,b}(t) = \frac{1}{\sqrt{s}}\psi\left(\frac{t-b}{s}\right) \quad (4.2)$$

is a dilated and shifted version of the mother wavelet also called the wavelet basis $\psi(t)$. $\psi_{s,b}(t)$ is defined on the open (b, s) half plane where $(b \in R, s > 0)$. $\psi^*(t)$ denotes the complex conjugate of $\psi(t)$. The parameter s corresponds to the scale and the parameter b corresponds to the time shift of $\psi(t)$. $\psi(t)$ is in general a complex-valued function, which satisfies the following properties:

$$\int_{-\infty}^{+\infty} |\psi(t)|^2 dt < \infty \quad (4.3)$$

$$C_\Psi = 2\pi \int_{-\infty}^{+\infty} \frac{|\Psi(\omega)|^2}{|\omega|} d\omega < \infty \quad (4.4)$$

where $\Psi(\omega)$ is the Fourier Transform of $\psi(t)$. The first condition implies finite energy of $\psi(t)$, and the second condition, the admissibility condition, implies that if $\Psi(\omega)$ is smooth then $\Psi(0) = 0$.

Since the wavelet transform is essentially a bandpass filter with a known response function (the wavelet function), it is possible to reconstruct the original time series using either deconvolution or the inverse filter. The original signal $f(t)$ can be reconstructed from the CWT coefficients $Wf(s, b)$, by the Inverse Continuous Wavelet Transform (ICWT), which

is defined as

$$f(t) = \frac{1}{C_\Psi} \int_{-\infty}^{+\infty} \int_{-\infty}^{+\infty} Wf(s, b) \frac{\psi_{s,b}(t)}{s^2} ds db \quad (4.5)$$

Therefore, through modifying the wavelet coefficients and reconstructing the signals by summing over scales, one can construct a *wavelet-filtered* time series as desired. In our case, ideally, we would like to find a method that is able to reduce interference and noise through canceling or attenuating the energy of these wavelet coefficients, however, without causing big distortion to the desired signals.

Since we modeled the respiratory and heartbeat signals as sinusoids, we derive the characteristic of the wavelet coefficients of sinusoidal signals. Assuming a sinusoidal wave $f(t) = \alpha e^{j\omega_0 t}$ with the angular frequency ω_0 , the wavelet transform of $f(t)$ can be written as

$$\begin{aligned} Wf(s, b) &= \int_{-\infty}^{+\infty} f(t) \psi_{s,b}^*(t) dt = \underbrace{f(t) * \tilde{\psi}_s(t)}_{\text{Time domain}} \Big|_{t=b} \\ &= \frac{1}{\sqrt{2\pi}} \int_{-\infty}^{+\infty} \underbrace{F(\omega) \cdot \sqrt{s} \Psi^*(s\omega)}_{\text{Frequency domain}} e^{j\omega b} d\omega \\ &= \alpha \sqrt{s} \Psi^*(s\omega_0) e^{j\omega_0 b} \end{aligned} \quad (4.6)$$

where $\tilde{\psi}_s(t) = \frac{1}{\sqrt{s}} \psi^*\left(\frac{-t}{s}\right)$.

From (4.6), we can easily observe that the wavelet coefficients of sinusoidal signals are also sinusoidal with an angular frequency equal to the original frequency ω_0 , and an amplitude equal to $\alpha \sqrt{s} \Psi^*(s\omega_0)$. At a certain wavelet scale s , the amplitude of the wavelet coefficient is determined by the magnitude of $\Psi^*(s\omega_0)$. Assuming multiple sinusoidal signals with different amplitudes and frequencies are contained in the original signal (i.e., $\sum_{i=1}^M \alpha_i e^{j\omega_i t}$), the wavelet

coefficients at scale s can be written as

$$Wf(s, b) = \sum_{i=1}^M \alpha_i \sqrt{s} \Psi^*(s\omega_i) e^{j\omega_i b} \quad (4.7)$$

If we assume the multiple sinusoids have identical amplitudes, the amplitude of the wavelet coefficients should depend on $\Psi^*(s\omega_i)$ due to different angular frequencies ω_i evaluated at the wavelet scale s . On the other hand, for each sinusoid, its wavelet coefficients span along a range of scale s with different amplitudes determined by $\sqrt{s}\Psi^*(s\omega_i)$. If we would like to reject one sinusoid from the original signal, we can attenuate the amplitude of its wavelet coefficients and reconstruct the signals. Now this wavelet-based filter invokes a major problem: How we can utilize the shape $\Psi^*(s\omega_i)$ in order to (1) make the total energy of the wavelet coefficients of each sinusoid concentrate within the scale range as narrowly as possible and (2) at some scale s , if the amplitude of the wavelet coefficient of one sinusoid reaches its maximum amplitude, it is beneficial that the other wavelet coefficients at this scale s are very small (which means the wavelet coefficients contain little information about the original signal) so that we can attenuate the target sinusoid without influencing other sinusoidal signals.

In choosing the wavelet basis function, there are several factors which should be considered [2]:

- *Complex or real.* A complex wavelet function will return information concerning both the amplitude and phase and is better adapted for capturing the oscillatory behavior. A real wavelet function returns only a single component and can be used to isolate peaks or discontinuities.
- *Width.* The resolution of a wavelet function is determined by the balance between the width in real space and in Fourier space. A narrow (in time) function will have good

Table 4.1: Wavelet basis functions

Name	$\psi_0 t$	$\Psi_0(s\omega)$
Morlet (ω_0 =frequency)	$\pi^{-1/4} e^{j\omega_0 t} e^{-t^2/2}$	$\pi^{-1/4} H(\omega) e^{-(s\omega - \omega_0)^2/2}$
Paul (m=order)	$\frac{2^m i^m m!}{\sqrt{\pi(2m)!}} (1 - it)^{-(m+1)}$	$\frac{2^m}{\sqrt{m(2m-1)!}} H(\omega) (s\omega)^m e^{-s\omega}$
DOG (m=derivative)	$\frac{(-1)^{m+1}}{\sqrt{\Gamma(m+\frac{1}{2})}} \frac{d^m}{dt^m} (e^{-t^2/2})$	$\frac{i^m}{\sqrt{\Gamma(m+\frac{1}{2})}} (s\omega)^m e^{-(s\omega)^2/2}$

¹DOG = derivative of a Gaussian;

$H(\omega)$ = Heaviside step function, $H(\omega) = 1$ if $\omega > 0$, $H(\omega) = 0$ otherwise

time resolution but poor frequency resolution, while a broad function will have poor time resolution, yet good frequency resolution.

- *Shape.* The wavelet function should reflect the type of features present in the time series. For a time series with sharp jumps or steps, one should choose a boxcar-like function such as Haar [33], while for smooth functions one should choose a function like a damped cosine.

Table 4.1 provides some typical wavelet basis functions and Figure 4.1 shows four mother wavelet functions based on Table 4.1 in the time domain and frequency domain. The plots on the left give the real part (solid) and imaginary part (dashed) of the wavelets in the time domain. The plots on the right give the corresponding wavelets in the frequency domain. We choose the “Morlet” wavelet due to its complex nature for oscillation detection and narrow bandwidth for good frequency resolution. Additionally, the simple formula of the Morlet wavelet makes it easy to apply the inverse wavelet transform for reconstruction [34].

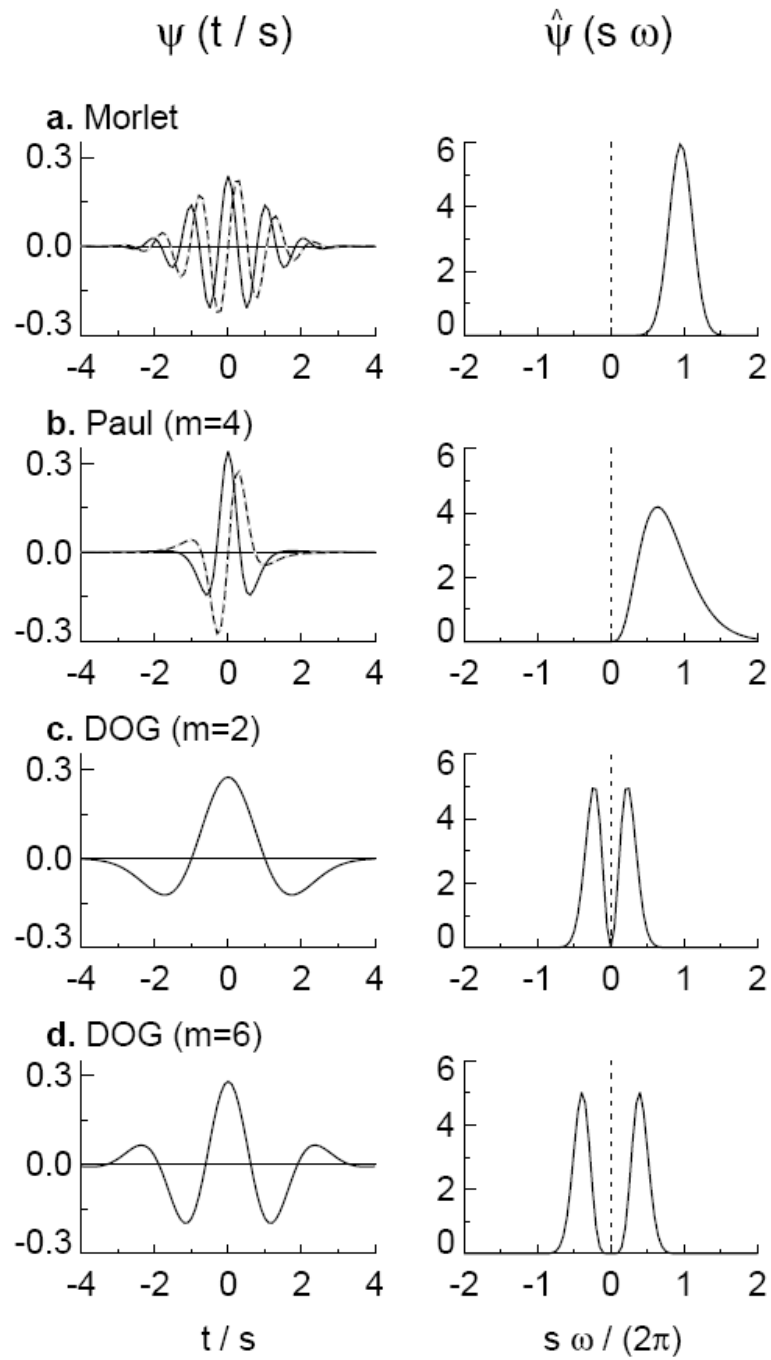


Figure 4.1: Four different wavelet bases (a) Morlet (b) Paul(m=4) (c) Mexican hat(DOG m=2), and (d) DOG (m=6), based on [2]

4.2.2 Shape Factor β for Morlet Wavelet

In Chapter 3 we found that the improved method is able to accurately estimate the respiration frequency, which implies that we can identify the high-order harmonic frequency components of the respiratory signal as well. Based on the estimated respiration rate, we investigate interference cancellation scheme using wavelets.

Examining the shape of $\Psi^*(s\omega)$ of the Morlet wavelet with $\omega_0 = 6$ shown in section 4.2.1, the peak in $\Psi^*(s\omega)$ occurs approximately at the frequency equal to s^{-1} . Actually, we should mention that the equivalent Fourier frequency is not always the reciprocal of the wavelet scale. The relationship between them can be derived analytically for a particular wavelet function. For the Morlet wavelet with $\omega_0 = 6$, $f = 0.9709s^{-1}$, where f is the Fourier frequency, indicating that for the Morlet wavelet the wavelet scale is almost equal to the reciprocal of Fourier frequency. Therefore, at a wavelet scale $s = (\frac{\omega_0}{2\pi})^{-1}$, the frequency-domain function $\Psi^*(s\omega)$ reaches its maximum magnitude at approximately $\omega = \omega_0$, and its magnitude decreases approaching zero with increasing $|\omega - \omega_0|$. This spectral property provides us a way to separate wavelet coefficients of multiple sinusoidal signals.

Based on the discussion above, the concept of interference cancellation using wavelets can be outlined as follows: We first apply the Morlet-based wavelet transform to a mixed signal containing multiple sinusoidal signals. For a sinusoid with angular frequency ω_0 , most of the energy of the wavelet coefficients for this sinusoidal signal will be distributed within a short scale range centered at the scale $s = (\frac{\omega_0}{2\pi})^{-1}$. If the wavelet coefficients of other signals within this scale range only contain little information of the corresponding signals, we can suppress or remove the all wavelet coefficients within this scale range that are thought to be attributed to the sinusoid of interest. After applying the inverse wavelet transform, we can obtain a new reconstructed signal without these sinusoidal components.

In order to concentrate more energy of the interfering signal but keep less energy from the desired signal within a narrow scale range, we introduce the parameter β to control the shape of the standard Morlet wavelet [34], which is defined as

$$\Psi(s\omega) = \pi^{-1/4} H(\omega) e^{-\beta(s\omega - \omega_0)^2/2} \quad (4.8)$$

The parameter β balances the time resolution and the frequency resolution of the Morlet wavelet. Increasing β will increase the frequency resolution, but it decreases the time resolution. When β tends to infinity, the Morlet wavelet becomes a Dirac function which has the finest frequency resolution, and when β tends to 0, the Morlet wavelet becomes all-pass filter which has the finest time resolution. Since we focus on improving the frequency resolution here, we choose $\beta = 5 > 1$ which provides better frequency resolution but also keeps good time resolution.

Since we aim at reducing the respiratory fundamental and its 2nd and 3rd harmonic signals, we calculate the amplitude of the wavelet coefficients of other possible sinusoids whose frequency may be close to them at the scale corresponding to these respiratory frequencies. This allows us to verify the influence on other sinusoids when attenuating these respiratory signals. For ease of comparison, we assume that there are other sinusoids with a frequency of $\Delta_f = 0.1\text{Hz}$ away from the respiratory fundamental, 2nd harmonic and 3rd harmonic frequencies respectively. As shown in Figures 4.2-4.4, when $\beta = 1$, the wavelet coefficients at the scale corresponding to the 3rd respiratory harmonics also contains over 80% information of the adjacent signals. It indicates that removing or suppressing the wavelet coefficient will greatly distort or attenuate the desired signals as well. In contrast to $\beta = 1$, when we change the β value to 5, as shown in Figures 4.5-4.7, the wavelet coefficients at the scale corresponding to the 3rd respiratory harmonics only contain less than half of the information of signals of interest. This guarantees that the heartbeat signal will not be cancelled or

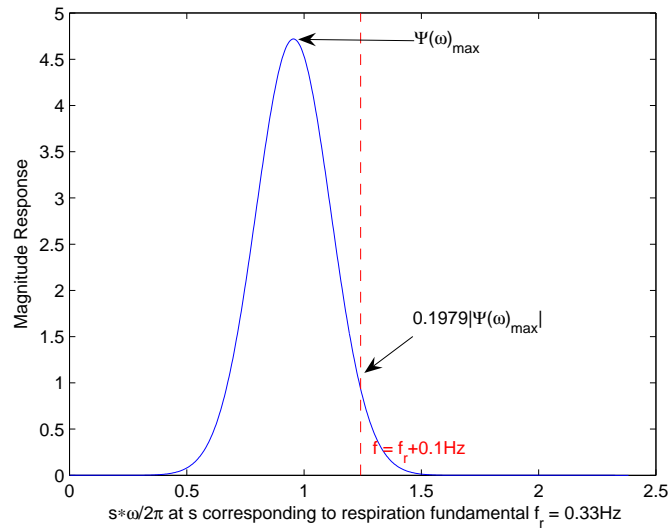


Figure 4.2: Shape of standard Morlet wavelet function in frequency at scale s corresponding to the fundamental respiration frequency, $\beta = 1$

largely distorted when canceling the respiratory interference.

Additionally, we also evaluate the magnitude of $\Psi(s\omega_0)$ along the scale s to verify the width of scale range which each sinusoid will span. Figures 4.8-4.10 illustrate that with a higher β value, the energy of the wavelet coefficients for a sinusoid will be concentrated in a narrower band, which implies that the attenuation of a particular signal's wavelet coefficients will be more effective and cause less distortion of the signal of interest.

4.2.3 Wavelet-based Filter

Using the modified Morlet wavelet mentioned above, we apply the CWT along the scale range equivalent to the frequency from 0.01 to 4Hz which covers the range of all possible vital-signs signals. Based on an accurately estimated respiration rate as discussed in Chapter 3, we can locate the frequency of 2nd and 3rd harmonics of the respiration signal. The procedure for interference cancellation is described as follows:

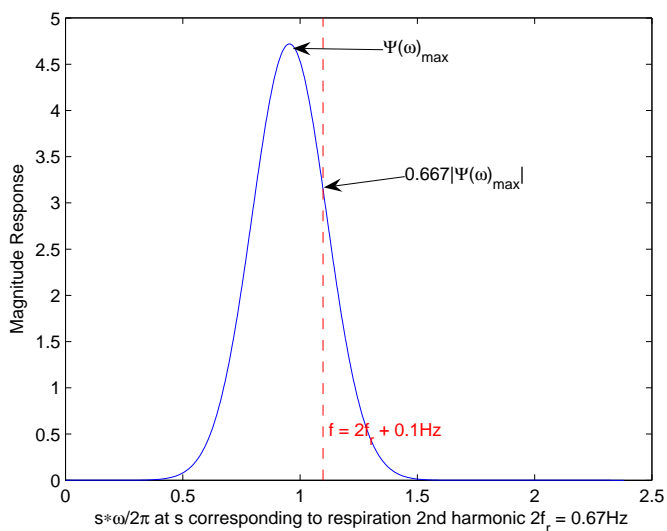


Figure 4.3: Shape of standard Morlet wavelet function in frequency at scale s corresponding to the 2nd harmonic of respiration frequency, $\beta = 1$

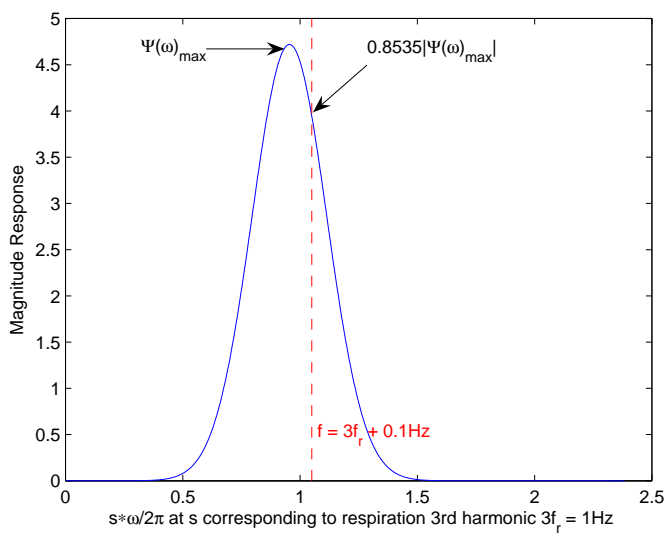


Figure 4.4: Shape of standard Morlet wavelet function in frequency at scale s corresponding to the 3rd harmonic of respiration frequency, $\beta = 1$

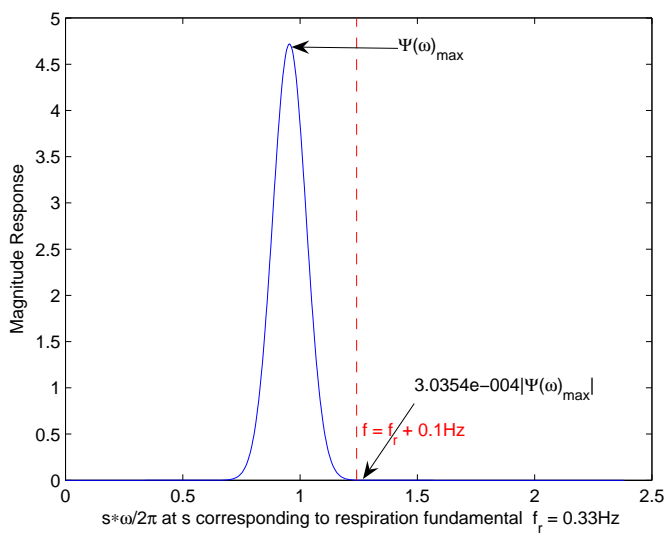


Figure 4.5: Shape of modified Morlet wavelet function in frequency at scale s corresponding to the fundamental respiration frequency, $\beta = 5$

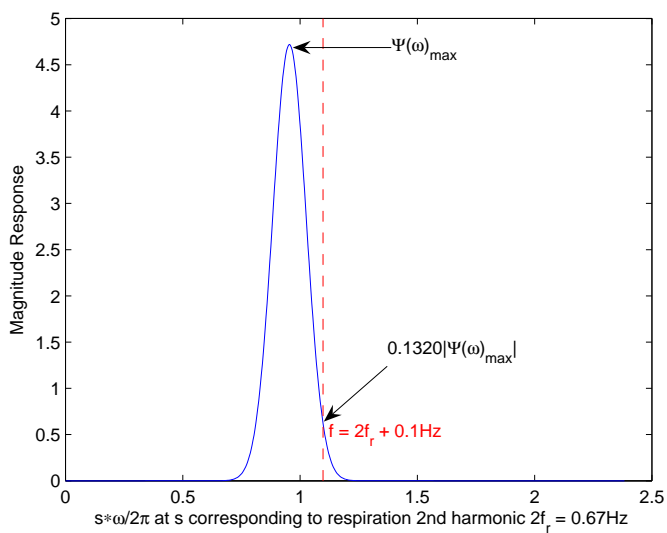


Figure 4.6: Shape of modified Morlet wavelet function in frequency at scale s corresponding to the 2nd harmonic of respiration frequency, $\beta = 5$

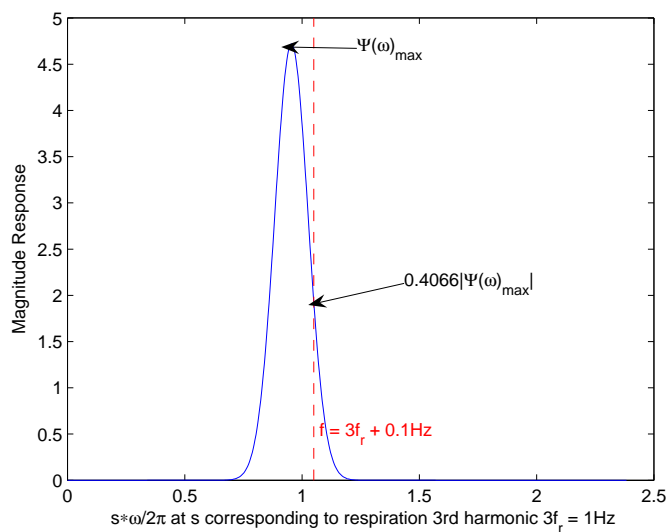


Figure 4.7: Shape of modified Morlet wavelet function in frequency at scale s corresponding to the 3rd harmonic of respiration frequency, $\beta = 5$

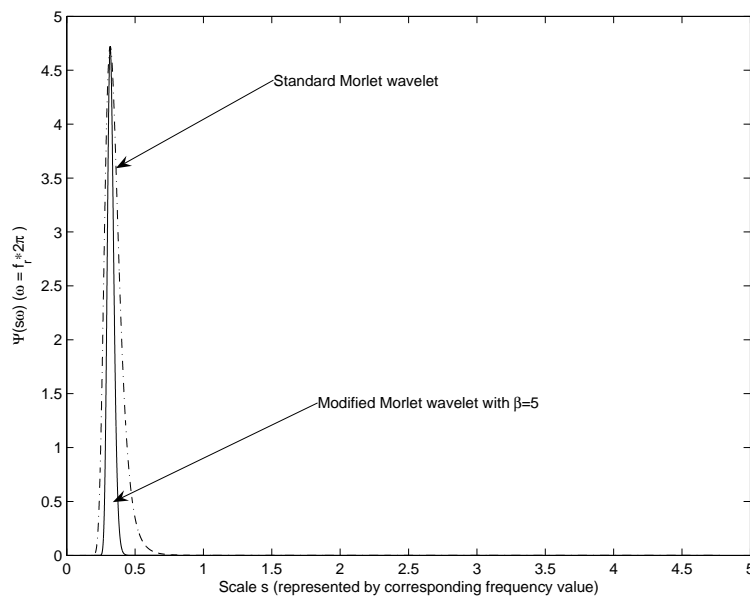


Figure 4.8: Comparison of magnitude of $\Psi(s\omega_0)$ along scale-axis s at the frequency ω_0 corresponding to fundamental respiration rate

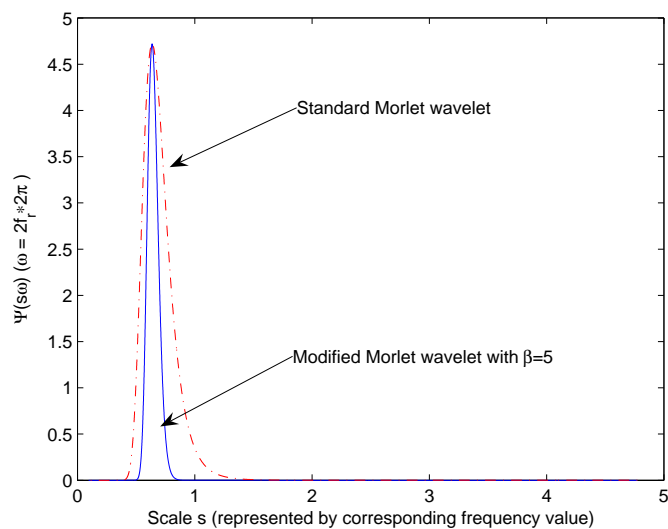


Figure 4.9: Comparison of magnitude of $\Psi(s\omega_0)$ along scale-axis s at the frequency ω_0 corresponding to 2nd harmonic respiration rate

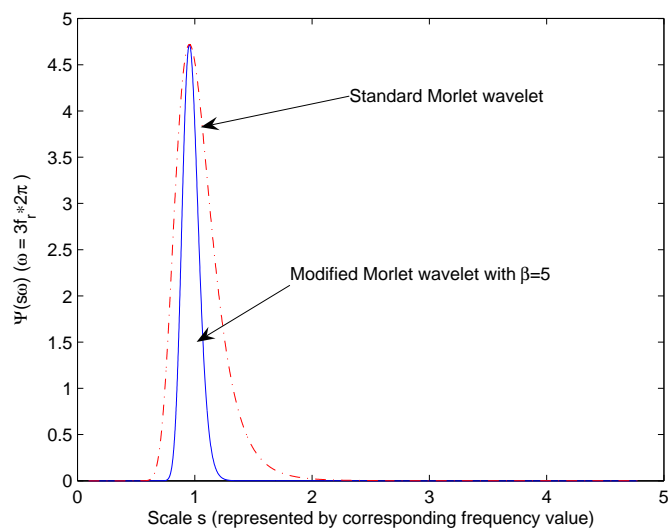


Figure 4.10: Comparison of magnitude of $\Psi(s\omega_0)$ along scale-axis s at the frequency ω_0 corresponding to 3rd harmonic respiration rate

1. *Cancel the respiration fundamental and 2nd harmonic interference.* Since these two components are usually much lower in frequency than the heartbeat frequency, we zero the wavelet coefficients for each scale in the range corresponding to $(0, 2f_r+0.15\text{Hz}]$. Note that the 0.15Hz is for the leakage of the sinusoidal signal wavelet coefficient in the neighboring scales.

$$\begin{aligned}\hat{W}f(s, b) &= 0 \cdot Wf(s, b) \\ 0 &< 0.9709s^{-1} \leq 2f_r + 0.15\end{aligned}\quad (4.9)$$

2. *Attenuate the 3rd harmonic interference.* The 3rd harmonic frequency usually lies within the possible frequency range of the heartbeat frequency. Since the heartbeat frequency is close to the 3rd harmonic of the respiration frequency, it may also impact the amplitude of heartbeat signal if we zero the wavelet coefficients in a narrow frequency range. Instead, we multiply the wavelet coefficients in the scale range corresponding to $[3f_r - 0.1, 3f_r + 0.1]\text{Hz}$ by a parameter $a \in (0, 1)$ so that the interference can be suppressed without canceling the desired heartbeat signals.

$$\begin{aligned}\hat{W}f(s, b) &= a \cdot Wf(s, b) \\ 3f_r - 0.1 &\leq 0.9709s^{-1} \leq 3f_r + 0.1\end{aligned}\quad (4.10)$$

3. *Reconstruct the signal.* Reconstruct the signal by applying ICWT and analyze the spectrum in the frequency domain. Pick the peak with the maximum magnitude in the spectrum as the estimated heartbeat rate.

$$f(t) = \frac{1}{C_\Psi} \int_{0.9709s^{-1}=2f_r+0.15}^{0.9709s^{-1}=4} \int_{-\infty}^{+\infty} \hat{W}f(s, b) \frac{\psi_{s,b}(t)}{s^2} dsdb \quad (4.11)$$

Note that the parameter a and the scale range determined here are obtained based on real experiments. As to different wavelet models or different measurement setups, the parameters may need to be adjusted.

4.3 Simulation Results

Simulation results using this wavelet-based filter are shown below. The model is the same as we developed in Chapter 2. The maximum deviation of the chest wall movement due to respiration Δ_r was assumed to be 10mm, and Δ_h associated with cardiac muscle expansion-contraction movement was assumed to be 1mm. As an example, Figure 4.11 shows the original spectrum of the observed trajectory, assuming that the respiration rate is 20 breaths/min (0.33Hz) and the heartbeat rate is 70 beats/min (1.16Hz). We also assume that the heartbeat signal is 20dB lower than respiratory signal. Examining Figure 4.12, we find that the normal bandpass filter with a passband frequency range of [0.7 4]Hz fails to eliminate the interference from the 3rd harmonics of the respiration signal. Further, the magnitude of the 3rd harmonic is larger than the heartbeat in the frequency domain which will cause false detection of the heartbeat frequency. However, after using the wavelet-based filter, the heartbeat frequency is magnified as compared to the attenuated interference peak, and there is almost no energy loss for the heartbeat signal, as shown in Figure 4.13.

The average error magnitude of heartbeat rate estimation (in beats per minute) versus Signal-to-Noise Ratio (SNR) based on simulation is shown in Figure 4.14. In this simulation, the heartbeat movement was assumed to be stationary and 20dB weaker than the respiratory signal. The respiration rate was random over 2000 simulations and uniformly distributed between 12 and 25 breaths per minute (0.2-0.4Hz). The heartbeat rate was uniformly distributed from 60 to 100 beats per minutes (1-2Hz). The average error is plotted versus the

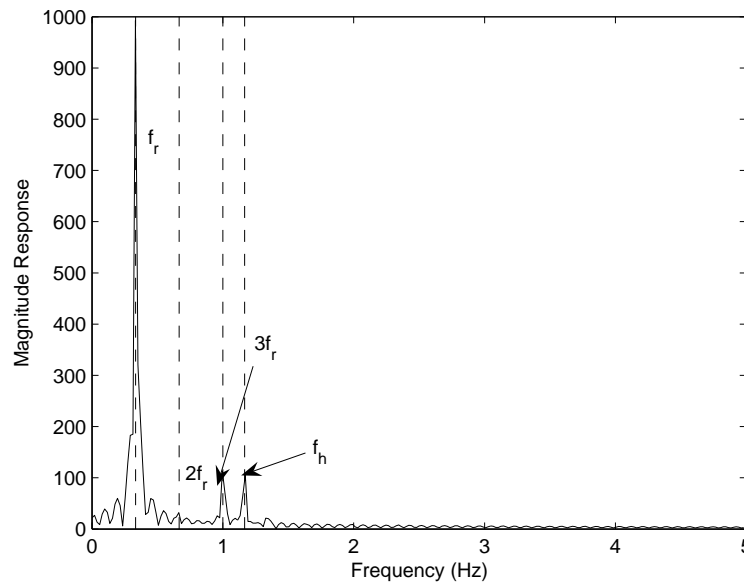


Figure 4.11: Original spectrum of the observed trajectory at $f_r = 0.33Hz$ and $f_h = 1.16Hz$

average SNR of the received signal. We compared the performance between the FFT-based approach and the improved algorithm discussed in this chapter. It is obvious that the simulation result provided by the improved method has much lower error floor which is mainly caused by the finite resolution in the frequency analysis.

The simulation results indicate that the improved algorithm successfully avoids the false detection of respiratory harmonics, thus improves the accuracy of heartbeat detection.

Finally, in order to verify the resolution of the proposed filter, we simulated with an assumed respiration rate of 20 breath/min (0.33Hz), and a heartbeat rate as 65 beats/min (1.08Hz). In this case, the 3rd harmonics of respiration signals is 1Hz and very close to the heartbeat frequency. In Figure 4.15, the magnitude of the 3rd respiratory harmonic is at the same level as the desired heartbeat frequency peak and thus it will be very difficult to correctly detect the heartbeat frequency. After applying the wavelet-based filter as shown in Figure 4.16, we find that although the heartbeat frequency is very close to the 3rd respiratory harmonic,

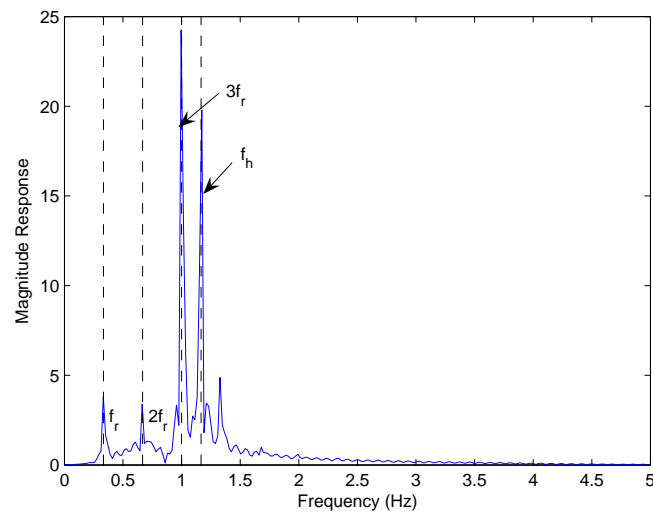


Figure 4.12: Spectrum of the observed trajectory after apply a bandpass filter with passband of $[0.7 \ 4]$ Hz at $f_r = 0.33Hz$ and $f_h = 1.16Hz$

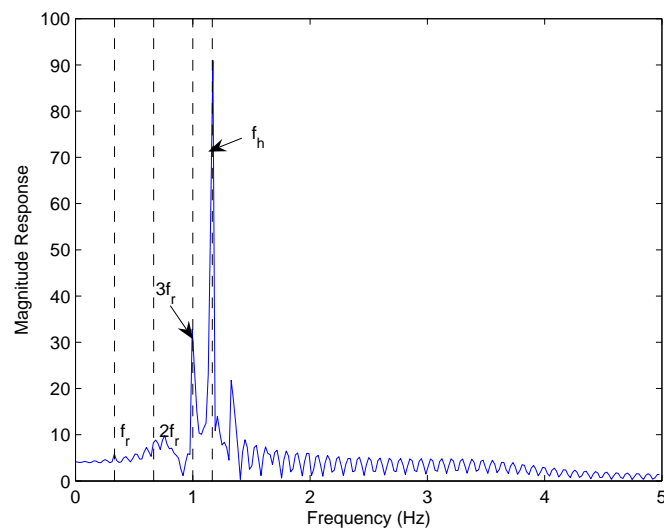


Figure 4.13: Spectrum of the observed trajectory after proposed filtering at $f_r = 0.33Hz$ and $f_h = 1.16Hz$

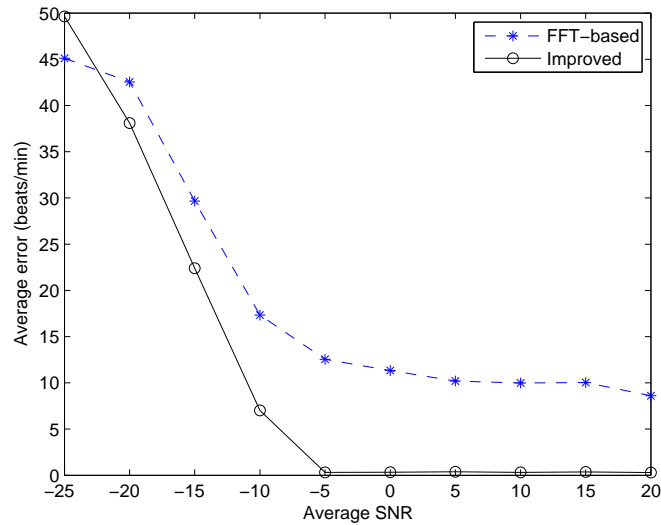


Figure 4.14: Average error of heartbeat rate estimation from simulation

and both of their magnitudes have been attenuated, the desired heartbeat frequency peak is now much larger than the 3rd respiratory harmonic. The results indicate that the proposed method could still provide reliable performance even with approximately 0.1Hz frequency difference between the desired signal and the 3rd respiratory harmonic.

4.4 Frequency Estimation for Non stationary Signals

Up until this point, the FFT has been used for spectral analysis. However, it can be shown that due to the non-stationary nature of many bio-medical signals (e.g., respiratory and cardiac signals), the FFT had limited applicability. A common approach to examining the spectra of non-stationary signals is the Welch periodogram [35].

As introduced in section 1.2, the detection of respiration and heartbeat rates can be modeled as the detection and frequency estimation of multiple non-stationary sinusoidal signals from a finite number of noisy discrete-time measurements.

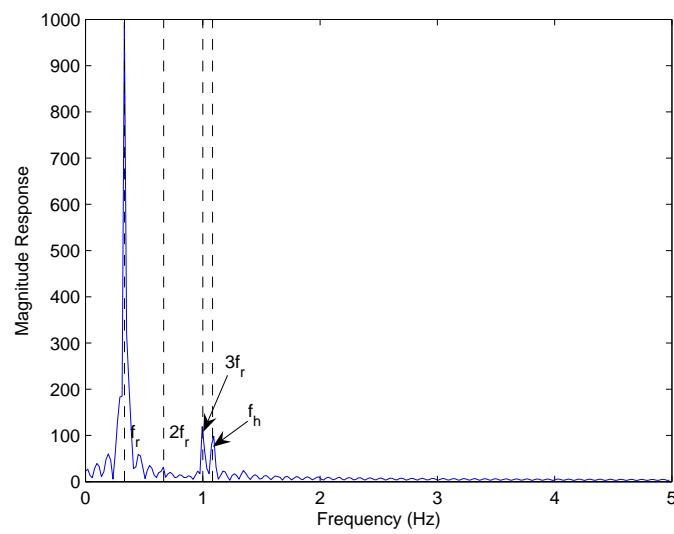


Figure 4.15: Original spectrum of the observed trajectory at $f_r = 0.33Hz$ and $f_h = 1.08Hz$

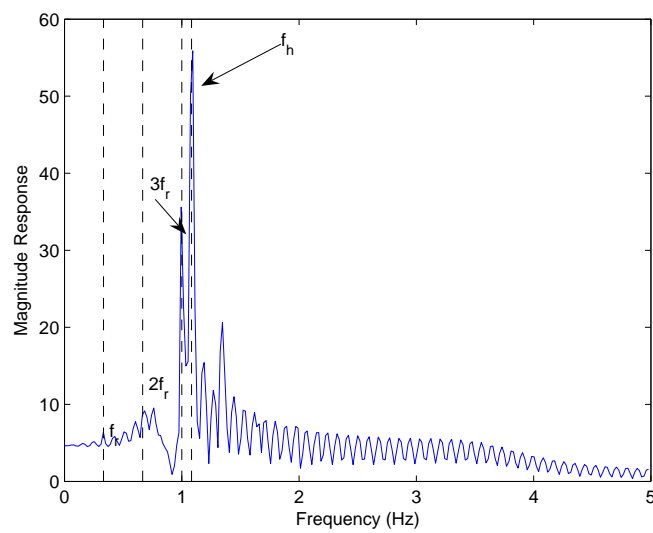


Figure 4.16: Spectrum of the observed trajectory after proposed filtering at $f_r = 0.33Hz$ and $f_h = 1.08Hz$

A direct method for tone detection and frequency estimation is the standard periodogram [36] based on the Discrete Time Fourier Transform (DTFT). The periodogram of an N -point input sequence, $x(0), x(1), \dots, x(N-1)$, is defined as

$$P_{per}(f) = \frac{1}{N} \left| \sum_{n=0}^{N-1} x(n) \exp(-j2\pi n f) \right|^2 \quad (4.12)$$

$$(4.13)$$

Thus, the periodogram is proportional to the squared magnitude of the DTFT of the observed data. In practice, sampling the periodogram at $f_k = k/N$, $k = 0, 1, \dots, N-1$ can be computed efficiently with the use of the Fast Fourier Transform (FFT) algorithm while values at the other frequencies are evaluated by either zero padding or interpolation. If $\tilde{x}[n]$ is real zero-mean white Gaussian noise with variance σ^2 , the variance of $P_{per}(f)$ is equal to σ^4 regardless of the length N of the observed data samples. So the standard periodogram is not a good estimator since the performance of the periodogram does not improve as N get larger. The variance problem can be reduced by smoothing the periodogram, such as with *Bartlett's* and *Welch's* periodogram [37].

In the Bartlett method, the sequence $x(n)$ is divided into K non-overlapping segments, where each segment has length M . For each segment, the periodogram is computed and the Bartlett power spectral estimate is obtained by averaging the periodograms for the K segments. By doing so, the variance in the periodogram estimate is reduced by a factor K but at the expense of reducing the frequency resolution by K . The Bartlett estimator has a resolution K times less than that of the standard periodogram.

Welch [35] modified Bartlett's procedure by allowing the data segments to overlap, where the overlaps are usually 50% or 75%, and data within a segment are windowed. Let the length of the segment be L , the i -th segment be denoted again by $x_i[n]_0^{L-1}$, and the offset of

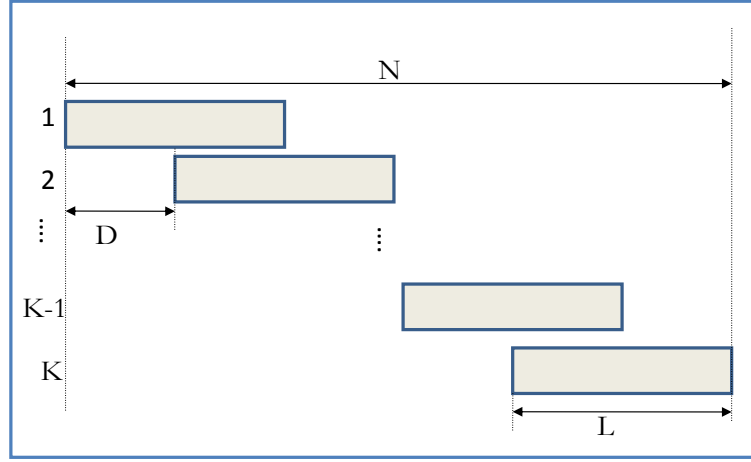


Figure 4.17: Illustration of the data segments of input sequence

successive segments by D samples, as shown in Figure 4.17. Then

$$N = L + D(K - 1) \quad (4.14)$$

where N is the total number of observed samples, K is the total number of segments and D implies the non-overlapping length for each segment. Note that if there is no overlap, $K = N/L$, and if there is 50% overlap, $K = 2N/L - 1$. The i -th sequence is defined by

$$x_i[n] = x[n + (i - 1)D] \quad (4.15)$$

$$n = 0, 1, \dots, L - 1$$

$$i = 0, 1, \dots, K$$

and its periodogram by

$$P_M^{(i)}(f) = \frac{1}{L} \left| \sum_{n=0}^{L-1} \omega[n] x_i[n] e^{-j2\pi f n} \right|^2 \quad (4.16)$$

Here $P_M^{(i)}(f)$ is the i th modified periodogram of the data since the samples $x_i[n]$ are weighted by a non-rectangular window $\omega[n]$. In our implementation, we choose ‘‘Hanning’’ window. The Welch spectrum estimate is then given by

$$P_{welch}(f) = \frac{1}{K} \sum_{i=1}^K P_M^{(i)}(f) \quad (4.17)$$

By permitting the overlap of sequences, we can form more segments than in the case of Bartlett’s method. Also, if we keep the same number of segments, the overlap allows for longer segments. The increased number of segments reduces the periodogram variance, and the longer segments improve its resolution, while the windowing is applied to reduce the spectral leakage associated with finite observation intervals. Thus, with the Welch method we can trade reduction in variance for improvement in resolution in many more ways than with the Bartlett method. It can be shown that if the overlap is 50%, the variance of the Welch estimator is approximately 9/16 of the variance of the Bartlett estimator [37]. Therefore, Welch’s method is often desired for noise reduction caused by imperfect and finite data. Additionally, In reference [38], a comparison of various periodograms for detection of a sinusoidal and frequency estimation has shown that the Welch method is the best detector when there is phase instability in the sinusoid.

Due to the phase instability nature of the vital signs signal, Welch averaged periodogram [35] avoids the necessity of interpolating noisy or abnormal beat detection, thus avoiding spectrum distortion. Therefore, we choose to apply the Welch periodogram to get the heartbeat frequency estimate instead of the simple FFT after wavelet-based filtering. Figure 4.18 shows the FFT spectrum and Welch periodogram spectrum of the same observed trajectory. The spectrum of Welch periodogram is obviously much smoother than FFT spectrum. It indicates that the Welch periodogram effectively mitigates the impact of abnormally sharp transient or noise but retains good resolution on the local maximum frequency information.

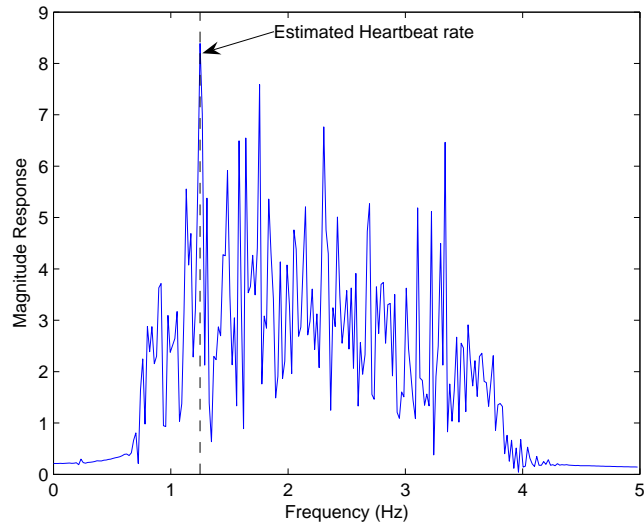
It holds great potential to avoid false detection of magnitude peaks caused by non-stationary noise. Therefore, we apply the Welch periodogram as the spectrum estimator for more reliable performance.

4.5 Experimental Results

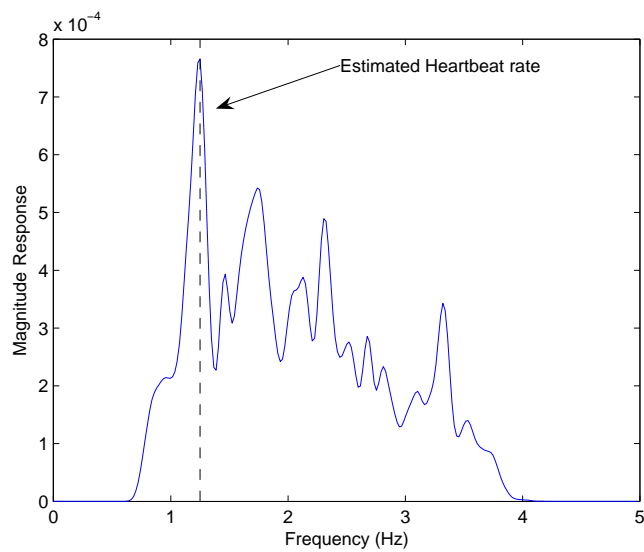
The most pronounced difference between the FFT-based approach and the proposed method (including both wavelet filtering and use of the Welch periodogram) is seen in the heart rate estimation. While the FFT-based approach often provided very large errors (e.g., Experiments 6,7 and 9), the error of the proposed technique was no greater than 4%. This is due primarily to the suppression of the breathing rate signal and noise, but also can be attributed to the use of the Welch periodogram as opposed to the FFT for spectral analysis. Figure 4.19 and 4.20 illustrate the spectra for respiration rate and heartbeat rate detection respectively. The estimated heart rates for each of the 10 experiments are given in Table 4.2.

4.6 Conclusions

Based on both simulation and experimental results from the FFT-based approach, we identified two major problems for heartbeat rate estimation: (1) respiratory harmonics resulting in false detection and (2) the non-stationary nature of heartbeat signal cause difficulty of frequency estimation. A wavelet-based filter was developed to mitigate the interference of respiratory signals and the Welch periodogram was shown to be give more reliable performance for spectral analysis of non-stationary signals. The experiment results demonstrates substantial improvement in accurate heartbeat estimation by the proposed algorithm.



(a) FFT of the observed trajectory



(b) Welch periodogram of the observed trajectory before wavelet-filtering

Figure 4.18: Performance of FFT spectrum and Welch periodogram of the observed trajectory

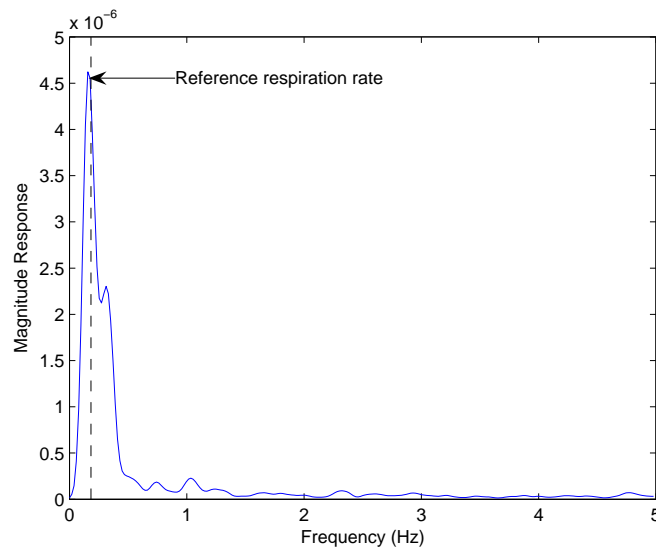


Figure 4.19: Spectrum of the observed trajectory for respiration rate detection

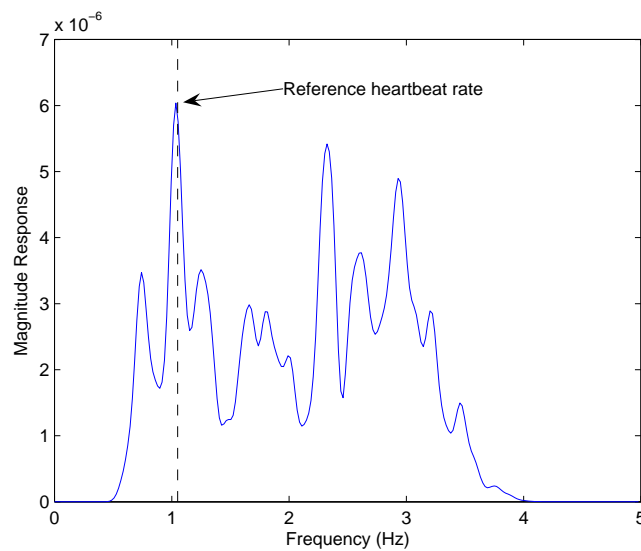


Figure 4.20: Spectrum of the observed trajectory for heartbeat rate detection

Table 4.2: Performance of the New Heartbeat Estimation Approach

EXP	True Heartbeat Rate (per min)	Estimated Heartbeat Rate
1	63	62.1
2	71	69.0
3	78	77.3
4	71	71.5
5	90	91.4
6	103	107.8
7	115	116.0
8	74	75.0
9	110	111.3
10	68	69.1
11	64	66.4
12	80	80.5
13	60	62.1
14	70	66.8
15	60	61.9

Chapter 5

Multi-Target Vital-Signs Estimation

5.1 Introduction

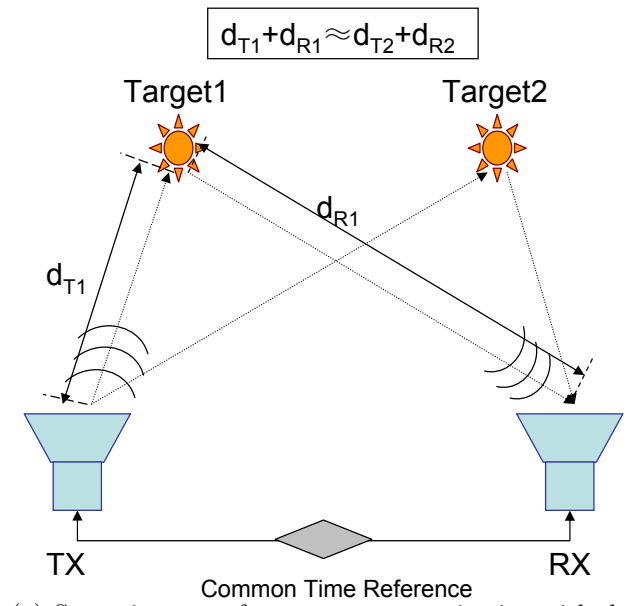
Previous chapters have demonstrated that the proposed UWB radar system is capable of accurately estimating the respiration and heartbeat of a single target. As mentioned in Chapter 1, it is possible to apply this contact-free monitoring technique to vital-signs detection in the presence of multiple targets. This potentially reduces the cost of health care by reducing the number of medical devices being used per patient. Additionally it could be applied to emergency rescue situations, especially in the case of triage when several victims are trapped under debris. This technology can help to estimate the number of people and help ascertain their physical conditions. With the precise location ability of a UWB system, it can also determine the location of the victims at the same time. In this chapter, we will investigate signal processing techniques for respiration and heartbeat rate estimation for multiple targets, based on the same measurement setup and system used for single-target detection discussed in Chapters 2-4.

5.2 Multi-Target Respiration Rate Estimation

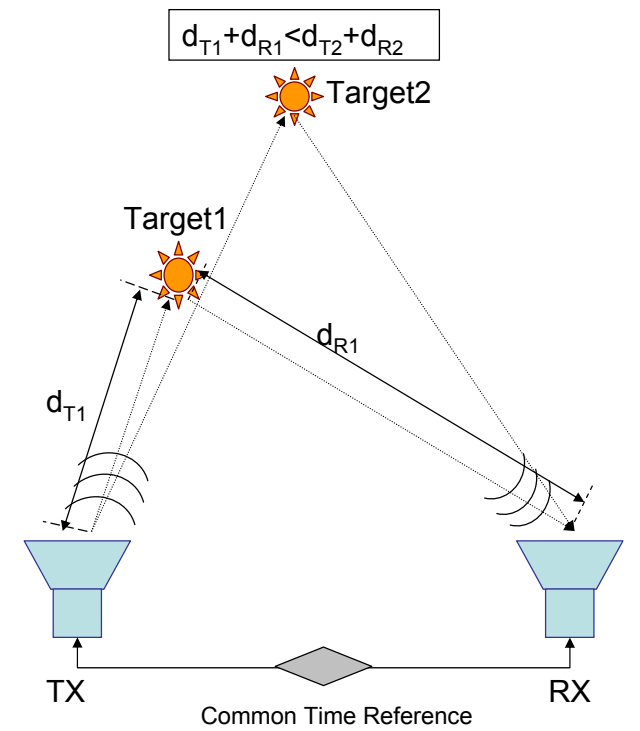
First, we focus on the estimation of the respiration rates of multiple targets. The analysis is based on a known number of targets being monitored. Two potential scenarios for two-person monitoring are shown in Figure 5.1. Based on the positions of the two targets, from the view of the receiver, potential scenarios can be classified into two classes. Figure 5.1(a) illustrates the first case where the round-trip distances between the transmitter and the receiver, reflected by the two targets are approximately the same. In this case the echo pulses from the different targets arriving at the receiver will overlap with each other in time. In this case, after removing the “stationary background”, the single observed trajectory selected by the maximum energy contained *fast-time* bin may contain most of the energy from the two periodic signals. A second situation shown in Figure 5.1(b) represents the case where due to the large difference in the traveled distance of the echo pulses, the two received pulses are not overlapped in time or are only partially overlapped. If we apply the same technique that we did in first case, the single observed trajectory may only contain the information from one target, therefore we will miss the detection of the other target. In order to collect the complete information of all the periodic signals, we adopt techniques from array processing which has similar structure as our model.

5.2.1 Array processing for respiration estimation

Recalling the notation of the observed trajectory, a *fast-time* bin containing the *slow-time* variation (\mathbf{r}_n in (2.9)) can be regarded as a vector of sensors in an array. Instead of determining one sensor by picking the *fast-time* bin which contains maximum energy, we set a threshold of energy to select several bins which may contain information about the signals of interest and thus construct virtual array of sensors. The original single-target model has



(a) Scenario setups for two person monitoring with the same round-trip distance from transmitter to receiver



(b) Scenario setup for two person monitoring with different round-trip distances from transmitter to receiver

Figure 5.1: Scenario setup for two person monitoring

been modified to detect multiple sinusoidal signals from measurements collected by an array of sensors. Subspace-based approaches are common methods for spectrum analysis applied to array processing. Generally speaking, they generate a power spectral density based on eigen-analysis or eigen-decomposition of the correlation matrix from the array of received signals. These methods are best suited for spectra of sinusoidal signals and are effective for detecting sinusoids buried in noise, especially when the signal-to-noise ratios are low [37].

We apply Multiple Signal Classification (MUSIC) using Schmidt's eigenspace analysis method [39] which is regarded as a subspace method with good performance compared to other subspace methods, and particularly suitable for signals that are the sum of sinusoids with additive white Gaussian noise [40], [37], [41]. The complete analysis of the MUSIC algorithm can be found in [39]. We outline the algorithm briefly as follows.

Consider an array of M sensors receiving a set of waves emitted by D sources. The received length- M vector \mathbf{X} can be written as

$$\begin{bmatrix} x_1 \\ x_2 \\ \vdots \\ x_M \end{bmatrix} = \begin{bmatrix} a(\theta_1) & a(\theta_2) & \cdots & a(\theta_D) \end{bmatrix} \begin{bmatrix} f_1 \\ f_2 \\ \vdots \\ f_D \end{bmatrix} + \begin{bmatrix} n_1 \\ n_2 \\ \vdots \\ n_M \end{bmatrix} \quad (5.1)$$

or

$$\mathbf{X} = \mathbf{A}\mathbf{F} + \mathbf{N} \quad (5.2)$$

where $\mathbf{F} = [f_1, \dots, f_D]^T$ is the length- D vector of sources; $\mathbf{A} = [a(\theta_1), \dots, a(\theta_D)]$ is the $M \times D$ matrix in which $a(\theta_i)$ is the response of the array to the i th source arriving from θ_i ; and $\mathbf{N} = [n_1, \dots, n_M]^T$ is an additive noise process.

The $M \times M$ covariance matrix of the \mathbf{X} vector is

$$\begin{aligned} \mathbf{S} &= E[\mathbf{X}\mathbf{X}^*] = E[\mathbf{A}\mathbf{F}\mathbf{F}^*\mathbf{A}^* + \mathbf{N}\mathbf{N}^*] \\ &= \mathbf{A}\mathbf{R}\mathbf{A}^* + E[\mathbf{N}\mathbf{N}^*] \end{aligned} \quad (5.3)$$

where $\mathbf{R} = E\mathbf{F}\mathbf{F}^*$. Assuming the noise is spatially white, we can rewrite $E[\mathbf{N}\mathbf{N}^*]$ as $\sigma^2\mathbf{I}$

When the number of source signals D is less than the number of array elements M , then $\mathbf{A}\mathbf{R}\mathbf{A}^*$ is singular, i.e., it has a rank less than M . Therefore

$$|\mathbf{A}\mathbf{R}\mathbf{A}^*| = |\mathbf{S} - \sigma^2\mathbf{I}| = 0 \quad (5.4)$$

If the source signals are independent or partially correlated, $rank(\mathbf{R}) = D$, and \mathbf{A} are also full rank which is generally true. These imply that $rank(\mathbf{S})$ is D , therefore, \mathbf{S} must have D non-zero eigenvalues and $M - D$ zero eigenvalues. Let the eigen decomposition of S be

$$\mathbf{S} = \sum_{i=1}^M \alpha_i \mathbf{v}_i \mathbf{v}_i^* \quad (5.5)$$

where $\alpha_1 \geq \alpha_2 \geq \alpha_{D+1} = \alpha_M = 0$ are the rank-ordered eigenvalues, and $\{\mathbf{v}_i\}_{i=1}^M$ are the corresponding eigenvectors. The eigenvectors can be partitioned into two sets,

$$\mathbf{E}_s = [\mathbf{v}_1, \dots, \mathbf{v}_D] \quad (5.6)$$

forms the *signal subspace*, and

$$\mathbf{E}_n = [\mathbf{v}_{D+1}, \dots, \mathbf{v}_M] \quad (5.7)$$

forms the *noise subspace*.

From the orthogonality of the signal and noise subspaces, we can detect the signal by finding the peaks in the estimator function

$$\mathbf{P}_{MUSIC}(\theta) = \frac{1}{a^*(\theta)\mathbf{E}_n\mathbf{E}_n^*a(\theta)} \quad (5.8)$$

where \mathbf{P}_{MUSIC} is the ordinary Euclidean distance (squared) from a vector to the noise subspace. Substituting $a(\theta)$ with $e(f)$ which consists of a complex exponential which is defined as

$$e(f) = e^{-j2\pi f} \quad (5.9)$$

we rewrite (5.8) as

$$\begin{aligned} \mathbf{P}_{MUSIC}(f) &= \frac{1}{e^*(f)\mathbf{E}_n\mathbf{E}_n^*e(f)} \\ &= \frac{1}{e^*(f)\left(\sum_{i=D+1}^M \mathbf{v}_i\mathbf{v}_i^*\right)e(f)} \end{aligned} \quad (5.10)$$

$$= \frac{1}{\sum_{i=D+1}^M |\mathbf{v}_i^*e(f)|^2} \quad (5.11)$$

$$(5.12)$$

so the inner product $\mathbf{v}_i^*e(f)$ amounts to a Fourier transform. The estimator can be regarded as the computation of the pseudospectrum. The frequencies which yield strong peaks correspond to the frequencies of the source signals. Note that the MUSIC algorithm assumes that the number of source sinusoidal signals is known.

In our case, the array of received signals consists of multiple observed trajectories which contain energy above the threshold. Now we summarize the procedure for detecting multi-target respiration rates as follows:

1. Apply a motion filter: Eliminate static background.
2. Obtain the array of the observed trajectory: Calculate the energy contained at each *fast-time* bins and maintain those bins whose energy is above a specified threshold.
3. Mean position tracking: Compensate the drifting mean value for each observed trajectory to avoid false detection.
4. Apply bandpass filter: Apply a low pass filter with the cut-off frequency of 0.5Hz to reduce the influence of the harmonics of the respiration signals.
5. Determine the MUSIC spectrum: Find the peaks corresponding to the estimated respiration rates.

5.2.2 Simulation Results

We simulated a two-target scenario to verify this method. We assume that the strength of the respiratory signal of Target1 is 5dB higher than Target2, and the difference of their echo pulses traveled distance is 0.2meters with the pulse width of 1nanoseconds. From the MUSIC spectrum as shown in Figure 5.2, two frequency peaks are clearly discernible with accurate estimation.

In the above simulation, we assumed that the received two echo pulses are about similar in amplitude. However, if one is much larger than the other, we may get two peaks at the true respiration frequency and the 2nd harmonic of the respiration frequency, as shown in Figure 5.3. In order to avoid such false detection, a low-pass filter at passband of $[0, 0.5]Hz$ should be applied before applying the MUSIC algorithm. This will eliminate most harmonics.

The average error magnitude of two-target respiration rate estimation(in breaths per minute) versus Signal-to-Noise Ratio (SNR) based on simulation is shown in Figure 4.14. In this sim-

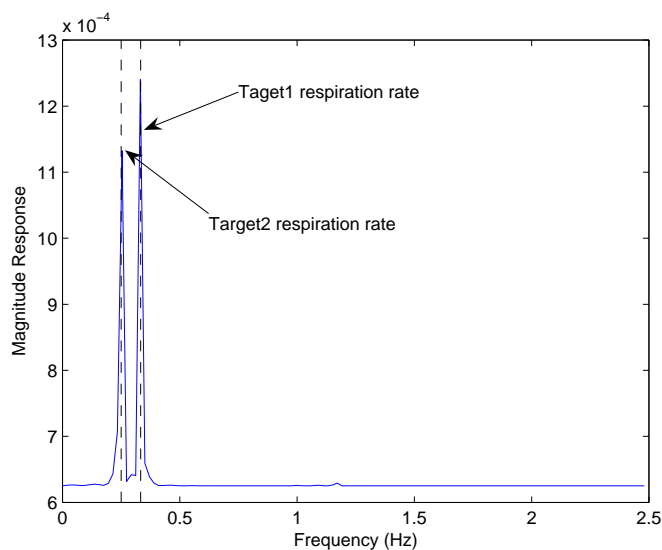


Figure 5.2: Spectrum of the array of the observed trajectory by using MUSIC algorithm, assuming Target1's respiration rate is 20 breaths/min (0.33Hz), Target2's respiration rate is 15 breaths/min (0.25Hz)

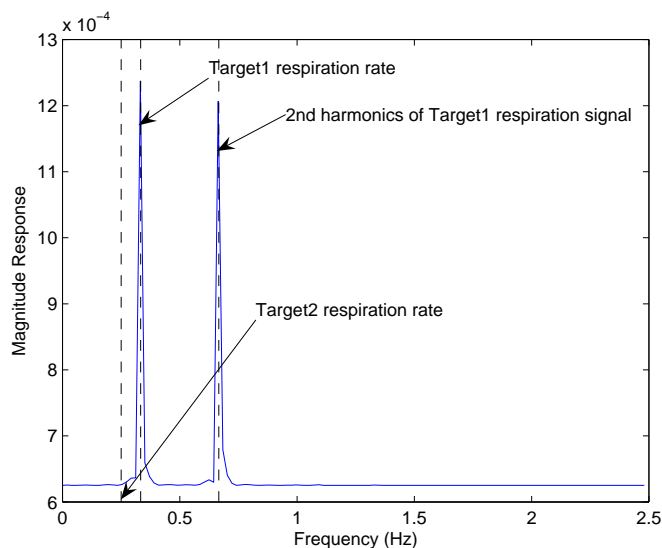


Figure 5.3: Spectrum of the array of the observed trajectory by using MUSIC algorithm, assuming Target1's respiration rate is 20 breaths/min (0.33Hz), Target2's respiration rate is 15 breaths/min (0.25Hz); Target1's receiving pulse amplitude is twice as the Target2's

ulation, the respiration rates were random over 2000 simulations and uniformly distributed between 12 and 25 breaths per minute (0.2-0.4Hz). The target1's signal is 2dB stronger than target2 and the difference of their relative distance to the transmitter and receiver is 0.5meters. The average error is plotted versus the average SNR of the received signal. We noticed that the error floor is higher than the single-target respiration rate estimation.

Figure 5.5 illustrates the distribution of the error of multi-target respiration rate estimation at SNR= 20dB over 200 simulations. We found that a big cluster is close to zero which indicates the successful detection of multi-target respiration frequency. There is also smaller clusters around the error of 15% and even up to 50%. After examining these estimated frequencies, we found out that the degraded performance is due to the two close respiration rates with additive noise which reduce the resolution of MUSIC spectrum analysis. As an extreme example, when two target have the same respiration frequency, the MUSIC algorithm will generate a single peak at that frequency and another spurious peak which can be regarded as a false detection and cause a large estimation error.

5.2.3 Experimental Results

We conducted a three-target scenario and a two-target scenario with the measurement setup described in Chapter 2. The scenario setup is illustrated in Figures 5.6(a) and 5.6(b), and the relative position of each target is labeled in the figures. We take experiment 1 as an example which has three targets. From the frequency estimation based on MUSIC algorithm, we can clearly distinguish the presence of multiple peaks as shown in Figure 5.7. The results are presented in Table 5.1. The average error is approximately 8% with a maximum error of 9.3%. Compared to the average error of single target respiration rate estimation shown in Chapter 3, which is approximately 2%, we find that the accuracy of multi-target respiration

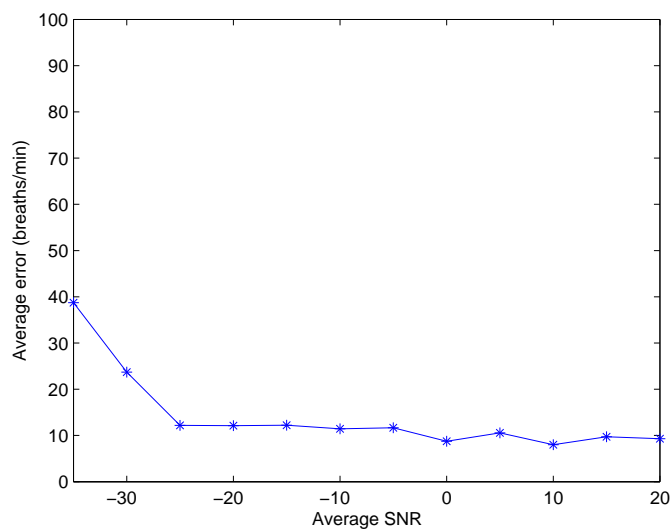


Figure 5.4: Average error of two-target respiration rate estimation from simulation using MUSIC algorithm

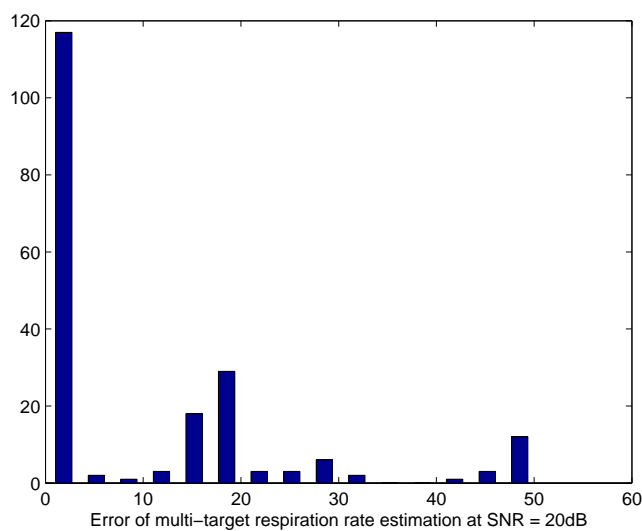


Figure 5.5: Distribution of estimation error of the multi-target respiration rate at SNR=20dB

Table 5.1: Reference and Estimated Respiration Rate

EXP	Target	True Respiratory Rate (per min)	Estimated Respiratory Rate(per min)
1	1	15	16.4
	2	20	18.16
	3	26	24.61
2	1	19.5	17.57
	2	20.5	19.92

rate estimation is obviously degraded. The possible reasons for the relatively high error rate are close respiration rates of the different targets and as well as the influence of additional noise.

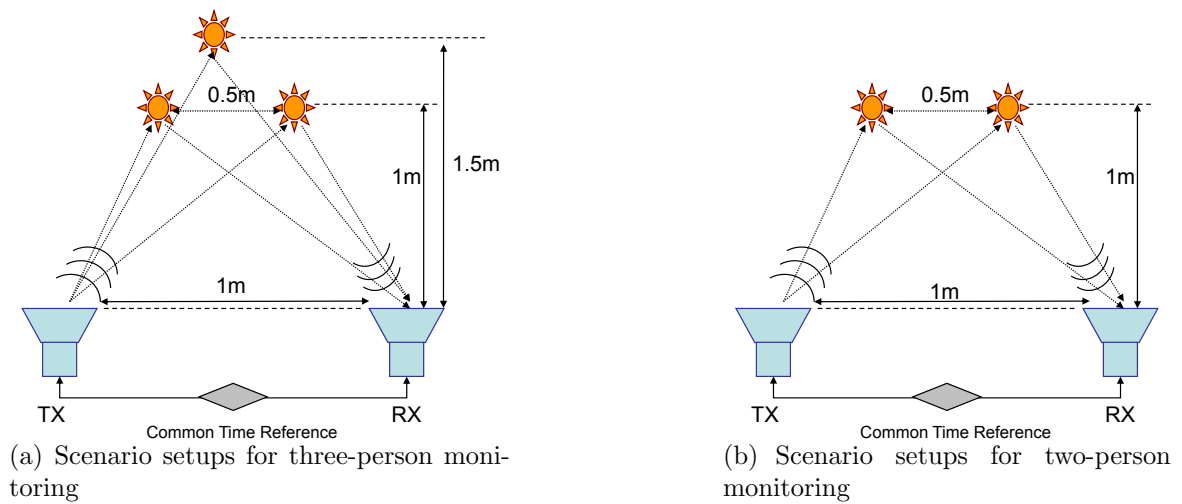


Figure 5.6: Scenario setup for multi-target monitoring

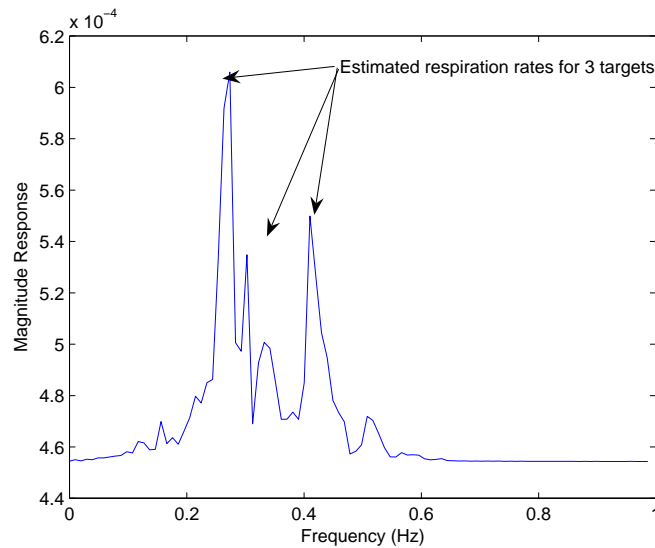


Figure 5.7: Respiration rate detection in three-target scenario

5.3 Multi-target Heartbeat Rate Estimation

Due to the weak amplitude of the received heartbeat signals and the strong interference of the respiratory harmonic signals, it is almost impossible to detect the heartbeat rate directly with the MUSIC algorithm from the covariance of the array of the observed trajectory. We need to combine the techniques for the single observed trajectory with the array processing.

5.3.1 Combination of single-target and multi-target techniques

In Section 5.2, we showed that the respiration rates of multiple targets can be accurately estimated. Based on each estimated respiration rate, we try to locate an observed trajectory from the array which contains most of the energy of the corresponding respiratory signal. In order to find the single observed trajectory for each target, we analyze the spectrum of each observed trajectory in the array. For a particular estimated respiration frequency, we evaluate the magnitude at this frequency along the array of spectrum and select the one with

the maximum magnitude. The corresponding *fast-time* instance of this observed trajectory can be regarded as the time-of-arrival for the related echo pulses. Based on the observation that multiple echo pulses from different targets are only partially overlapped, we can always get the single observed trajectory which contains most of the information of one target. Once we choose the observed trajectory for each target, the proposed signal processing method in Chapter 4 can be applied to each trajectory to estimate the heartbeat rate. Note that the more space that separates the single target trajectories, the less influence other targets' signals will have on the estimation, which implies that it would be beneficial to keep a certain distance for multiple targets to get sufficient difference in of times-of-arrival of multiple echo pulses.

Another important advantage of this method is that we can associate the heartbeat rate and respiration rate from the same person due to the utilization of single observed trajectory. Additionally, based on different a time-of-arrival for each trajectory, we can roughly calculate the distance between the targets which may help to precisely locate multiple targets in an emergency rescue scenario.

5.3.2 Simulation Results

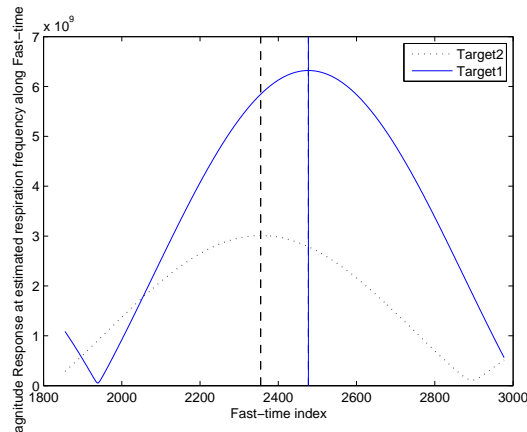
The proposed approach discussed above is verified by simulations in a two-target scenario. Based on the possible scenario setups for two-target monitoring as shown in Figure 5.1, we implement the simulations for two cases. First, we assume that the time-of-arrival of the echo pulses from two targets is close and the two pulses are highly overlapped with each other. From the Figure 5.8, we find that the two *fast-time* indexes of the single trajectories which contain the maximum energy of each target are very close which implies that both of these two single trajectory may contain a large part of the other target's signals. Figure

5.8(b) and 5.8(c) show the spectrum after applying single-target detection techniques for the picked single trajectory of each target. We find that two frequency peaks corresponding to the two targets' heartbeat rates can be detected from the frequency domain. These two heartbeat frequency peaks may become interference to each single target detection and it will be hard to associate the heartbeat rate and respiration rate from the same person. In the second simulation, we assume that there is no overlap between two echo pulses due to their relative distances to the radar system. Figures 5.9(b) and 5.9(c) show the spectrum for each single observed trajectory applied using the proposed single-target heartbeat detection method. For both spectra, a clear single frequency peak is discernible and the performance of the estimation of these two heartbeat rates is the same as for single-target heartbeat estimation.

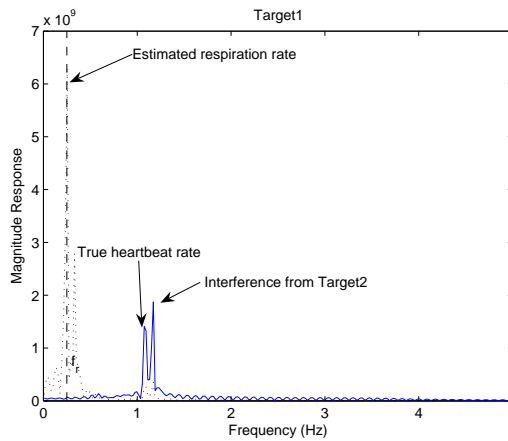
Based on the simulation results, we verified the necessity of separating multiple targets by a certain distance so that the heartbeat rate detection will not be degraded by the other targets' signal interference.

5.3.3 Limitations of the measurement setup

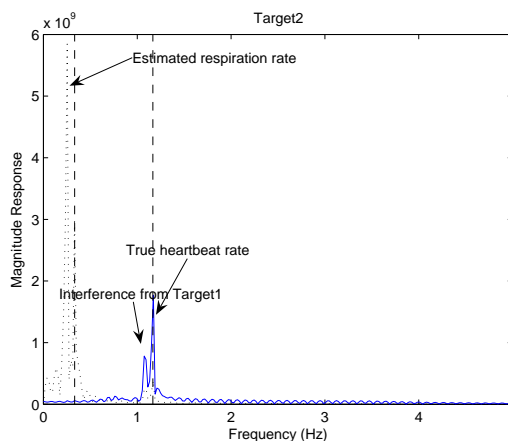
In the real experiment, especially for multi-target measurements, there is a trade-off between *fast-time* resolution and the record length of each waveform samples at each *slow-time* instance. In our current setups, at the *slow-time* sampling rate of 40Hz, the maximum record length of each received waveform is 2500 samples. With the 2 picoseconds *fast-time* resolution, the corresponding *fast-time* window of each waveform is approximately $2^{-12} \times 2500 = 5$ nanoseconds, which implies that the maximum round-trip distance between different targets from which the ideal echo pulse could be captured in the recording window, is approximately $5 \times 10^{-9} \times 3 \times 10^8 = 1.5$ meters. As mentioned in Chapter 2, the transmit pulse width is



(a) Magnitude response at the estimated respiration frequency for each trajectory in the array

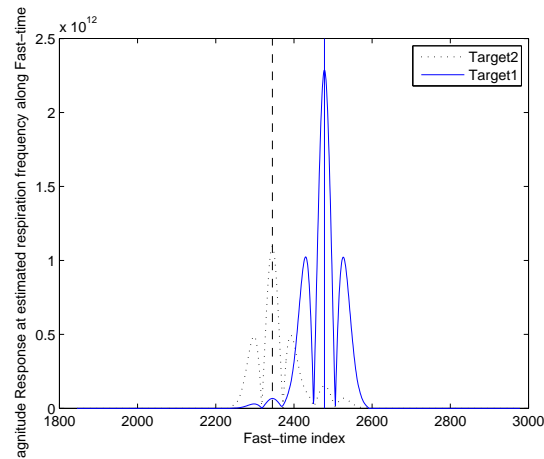


(b) Spectrum for Target1's single observed trajectory applied with proposed single target heartbeat detection method, with respiration rate 15 breath/min (0.25Hz) and heart rate 65 beats/min (1.08Hz)

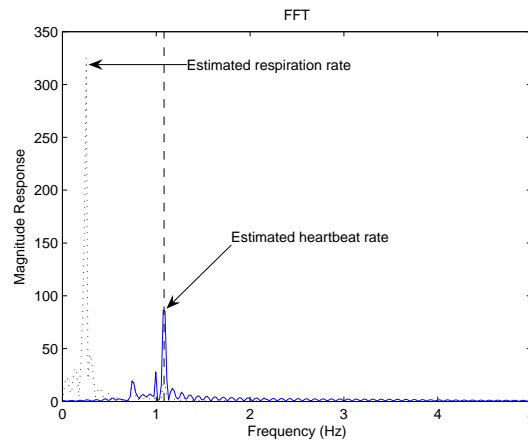


(c) Spectrum for Target2's single observed trajectory applied with proposed single target heartbeat detection method, with respiration rate 20 breath/min (0.33Hz) and heart rate 70 beats/min (1.67Hz)

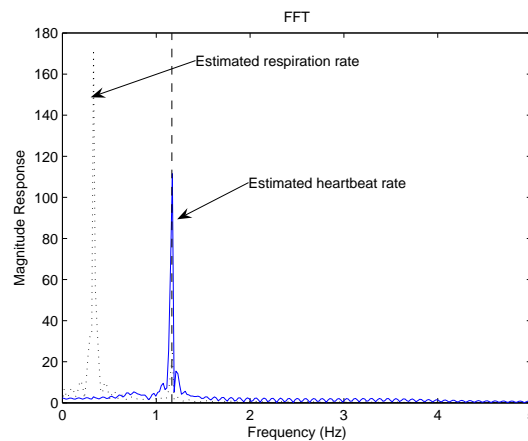
Figure 5.8: Performance of multiple targets heartbeat estimation with overlapped echo pulses



(a) Magnitude response at the estimated respiration frequency for each trajectory in the array



(b) Spectrum for Target1's single observed trajectory applied with proposed single target heartbeat detection method, with respiration rate 15 breath/min (0.25Hz) and heart rate 65 beats/min (1.08Hz)



(c) Spectrum for Target2's single observed trajectory applied with proposed single target heartbeat detection method, with respiration rate 20 breath/min (0.33Hz) and heart rate 70 beats/min (1.67Hz)

Figure 5.9: Performance of multiple targets heartbeat estimation with non-overlapped echo pulses

1nanosecond, however, due to the use of amplifier, the pulse shape is distorted like a damped sine wave which has a width much greater than 5nanoseconds at the receiver. This means that even if the targets are separated by 1.5meters, due to the increased pulse length, their echo pulses will still overlapped with each other. Based on the simulation results in the previous section, we learned that the overlapped echo pulses cause great difficulty in identifying the heartbeat rate. One way to solve this problem is to reduce the *fast-time* resolution. With a larger *fast-time* interval, the larger time window length will be gained to fit multiple non-overlapped echo pulses within the window. However, degraded *fast-time* resolution may runs the risk of failing to detect the subtle displacement of the cardiac motion. For example, if we increase the *fast-time* interval to 20picoseconds, the minimum displacement to be detected along *fast-time* axis will be $20 \times 10^{-12} * 3 \times 10^8 = 6mm$ which is larger than the average cardiac motion. This indicates that the heartbeat motions may not be able to be detected. Due to this limitation of our current measurement setup, we can not provide satisfying estimation of the heartbeat rate for multiple targets.

5.4 Conclusions

In this chapter, a signal processing technique for multiple-target estimation is investigated. We constructed an array of observed trajectories to collect the complete signals reflected from multiple targets. The MUSIC algorithm based on the covariance matrix of the signals was applied to estimate the respiration rate. Simulation and real experiment results demonstrated the capability of multiple target respiration rate detection based on our measurement setup. Further, we developed a method of combining array processing with single target detection for multiple targets heartbeat detection. We also discussed the important measurement setup parameters that will influence the performance of accurate heartbeat

estimation. The simulation and real experimental results demonstrate the feasibility of the approach.

Chapter 6

Concluding Remarks

Ultra-wideband technology has strong potential for use in the medical field, emergency rescue scenario and security. This thesis is based upon an impulse-based UWB radar monitoring system using real experiments. A FFT-based signal processing algorithm is presented to conceptually demonstrate the capability of the proposed system for non-invasive detection of respiration and heartbeat rate for a single target.

Based on the experimental and simulation results from this simple FFT-based approach, the major impediments to accurate respiration and heartbeat rate estimation are identified. For respiration rate detection, a mean position tracking algorithm is developed to avoid false detection caused by slight body motion during the experiment. The estimation of heartbeat frequency is more challenging due to the subtle cardiac displacement. A wavelet-based filter is presented which can effectively mitigate respiratory interference. Additionally, the Welch periodogram method is used for reliable spectral analysis of non-stationary bio-signals. In addition, a multi-target monitoring system based on the single target estimation techniques is proposed. The results of the various techniques described in the work demonstrate that these algorithms greatly improve the robustness and accuracy of the proposed UWB radar

system for vital-signs estimation. The work provides deep insight into signal processing techniques for vital-signs detection in a non-contact manner and gives more confidence in the real implementation of UWB biomedical devices in the future.

Bibliography

- [1] S. Venkatesh, C. R. Anderson, N. V. Rivera, and R. M. Buehrer, “Estimation of respiration rate using impulse-based UWB,” in *presented at the National Radio Science Meeting (URSI 2006)*, University of Colorado, Boulder, January 2006.
- [2] C. Torrence and G. P. Compo, “A practical guide to wavelet analysis,” *Bulletin of the American Meteorological Society*, vol. 79, pp. 61–78, January 1998.
- [3] K. M. Chenand, Y. Huang, J. Zhang, and A. Norman, “Microwave life-detection systems for searching human subjects under earthquake rubble and behind barrier,” *IEEE Trans. Biomed. Eng.*, vol. 47, pp. 105–14, January 2000.
- [4] E. F. Greneker, “Radar sensing of heartbeat and respiration at a distance with security applications,” in *SPIC-int. Soc. Opt. Eng. Proceedings of Spic - the international society for Optical Engineering*, vol. 3066, 1997, pp. 22–7.
- [5] G. Ossberger, T. Buchegger, E. Schimback, A. Stelzer, and R. Weigel, “Non-invasive respiratory movement detection and monitoring of hidden humans using ultra wideband pulse radar,” *Ultra Wideband Systems, 2004. Joint with Conference on Ultrawideband Systems and Technologies. Joint UWBST and IWUWBS. 2004 International Workshop on*, pp. 395–399, May 2004.

- [6] E. M. Staderini, “Uwb radars in medicine,” *Aerospace and Electronic Systems Magazine, IEEE*, vol. 47, pp. 13–18, January 2000.
- [7] J. C. Lin, “Non-invasive microwave measurement of respiration,” *Proceedings of the IEEE*, vol. 63, p. 1530, 1975.
- [8] J. C. Lin, E. Dave, and J. Majcherek, “A noninvasive microwave apnea detector,” *Proceedings of the San Diego Biomedical Symposium*, pp. 441–443, 1977.
- [9] J. C. Lin, J. Kiernicki, M. Kiernicki, and Wollschlaeger, “Microwave apexcardiography,” *IEEE Transaction on Microwave Theory and Techniques*, vol. 27, pp. 618–620, 1979.
- [10] K. H. Chan and J. C. Lin, “Microprocessor-based cardiopulmonary rate monitor,” *Medical and Biological Engineering and Computing*, vol. 25, pp. 41–44, 1987.
- [11] M. Nowogrodzki, D. D. Mawhinney, and H. F. Milgazo, “Non-invasive microwave instruments for the measurement of respiration and heart rates,” in *Proceedings of the IEEE 1984 National Aerospace and Electronics Conference*, vol. 2, New York, NY, USA, 1984, pp. 958–60.
- [12] J. Seals, S. R. Crowgey, and S. M. Sharpe, “Electromagnetic vital signs monitor,” Georgia Tech Research Institute Biomedical Division, Atlanta, GA, Tech. Rep. Final Report Project A-3529-060, 1986.
- [13] K. M. Chen, Y. Huang, J. Zhang, and A. Norman, “Microwave life-detection systems for searching human subjects under earthquake rubble or behind barrier,” *Biomedical Engineering, IEEE Transactions on*, vol. 47, pp. 105–114, January 2000.
- [14] E. F. Greneker, “Radar sensing of heartbeat and respiration at a distance with applications of the technology,” *Radar 97 Conference*, pp. 150–154, 1997.

- [15] M. Paksuniemi, H. Sorvoja, E. Alasaarela, and R. Myllyla, “Wireless sensor and data transmission needs and technologies for patient monitoring in the operating room and intensive care unit,” *Engineering in Medicine and Biology Society, 2005. IEEE-EMBS 2005. 27th Annual International Conference of the*, pp. 5182–5185, 2005.
- [16] S. Venkatesh, C. R. Anderson, N. V. Rivera, and R. M. Buehrer, “Implementation and analysis of respiration-rate estimation using impulse-based uwb,” in *Military Communications Conference, 2005. MILCOM 2005. IEEE*, vol. 5, October 2005, pp. 3314–3320.
- [17] K. Kang, I. Maravic, and M. Ghavami, “Ultra-wideband respiratory monitoring system,” *Ultra Wideband Systems, Technologies and Applications, 2006. The Institution of Engineering and Technology Seminar on*, pp. 191–195, April 2006.
- [18] M.-T. E. of Heart and R. R. U. U. W. Sensors, “Feasibility of dual UWB heart rate sensing and communications under fcc power restrictions,” in *Proceedings of the 14th European Signal Processing Conference (EUSIPCO 2006)*, Florence, Italy, September 2006.
- [19] S. Gezici, “Theoretical limits for estimation of periodic movements in pulse-based uwb systems,” *Selected Topics in Signal Processing, IEEE Journal of*, vol. 1, pp. 405–417, October 2007.
- [20] C. G. Bilich, “Feasibility of dual UWB heart rate sensing and communications under fcc power restrictions,” in *Proceedings UWB Radio Technology Workshop/IET 2007 Symposium on UWB*, 2007.
- [21] “Revision of part 15 of the commission’s rules regarding ultra-wideband transmission systems,” Federal Communications Commission, Washington, D.C., Tech. Rep. ET Docket 98-153, April 2002.

- [22] M. Z. Win and R. A. Scholtz, “Impulse radio: how it works,” *Communications Letters, IEEE*, vol. 2, pp. 36–8, February 1998.
- [23] R. Buehrer, W. Davis, A. Safaai-Jazi, and D. Sweeney, “Ultra-wideband propagation measurements and modeling - DARPA NETEX final report,” Virginia Tech, Tech. Rep., January 2004. [Online]. Available: http://www.mprg.org/people/buehrer/ultra/darpa_netex.shtml
- [24] C. N. Paulson, J. T. Chang, C. E. Romero, J. Watson, F. J. Pearce, and J. Levin, “Ultra-wideband radar methods and techniques of medical sensing and imaging,” *Proceedings of SPIE, Conference on Society of Photo-Optical Instrumentation Engineers*, vol. 6007, pp. 96–107, October 2005.
- [25] R. Dilsavor, W. Ailes, P. Rush, F. Ahmad, W. Keichel, G. Titi, and M. Amin, “Experiments on wideband through-the-wall imaging,” *Proceedings of the SPIE Defense and Security Symposium, Conference on Algorithm for Synthetic Aperture Radar Imagery XII, Orlando, FL*, vol. 5808, pp. 196–209, March 2005.
- [26] S. G. Azevedo and T. E. McEwan, “Micropower impulse radar,” *Science and Technology Review*, Tech. Rep. UCRL-52000-96-1/2, January 1996.
- [27] Y. Seppenwoolde, H. Shirato, K. Kitamura, S. Shimizu, and J. R. Adler, “Precise and real-time measurement of 3d tumour motion in lung due to breathing and heartbeat, measured during radiotherapy,” *International Journal of Radiation Oncol. Biol. Phys.*, vol. 53, pp. 822–34, July 2002.
- [28] D. Ruan, J. A. Fessler, and J. M. Balter, “Mean position tracking of respiratory motion,” *Medical Physics*, vol. 35, pp. 782–792, Feb. 2008.
- [29] A. W. Fitzgibbon, M. Pilu, and R. B. Fisher, “Direct least squares fitting of ellipses,”

- Pattern Recognition, 1996., Proceedings of the 13th International Conference on*, vol. 1, pp. 253–7, August 1996.
- [30] F. L. Bookstein, “Fitting conic sections to scattered data,” *Computer Graphics and Image Processing*, vol. 9, pp. 56–71, 1979.
- [31] B. Bussels, L. Goethals, M. Feron, D. Bielen, S. Dymarkowski, P. Suetens, and K. Haustermans, “Respiration-induced movement of the upper abdominal organs: a pitfall for the three-dimensional conformal radiation treatment of pancreatic cancer,” *Radiotherapy and Oncology*, vol. 68, pp. 69–74, July 2003.
- [32] B. K. Alsberg, A. M. Woodward, M. K. Winson, J. Rowland, and D. B. Kell, “Wavelet denoising of infrared spectra,” *Analyst*, vol. 122, pp. 645–652, July 1997.
- [33] S. Mallat, *Wavelet tour of signal processing*. Academic Press, 1998.
- [34] J. Lin and L. Qu, “Feature extraction based on morlet wavelet and its application for mechanical fault diagnosis,” *Journal of Sound and Vibration*, vol. 24, pp. 135–48, June 2000.
- [35] P. Welch, “The use of fast fourier transform for the estimation of power spectra: A method based on time averaging over short, modified periodograms,” *Audio and Electroacoustics, IEEE Transactions on*, vol. 68, pp. 70–73, June 1967.
- [36] M. S. Hayes, *Statistical Digital Signal Processing and Modeling*. John Wiley and Sons, 1996.
- [37] D. B. Williams and V. Madisetti, *Digital Signal Processing Handbook*. CRC Press, Inc., 1997.
- [38] H. C. So, Y. T. Chan, Q. Ma, and P. C. Ching, “Comparison of various periodograms for single tone detection and frequency estimation,” *Circuits and Systems, 1997. ISCAS*

- '97., *Proceedings of 1997 IEEE International Symposium on*, vol. 4, pp. 2529–2532, June 1997.
- [39] R. Schmidt, “Multiple emitter location and signal parameter estimation,” *Antennas and Propagation, IEEE Transactions on*, vol. 34, pp. 276–280, March 1986.
- [40] P. Stoica and T. Soderstrom, “Statistical analysis of music and subspace rotation estimates of sinusoidal frequencies,” *Signal Processing, IEEE Transactions on*, vol. 39, pp. 1836–1847, August 1991.
- [41] P. Stoica and R. L. Moses, *Introduction to Spectral Analysis*. Prentice-Hall, 1997.